

**WEARABLE TECHNOLOGIES FOR KNEE HEALTH
MONITORING USING BIOIMPEDANCE AND ACOUSTICAL
EMISSIONS**

A Thesis Presented to
The Academic Faculty

by

Sinan Hersek

In Partial Fulfillment
of the Requirements for the Degree
Doctor of Philosophy in the
School of Electrical and Computer Engineering



Georgia Institute of Technology
May 2017

COPYRIGHT © 2017 BY SINAN HERSEK

**WEARABLE TECHNOLOGIES FOR KNEE HEALTH
MONITORING USING BIOIMPEDANCE AND ACOUSTICAL
EMISSIONS**

Approved by:

Dr. Omer T. Inan, Advisor
School of Electrical and Computer
Engineering
Georgia Institute of Technology

Dr. Hua Wang
School of Electrical and Computer
Engineering
Georgia Institute of Technology

Dr. Pamela T. Bhatti
School of Electrical and Computer
Engineering
Georgia Institute of Technology

Dr. Géza F. Kogler
School of Biological Sciences
Georgia Institute of Technology

Dr. Ali F. Sarioglu
School of Electrical and Computer
Engineering
Georgia Institute of Technology

Date Approved: [January 30, 2017]

*To my parents Hüseyin and Nur Hersek, and in the memory of my grandmother Müşerref
Atasever*

ACKNOWLEDGEMENTS

It is my pleasure to thank several people who in one way or another assisted me in the completion of this work. First and foremost, I would like to express my deepest appreciation and gratitude for my advisor, Prof. Ömer Inan. This work would not have been possible without Prof. Inan's valuable guidance, supervision and support. I came across Prof. Inan's name coincidentally while searching for an advisor and after meeting him personally, decided to start working with him. Soon after this, I understood that this was one of the most correct decisions I have made in my life. His knowledge of biomedical instrumentation and physiology, his energy, and his creativeness inspired and impacted my scientific education. I am particularly thankful to him for personally teaching me important aspects of biomedical instrumentation design, designing human subject experiments, physiology and many more. He gave me the freedom of pursuing my research interests and supported and motivated me throughout my PhD. He was always accessible, approachable, friendly and thoughtful. Working with him was very rewarding and I am very grateful for his guidance.

I also would like to thank Dr. Pamela T. Bhatti, Dr. Fatih Sarıoğlu, Dr. Hua Wang and Dr. Géza F. Kogler, for taking time to serve on my dissertation committee and for their useful comments and suggestions to improve my work. They provided me with very important and fundamental insights about my research. I worked with Dr. Kogler in the design of a knee orthosis equipped with sensors. His input on how to design the orthosis was very interesting and valuable.

I was very lucky to work with smart, helpful and friendly lab-mates. I would like to thank my colleagues: Oludotun Ode, Andrew Carek, Caitlin Teague, Hazar Ashouri, Nick Bolus, Mobashir Sandhi, Nil Gurel, Hyeon Ki Jeong, Hakan Toreyin, Miheer Bavare, Ozan Bicen and Maziyar Baran Pouyan. The lab's friendly and hard-working

atmosphere motivated my work. I would like to thank Caitlin Teague, whom I worked closely with during my PhD. Her hard work and contributions to this thesis are of great value. Her friendly nature, great teamwork and technical skills made challenges in the project easier to overcome. I would like to thank Hyeon Ki Jeong and Miheer Bavare for their help in finding and collecting data from human subjects. I would like to also thank Andrew Carek for contributing to the design of the dry electrode integrated knee brace and his insights in how to package certain circuits I designed. It was also a pleasure to work with Hakan Toreyin on various aspects of the bioimpedance measurement system. I would also like to express my deepest gratitude to Hazar Ashouri. I would like to thank her for being such a great and supportive friend. Throughout my PhD I had countless great conversations with her where we exchanged ideas, and her insight was always very valuable. I thank her for being my partner in many courses we took together, for her great teamwork efforts, for her friendly nature, for always being there if I needed help whether in the lab or outside, for being my lunch and coffee buddy (I do not remember any instance where I asked Hazar if she would like to go for lunch or have coffee, and she declined), for being such a reliable person and many other things that I probably cannot fit into a few pages.

I would also like to thank my aunt Ayse Hersek, my uncle Ziya Hersek and my grandmother Suphiye Hersek. They always had faith in me and I am lucky to have such a supportive family, standing behind me. Their support during my PhD was very valuable, and I am very grateful to have them by my side.

I was very lucky to meet an extraordinary person, in the second year of my PhD. Our paths crossed coincidentally in Atlanta, and this became one of the best things that happened to me in my life. She quickly changed my life and became my family away from home. She supported me in good and bad times, motivated me to keep going and always believed in me. When I complained she listened, when I was happy because I accomplished a milestone, she made sure we celebrated each one of them. She even took

part in writing parts of this thesis and always offered help. Looking back at parts of my work, almost every part of it has something that reminds me of her because she was there for me during all of it. She stood by me against every challenge I had both in my academic and personal life. The words “thankful”, “lucky” or “grateful” do not even describe how I feel about having Norah Essali by my side, a smart, reliable, supportive and beautiful doctor.

I would like to thank my mom and dad Nur and Huseyin Hersek to whom I dedicated this thesis to. They both dedicated their life to me and they are the reason I was able to chase my dreams. I was able to get to where I am thanks to their endless support and efforts all throughout my life. They always created opportunities for me to develop myself. Every step they took in my education throughout my life had a role in bringing me to where I am right now. They made sure I went to a great school for my pre-college education, which gave me a great background in math and made me passionate about science. They made sure to enhance my creativity by introducing me to sports and music. Their wisdom and vision made me the person I am today. While I was in Atlanta pursuing my degree, their unconditional love, support and encouragement despite the long distance between us motivated me. I love them both and owe my deepest gratitude to them for their patience, sacrifice, inspiration, kindness, wisdom and for being my biggest supporters.

Finally, I also dedicate this thesis to my grandmother Muserref Atasever. I will always remember her cheerful nature, her kindness, the smile she had every time she saw me, her voice, her laugh... She touched the hearts of everyone around her and will be missed greatly. Her memory will always live with me, may she rest in peace and solace.

TABLE OF CONTENTS

ACKNOWLEDGEMENTS	iv
LIST OF TABLES	x
LIST OF FIGURES	xi
SUMMARY	xvi
CHAPTER 1: INTRODUCTION	1
1.1 Electrical Bioimpedance	2
1.2 Knee Joint Acoustical Emissions	4
1.3 Major Contributions	6
1.4 Thesis Organization	6
CHAPTER 2: DESIGN OF A ROBUST VECTOR BIOIMPEDANCE MEASUREMENT SYSTEM FOR KNEE JOINT HEALTH ASSESMENT	8
2.1 Introduction	8
2.2 System Level Design	9
2.2.1 Analog Front-End	10
2.2.2 Calibration and Current Control	13
2.2.3 Preprocessing and Feature Extraction Algorithms	16
2.3 System Verification Results and Discussion	19
2.3.1 Circuit Verification	19
2.4 Conclusion	24
CHAPTER 3: VALIDATION OF THE ELECTRICAL BIOIMPEDANCE SYSTEM IN THE CONTEXT OF KNEE JOINT HEALTH MONITORING	25
3.1 Introduction	25
3.2 Bioimpedance Measurement Setup and Electrode Placement	25
3.3 Human Subject Studies	26
3.3.1 Discriminating Healthy versus Injured Knees and Monitoring Longitudinal Injury Recovery	27
3.3.1.1 Measurement Protocol	27
3.3.1.2 Results and Discussion	27
3.3.2 Day-to-Day Variability in EBI Measurements	30
3.3.2.1 Measurement Protocol	30

3.3.2.2 Results and Discussion	30
3.3.3 Investigating Effects of Local Heating/Cooling on EBI	30
3.3.3.1 Measurement Protocol	31
3.3.3.2 Results and Discussion	31
3.3.4 Evaluating the Validity of Cardiovascular Features Computed Using the Dynamic EBI	33
3.3.4.1 Measurement Protocol	33
3.3.4.2 Results and Discussion	34
3.3.5 Demonstrating the Sensitivity of the Dynamic EBI Measures to Minute Changes in Local Blood Flow	34
3.3.5.1 Measurement Protocol	34
3.3.5.2 Results and Discussion	35
3.4 Conclusion	36
CHAPTER 4: TRANSLATION OF THE ELECTRICAL BIOIMPEDANCE MEASUREMENT SYSTEM TO WEARABLE, UNCONTROLLED SETTINGS	38
4.1 Introduction	38
4.2 Position Identification Algorithm	38
4.2.1 Human Subject Study and Measurement Protocol	41
4.2.2 Results and Discussion	42
4.3 Evaluation and Design of a Knee Wrap with Integrated Dry Electrodes	43
4.3.1 Human Subject Study and Protocol	44
4.3.2 Results and Discussion	45
4.4 Conclusion and Future Work	46
CHAPTER 5: NOVEL METHODS FOR SENSING ACOUSTICAL EMISSIONS FROM THE KNEE FOR WEARABLE JOINT HEALTH ASSESMENT	48
5.1 Introduction	48
5.2 System Design and Methods	49
5.2.1 Microphone Selection	49
5.2.2 Methods for Microphone Comparison	50
5.2.3 Interfacing Circuits	51
5.2.4 Human Subject Study and Measurement Protocol	51

5.2.5 Joint Sound Processing	53
5.3 Results and Discussion	59
5.3.1 Microphone Comparison	59
5.3.2 Joint Sound Consistency	63
5.4 Conclusion	65
CHAPTER 6: ACOUSTICAL EMISSION ANALYSIS BY UNSUPERVISED GRAPH MINING: A NOVEL BIOMARKER FOR KNEE HEALTH STATUS	66
6.1 Introduction	66
6.2 Materials and Methods	67
6.2.1 Human Subject Protocol and Subject Demographics	67
6.2.2 Signal Processing and Feature Extraction	69
6.2.3 Graph Community Factor Calculation	72
6.3 Results and Discussion	75
6.3.1 Results	75
6.3.2 Discussion	80
6.4 Conclusion and Future Work	84
CHAPTER 7: CONCLUSION AND FUTURE DIRECTIONS	86
7.1 Conclusion	86
7.2 Future Directions	87
7.3 Final Remarks	89
REFERENCES	90

LIST OF TABLES

Table 1: Comparison of the electronic and system specifications of the system proposed in this work, with numerous other electrical bioimpedance measurement systems available in literature. ^a FS = Full system, FE = Front-end only; Noise RTI in [69] was calculated for a bandwidth of 20 Hz using the noise spectral density reported. ^b Architecture sorted into four groups: (i) Computer-assisted architecture; (ii) ASIC; (iii) FPGA; (iv) Discrete design.....	23
Table 2: Demographic data for study participants (n=42 intercollegiate athletes). The lower extremity functional score (LEFS) was evaluated using the questionnaire presented in [105] on 80 point scale. *=Groups significantly different (p<0.01), std.= standard deviation.....	67
Table 3: Description of the audio features extracted from each 200 ms signal frame. For detailed information on features f_1 - f_{35} , refer to [106]. Features marked with a (*) in the “Feature Number and Name” column are time domain feature; the rest are frequency domain features. ZCR=zero-crossing rate, MFCC = Mel-Frequency Cepstrum Coefficients.....	70

LIST OF FIGURES

- Figure 1: Block diagram of the bioimpedance measurement system concept for local joint health assessment. A novel combination of both musculoskeletal and cardiovascular parameters will be obtained from the knee joint longitudinally during recovery from acute musculoskeletal injury with a wearable device based on the high performance circuit and system described here. 9
- Figure 2: Block diagram of the bioimpedance measurement system for local joint health assessment. E1-E4 represent the four electrodes on the body used for impedance measurement; $i(t)$ and $q(t)$ represent the static (slowly varying on the order of hours to days), and $\Delta i(t)$ and $\Delta q(t)$ represent the dynamic (rapidly varying on the order of milliseconds) bioimpedance components; $A(t)$ is the sensed electrical current delivery to the body being monitored in real-time to ensure safety and enable real-time calibration of the measured data on-board the microcontroller (μC). 10
- Figure 3: Physiology-driven algorithm design for extracting cardiovascular parameters automatically from the dynamic component (i.e. IPG) of the bioimpedance signals. First, the signals are pre-processed to reduce noise and detect heartbeats; then heartbeat segmentation is used to enable ensemble averaging to further improve the signal quality; finally, features of blood volume pulse and blood flow are then extracted from these ensemble averaged vector IPG traces. 17
- Figure 4: Circuit verification. (a) Photo of the printed circuit board (PCB) fabricated for the analog front-end. (b) Calibration of the resistance and reactance measurements demonstrated high linearity and consistency (points are shown for multiple measurements taken on different days). (c) Noise spectral density plots for dynamic impedance measurements (i.e. IPG). The total noise integrated from 0.8-20 Hz was found to be $18 \mu\Omega_{\text{rms}}$ for the resistive and $55 \mu\Omega_{\text{rms}}$ for the reactive dynamic components, lower than any other previously reported design in the existing literature. (d) Demonstration of improvement of calibration using the novel microcontroller-enabled automatic calibration methods described here. 20
- Figure 5: Placement of the wet gel (Ag/AgCl) electrodes for electrical bioimpedance measurements. The outer electrodes (E1 and E4) are current electrodes and the inner ones (E2 and E3), are voltage electrodes. 26
- Figure 6: Discriminating healthy versus injured knees and monitoring longitudinal injury recovery using static EBI measurements. (a) The difference in resistance versus the difference in reactance for the healthy and injured subjects. For the healthy subjects (shown in blue, N=42), the difference is that between the left and the right knee (L-R) and for the injured subjects (shown in red, N=7) it is that between the injured and the healthy knee (I-H). The error bars indicate one standard deviation. (b) The difference in resistance versus the difference in reactance for the injured subjects (N=7), when the injury is acute (within one month of the measurement take, shown in red) and during recovery (four to seven months after corrective surgery, in blue). For these subjects, the difference shown is I-H. The probability density of the healthy subjects' data (N=42, L-R

difference), estimated using 2-dimensional Gaussian kernel density estimation is also visualized in shades of orange for comparison. The error bars indicate one standard deviation..... 29

Figure 7: Mean knee resistances for seven subjects during heating (in red) and cooling (in blue) along with the standard deviations (shown in error bars). Note that each subject’s baseline knee resistance (at time=0 minutes) was subtracted from the rest of their measurements to emphasize the change in knee resistance with heating/cooling. The data points shown are at 0,5,10 and 15 minutes into heating/cooling. The skin temperatures at the patella, at these time instances during heating were: $25.7\pm 3.0^{\circ}\text{C}$, $34.7\pm 2.8^{\circ}\text{C}$, $36.1\pm 1.8^{\circ}\text{C}$ and $36.1\pm 1.4^{\circ}\text{C}$. The temperatures for cooling were: $25.6\pm 1.3^{\circ}\text{C}$, $19.5\pm 2.7^{\circ}\text{C}$, $18.3\pm 3.1^{\circ}\text{C}$ and $18.0\pm 3.3^{\circ}\text{C}$ 31

Figure 8: Human subject study results related to the dynamic EBI measures. (a) Example waveforms from the intermediate stages of the preprocessing and the feature extraction. (b) Comparison of extracted features using ECG-based vs. IPG-based ensemble averages. (c) Evaluation of the system in response to changes in physiology (vasoconstriction after 2 min. cold pressor test). 36

Figure 9: (a) Accelerometers placed on the thigh and the shank, are used to gate the EBI signals. The acceleration vector obtained from the accelerometer on the thigh is: $a_t=[a_{t,x} \ a_{t,y}]^T$. That obtained from the shank is: $a_s=[a_{s,x} \ a_{s,y}]^T$. (b) Algorithm for identifying the time intervals when the user is in the optimal position to acquire measurements (sitting, legs extended and supported). The acceptable time intervals are identified by extracting features from the dual axis accelerometer signals ($a_{t,x}(t)$, $a_{t,y}(t)$, $a_{s,x}(t)$, $a_{s,y}(t)$) and using these features to make a decision. The binary decision rule is trained once before-hand. The accepted time intervals are used to obtain the knee resistance (R_{final}) and reactance (X_{final}) using the voltage signals $i(t)$ and $q(t)$ 39

Figure 10: (a) Electrode positioning using wet Ag/AgCl electrodes as well as the positioning used for the two dual axis accelerometers. (b)The resistance ($r(t)$) signal and the x-axis shank acceleration signal ($a_{s,x}(t)$) measured from a subject during various activities. The time intervals marked in red are when the subject is in the correct position for taking measurements (sitting, legs extended and supported). The measurements taken when the subject is in the correct position are to be accepted, all other measurements (shown in blue) should be rejected. 42

Figure 11: (a) Electrode placement for the knee wrap with integrated dry copper electrodes. The electrode positions inside the wrap are indicated using green rectangles. (c) Dry, copper electrodes integrated into a knee wrap. Each electrode is made of five 4.1 cm by 3.0 cm rectangles cut out of plastic, covered with copper tape. (d) Resistance measured using dry electrodes (R_{dry}) versus that measured using wet electrodes (R_{wet}) along with the linear regression line and the 95% confidence interval for the regression shaded. (e) Reactance measured using dry electrodes (X_{dry}) versus that measured using wet electrodes (X_{wet}) along with the linear regression line and the 95% confidence interval for the regression shaded. 44

Figure 12: Block diagram of knee joint acoustic emissions sensing and interpretation for quantifying joint health during rehabilitation. 48

Figure 13: Sensor placement and measurement block diagram. (a) Eight sensors were used during human subject testing. Two IMUs were placed laterally on the thigh and shank. Piezoelectric film sensors were placed directly proximal and distal of the patella. The air microphones (MEMS and electret) were attached on the lateral and medial sides of the patella. (b) Block diagram of the data collection hardware used during human subject studies. 53

Figure 14: Significant acoustical emission identification algorithm (a) Block diagram of the whole algorithm. (b) Block diagram of the click detection portion of the algorithm. 56

Figure 15: Joint sound processing (a-c) and results (d). (a) An example 60 ms joint sound recording window showing three distinct high-amplitude, short-duration acoustical emissions. The original signal contains ambient noise, which presents as broadband signals up to 7 kHz, and interface noise, which appears as baseline movement. These components are clearly visualized in the spectrogram of the original signal. To remove the majority of the noise, the signal is band-pass filtered at 7 kHz - 16 kHz, resulting in the filtered signal $x_{Fbk}[n]$. The envelope of this signal is found, yielding $A[n]$. Using a thresholding technique based on the moving average, the significant peaks of $A[n]$ are found, roughly corresponding to the clicks of the original signal. These are later refined to match the true locations of the clicks found in the original signal (i.e., such that the locations correspond to where the clicks achieve their maximum amplitudes, positive or negative, in the original signal). (b) Final result of the click detection algorithm, which displays the identified clicks for three cycles of flexion/extension. (c) Three extension cycles with artificial offsets. These qualitatively show that the main acoustic event of each cycle occurs at similar angular locations. 58

Figure 16: Joint sounds simultaneously sensed by electret, MEMS, and piezoelectric film microphones during three repetitions of (a) flexion/extension and (b) sit-to-stand exercises. For both parts (a) and (b), the top plot displays the joint angle (θn). The middle and bottom graphs show the time and frequency domain signals from the various microphones. (The acoustic signatures of the electret and MEMS microphones exhibit similar characteristics.) 60

Figure 17: Joint sounds measured on the skin and 5 cm off the skin during flexion/extension exercises. Though the off-skin microphone captured a signal with decreased amplitude, the on- and off-skin measurements showed significant similarities in their acoustic signatures. The main acoustic event of each signal occurred at similar locations. 62

Figure 18: The final results of click location consistency for five repetitions of flexion/extension for 13 subjects on left (blue) and right (red) legs. Across subjects, the standard deviation for click location is small, supporting observations of consistent angular location cycle-to-cycle. Additionally, the mean locations of these clicks are consistent between left and right legs for most of the subjects. 63

Figure 19: An overview of the methods by which the signals acquired from the knee joint are analyzed. (a) The knee joint sound signal ($x(t)$, in blue) and the spectrogram of $x(t)$, measured from the knee of a human subject during four leg extension and flexion cycles. (b) The signal analysis workflow for knee joint sounds. The signals from the left knee of the subject are filtered and standardized (to zero mean and unity variance) and windowed (frame length of 200 ms with 50% overlap). $M=64$ features (f_1, f_2, \dots, f_M) are extracted from each of the N_{iL} frames and stored in an $N_{iL} \times M$ matrix where each row represents a frame and each column represents a feature. The aforementioned steps are repeated for the right knee and the data matrices formed using both knees are concatenated. A k-nearest neighbor graph (kNN graph) is constructed from the matrix formed using data from both knees. The graph community factor (GCF) is calculated from the kNN graph. 71

Figure 20: A representative k-nearest neighbor graph where $k=3$. The graph contains three underlying communities shown in red, blue, and black. The communities in red and blue cannot be distinctly detected using edge weights, derived from the Euclidean distance between the vertices, as the weight of the edge in green (w_{pq}) would be non-zero. Using dice similarity to calculate edge weights solves this problem, as this makes w_{pq} zero. 75

Figure 21: Visualization of the audio signal frames from nine subjects with acute unilateral knee injury (in cyan) and 33 healthy subjects (in pink), using t-Stochastic Neighbor Embedding (t-SNE). t-SNE computes a distance matrix corresponding to distances between every pair of frames. It converts this distance matrix to joint probabilities and minimizes the Kullback-Leibler divergence [117] between the joint probabilities of the 2D embedding space and the high-dimensional feature space. Note that the new calculated dimensions (e.g. t-SNE dimension 1 and t-SNE dimension 2) do not correspond to any specific acoustical features. These dimensions integrate the relations between the individual data points in the high dimensional space to represent them in a lower dimensional space. 76

Figure 22: The relationship between graph heterogeneity (quantified using the graph community factor, GCF) and acute unilateral knee injury. (a) The graph constructed using features extracted from the audio signals acquired from both knees of a healthy subject (top). The Infomap community detection algorithm discovered 16 communities (GCF=16) in the graph, all shown in distinct colors on the graph in the bottom. (b) The graph constructed using the data acquired from a subject with an acute unilateral knee injury, where 30 communities are detected. The heterogeneity of the features for the injured subject is visually and quantitatively greater than for the healthy subject. (c) The graph constructed using the data acquired from the injured subject shown in Figure 1(B), after corrective surgery, where the number of communities detected has decreased to 15, and the heterogeneity has decreased visually. (d) The GCF calculated for subjects with an acute unilateral knee injury (shown in cyan) and for healthy subjects (shown in pink). The bars represent the mean of the GCF within the population and the error bars represent one standard deviation. (*) represents a statistically significant difference ($p=0.01$), where the p-value is calculated using a paired t-test with unequal variances. (D) The GCF metric for seven subjects with unilateral knee injury before and after corrective

surgery. The black data points connected with lines represent each subject. The red data points and error bars represent the mean and one standard deviation of the GCF, for all the seven subjects, before and after surgery. 77

Figure 23: The effect of the parameter k , which is the number of neighbors each vertex is connected to in the constructed graph, on the ability of the graph community factor (GCF) metric in discriminating between subjects with an acute unilateral knee injury (in cyan) and healthy subjects (in pink). The values of k in the set $\{5,10,15,20\}$, are considered. All differences were found to be significant ($p < 0.05$) except for the case of $k = 20$, as denoted by the asterisks (*). 80

SUMMARY

Knee injuries are among the most common reasons for doctor's visits. Approximately 10 million patient visits are made each year in the United States for common knee injuries such as sprains and ligament tears [1]. The incidence rate per 1,000 persons for knee injuries is 2.29, with the most common diagnoses being strains and sprains [2].

The physical examinations of the joint during these visits are typically limited to qualitative observations based on expert examination by the clinician [3, 4]; standard examinations do not yield any quantitative feedback to the physician or patient regarding, for example, the swelling, range of motion, or structural integrity of the joint. Examination methods based on diagnostic imaging do provide quantitative metrics of joint health [5], but are less commonly used because they are expensive and time consuming. Beyond the clinic, such as in the home or with wearable technologies, there are no viable solutions available for providing in-depth, quantitative joint health assessment. Developing novel, ubiquitous technologies for joint health assessment would enable personalized, feedback-controlled therapies for patients, thus improving their quality of care, and would provide an indication of when it is safe to resume activities.

The aim of this research is to address the gap in the area of wearable knee health assessment. Towards this goal, the focus of this research was on sensing systems and signal processing techniques that can provide biomarkers for knee joint health assessment with wearable technology. Since existing sensing modalities for wearable knee health assessment do not provide clinically-relevant metrics, two novel modalities of wearable physiological measurements were acquired from the knee in this work: (1) electrical bioimpedance and (2) acoustical emission signals. This dissertation describes the technologies for measuring, processing, and interpreting these signals.

CHAPTER 1: INTRODUCTION

The knee is one of the most complex joints in the body [6] and is thereby subject to extreme stress due to the multidirectional forces exerted on the joint during motion [6, 7]; additionally, its intricate structural arrangement, reliance on soft tissue networks for structural stability, and large loading requirements leave the joint particularly susceptible to injury [8-10]. As a result, the knee represents not only one of the most frequently injured body parts but also accounts for many severe injuries in terms of time of restricted and/or total loss of participation among athletes [11-13], military personnel [14], and other populations engaged in high performance activities [15]. Moreover, knee injuries are not exclusive to active populations; sedentary populations may be at higher risk for such injuries due to poor cardiovascular health, atrophied surrounding muscles which fail to properly stabilize the joint, and lack of training and warm-up [7, 15]. This frequency across populations combined with the extensive treatment requirements—often entailing surgery and/or substantial rehabilitation [8]—result in approximately 10.4 million patient visits annually in the United States [16]. To this extent, these injuries are considerable in their effect on not only the health care system but also on patients' daily lives given the knee's significance in performing ambulatory motions and other everyday activities [9].

The physical examinations of the joint during these visits are typically limited to qualitative observations based on expert examination by the clinician [3, 4]; standard examinations do not yield any quantitative feedback to the physician or patient regarding, for example, the swelling, range of motion, or structural integrity of the joint. Examination methods based on diagnostic imaging do provide quantitative metrics of joint health [5], but are less commonly used because they are expensive and time consuming. Beyond the clinic, such as in the home or with wearable technologies, there are no viable solutions available for providing in-depth, quantitative joint health

assessment. Developing novel, ubiquitous technologies for joint health assessment would enable personalized, feedback-controlled therapies for patients, thus improving their quality of care, and would provide an indication of when it is safe to resume normal activity.

To facilitate monitoring of patients during daily activities, researchers have explored the use of wearable devices to unobtrusively acquire health information [17]. With regard to musculoskeletal and biomechanical-related disorders and injuries, these systems may provide a new way to collect objective and quantitative data. For example, A. Rampp *et al.* assessed gait impairment parameters in elderly populations using data from inertial sensors worn on shoes, thus providing a successful wearable alternative to clinic-based diagnostics (e.g., specialist observation, camera-based laboratories, sensor-embedded walkways, etc.) [18]. L. Atallah *et al.* also investigated gait, leveraging changes in gait patterns in post-operative, knee-replacement patients to evaluate recovery progress by utilizing an ear-worn sensor [19]. L. Toffola *et al.* developed a wearable sleeve to record robust knee joint kinematics and subject compliance during long-term, at-home activities and therapies [20]. While these approaches provided some indication that wearable technologies may have merit in assessing rehabilitation progress, the techniques lacked specific, in-depth information regarding the health of the joints.

In this work, the use of two novel modalities of physiological signals for knee health monitoring is explored in the context of wearable measurements: electrical bioimpedance (EBI) and acoustical emissions. Towards this goal, sensing systems and signal processing techniques that can provide biomarkers for knee joint health assessment are developed and discussed.

1.1 Electrical Bioimpedance

One technology that has been investigated for local joint health assessment recently is EBI. For EBI measurements, a small electrical current is injected into a volume of tissue

– such as the volume of tissue encapsulating a knee joint – and the resultant voltage drop across the tissue is measured [21-23]; the ratio of this voltage to the injected current yields the electrical impedance of this tissue, and can change based on the structural composition of the medium (e.g. increased edema decreases the tissue impedance since fluid is less resistive than muscle, fat, or bone).

EBI has been demonstrated in previous studies as a possible means of evaluating knee osteoarthritis [24], edema (swelling) related to lower limb muscle injuries [25, 26], and edema for total knee arthroplasty surgery and rehabilitation [27]. EBI has also been used in cardiovascular physiology research as a means of quantifying blood flow and volume, such as for estimating cardiac output or the local blood flow rate to (or blood volume pulse at) a limb [21, 28, 29].

While EBI measurements for structural assessment typically examine the *static* (varying over the course of hours to days) component of tissue impedance, measurements for cardiovascular assessment examine the *dynamic* (varying over the course of milliseconds) components. The dynamic EBI has a bandwidth of approximately 0.8-20 Hz [30]. This signal originates from the pulsatile impedance changes of tissue, due to the blood volume pulse (and blood flow) associated with each cardiac cycle [31]. Additionally, while static EBI measurements involve magnitudes of changes on the order of Ohms to tens of Ohms, dynamic cardiovascular measures from limbs can be as small as tens of milli-Ohms [32]. Accordingly, the performance of the analog front-end circuitry for EBI measurements becomes significantly more challenging when targeting both static and dynamic measurements.

Nevertheless, many researchers have made significant advances over the past several years in EBI circuit and system design, including improving the current source for high frequency implementation [33], increasing the output impedance and accuracy of CMOS current drivers for EBI [34], developing error correction algorithms [35], and investigating solutions for textile electrode interfaces [36]. In the literature, such

measurements of dynamic changes in electrical bioimpedance are referred to as impedance plethysmography (IPG) [21, 37].

In addition to quantifying edema with static EBI, quantifying the local blood flow patterns following a joint injury with IPG could provide significant insight into joint rehabilitation progress. An increase in local blood flow may follow an injury to the joint, associated with inflammation and scar tissue formation, while decrease in local blood flow may be indicative of improving status [38]. Such changes in blood flow patterns are believed to precede changes in structure (edema) or range of motion, and can potentially provide very early indicators for changing joint health status. Beyond local blood flow, IPG measurements can also provide a window to evaluating the overall cardiovascular physiology and autonomic nervous system (ANS) balance through heart rate variability (HRV) [39, 40], thus providing an index of a person's sympathetic arousal which has been shown to increase in response to pain [41]. However, no existing bioimpedance technologies, in the commercial or research domains, are capable of providing both the required resolution to capture edema measures and blood flow through the knee joint, and operate on sufficiently low power consumption such that several hours of use on a small battery is feasible.

1.2 Knee Joint Acoustical Emissions

Acoustics can provide an unobtrusive method—and thus a possible wearable platform—for capturing information regarding underlying physical structures and alignments, articulating surfaces, and soft tissue characteristics. Friction between the structures and articulating components of the knee joint gives rise to various kinds of vibrations [42]. These vibrations (i.e., acoustical energy) travel to the skin surface where they encounter a large impedance mismatch between the fluid-filled tissue and air. Because of this, most of the acoustical energy manifests itself as vibrations signals on the skin with the majority of the energy reflected back into the tissue [43]. However, there is a small amount of

energy that propagates to the air, resulting in audible joint sounds. While some very early work in this area studied airborne signals using “air” microphones, the majority of research has largely utilized vibration sensors as “contact” microphones (e.g., accelerometers, piezoelectric devices, stethoscopes) to measure joint sound vibrations [44].

Researchers have concentrated on the efficacy of joint acoustical emissions, sometimes referred to as vibroarthrographic signals (VAG), as clinically-relevant biomarkers for joint health, and notably, the majority of the research has worked towards developing diagnostic techniques to differentiate “healthy” vs “unhealthy” knee joints, primarily as it concerns cartilage-based conditions such as osteoarthritis and chondromalacia. For example, R. Mollan *et al.* measured acoustical emissions from the knee using a condenser microphone and captured low frequency signals (<100 Hz) [43] while L. Shark *et al.* used wide-band piezoelectric sensors to record emissions in the ultrasonic band (>20 kHz) [43, 45]. They observed differences between healthy knees and those afflicted with osteoarthritis and found that osteoarthritic knees produce more frequent, higher peak, and longer duration acoustical emissions compared to healthy knees [45]. J. Lee *et al.* also evaluated osteoarthritic subjects using an accelerometer and successfully classified three different conditions of the patellofemoral joint [46]. To achieve such outcomes, significant work has been devoted to developing various signal processing techniques for conditioning and classifying such signals. Algorithms have leveraged linear prediction [47] and autoregressive modelling [46], statistical parameter investigation [48], Fourier [49] and time-frequency [50] analysis, wavelet decomposition [51, 52], and neural networks and other classifier methods such as dynamic weighted classifier fusion [48, 52].

The ultimate goal is to enable around-the-clock monitoring of joint acoustics during normal activities of daily living, and prescribed rehabilitation activities that elicit specific signatures indicative of improving or worsening joint health. The previous work

in the area of knee joint acoustical emissions mostly focuses on diagnostics in controlled settings, rather than longitudinal monitoring with wearable technology.

1.3 Major Contributions

The major contributions of this work to the scientific community can be summarized as follows:

- 1) Demonstrated, for the first time, wearable systems for measuring high quality knee acoustical emissions and swelling (using electrical bioimpedance) data.
- 2) Improved the robustness of these measurements in unsupervised settings (e.g., the home) using multi-modal sensing and sensor fusion algorithms.
- 3) Discovered physiological biomarkers of knee health that can be derived from these wearable measurements to discriminate healthy from injured knees and track rehabilitation progress.

1.4 Thesis Organization

This work is organized as follows: In Chapter 2, the design of an analog front-end targeted for wearable knee joint health monitoring is presented. A real-time calibration algorithm is also designed, allowing EBI measurements robust to environmental changes to be acquired. Pre-processing and feature extraction algorithms are presented to acquire the knee resistance and reactance from the static EBI signals, which are related to musculoskeletal health. Algorithms are presented to acquire cardiovascular features such as heart rate, local blood volume and blood flow rate from the dynamic EBI signals. The resolution and power consumption of the designed hardware is presented and, the ability of the designed real-time calibration algorithm in providing robustness to changes in environmental temperature is demonstrated.

In Chapter 3, a comprehensive validation of the EBI measurement system is made in the context of knee joint health monitoring. A human subject study that demonstrates

the ability of static EBI measurements in identifying knee injury is presented. Furthermore, the ability of static EBI measurements in monitoring knee injury recovery is demonstrated on human subjects with acute, unilateral knee injuries. A study of the inter-day variability of static EBI measurements is presented. Furthermore, the ability of the designed EBI measurement system in detecting small changes in local interstitial fluid volume and limb blood flow are demonstrated.

Chapter 4 focuses on the translation of the EBI measurement system described, into uncontrolled wearable settings. Towards this goal, a position identification algorithm is presented and validated (using human subject experiments) that allows EBI measurements to be taken while the knee assumes a certain consistent posture and while motion artifacts are not present. Furthermore, a knee brace with dry electrodes integrated, capable of acquiring EBI measurements with comparable reliability to wet, gel electrodes, is presented.

In Chapter 5, the measurement of knee joint acoustical emissions is described. The ability of various types of microphones in acquiring these acoustical emissions is contrasted. Furthermore, it is demonstrated that the characteristic acoustical emissions from the knee joint are short duration, high energy and broad band signatures. It is demonstrated that these signatures occur in consistent knee joint angles during unloaded leg flexion and extension.

Chapter 6 introduces a novel algorithm that utilizes unsupervised graph mining techniques, to calculate a biomarker relating to knee joint health, using acoustical emissions. It is shown that the biomarker devised can distinguish between subjects with healthy knees and subjects with acute, unilateral knee injury, and it is presented that the biomarker demonstrates improvement in knee joint health during injury recovery. Finally, concluding remarks and future research pathways are discussed in Chapter 7.

CHAPTER 2: DESIGN OF A ROBUST VECTOR BIOIMPEDANCE MEASUREMENT SYSTEM FOR KNEE JOINT HEALTH ASSESSMENT

2.1 Introduction

In this section, methods for addressing the technological gap in the area of wearable EBI measurement systems for local joint physiology assessment are presented. Specifically, a system-level biomedical proof-of-concept that measures bioimpedance signals and then extracts both musculoskeletal (tissue resistance and reactance), and cardiovascular (heart rate, local blood volume, and flow rate) parameters is reported (Figure 1). These physiological parameters can then be used to quantify both edema and blood flow during post-injury recovery. The work presented advances the state-of-the-art for EBI measurement systems by: (1) incorporating a custom bioimpedance measurement analog front-end for both tissue impedance (static) and local hemodynamics (dynamic) with the highest resolution given the power consumption and size, compared to similar systems, (2) employing a novel self-calibration procedure to minimize drift and inaccuracy due to environmental factors such as temperature, and (3) creating customized physiology-driven algorithms for IPG-based heartbeat detection to alleviate the need for a reference biosignal recording (e.g., an electrocardiogram, ECG) for extracting hemodynamic parameters from the knee.

In the remainder of this chapter, the design details of the system are presented, followed by the details of the bench test verification and concluding remarks. The work presented in this chapter and the following one were published in [53].

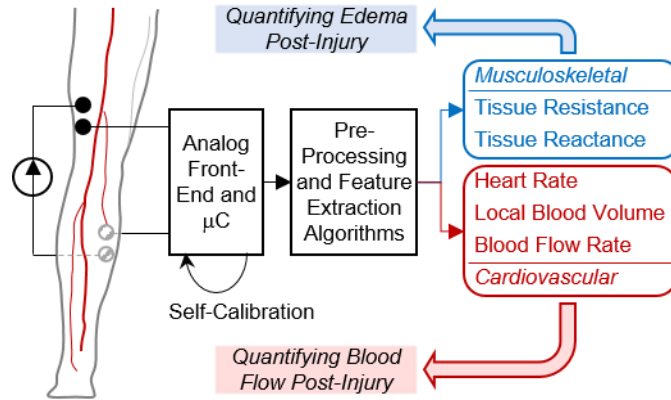


Figure 1: Block diagram of the bioimpedance measurement system concept for local joint health assessment. A novel combination of both musculoskeletal and cardiovascular parameters will be obtained from the knee joint longitudinally during recovery from acute musculoskeletal injury with a wearable device based on the high performance circuit and system described here.

2.2 System Level Design

The aims of quantifying edema and blood-flow in the post-injury period necessitate a small form factor system obtaining accurate EBI measurements from the body in an energy-efficient manner. Towards reaching that goal, a digitally-assisted analog approach was followed: designing a system benefiting from the advantages of both analog (i.e., low power) and digital (i.e., programmability) domains. The system uses this approach to perform (1) EBI measurements, (2) calibration, and (3) preprocessing and feature extraction. The first function, namely performing the EBI measurements from the body, is achieved by a custom, analog front-end designed with discrete components. A low-power TI MSP430 series microcontroller (Texas Instruments, Inc., Dallas, TX) is used with a micro secure digital (SD) card as a data logger to enable processing of the signals later on a computer. The microcontroller is also used to implement the second function of the system, namely performing calibration, which aims to reduce the measurement error due to environmental changes (e.g., temperature). The last function, namely feature extraction, is performed using MATLAB software (MathWorks, Natick, MA) to extract

physiologically-relevant information from the calibrated data stored on a microSD. Below, the system-blocks implementing the aforementioned three functions are detailed.

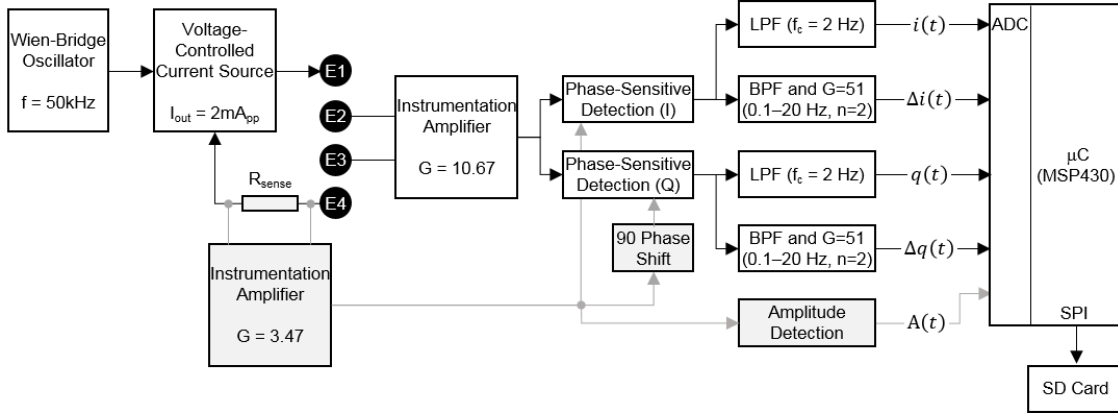


Figure 2: Block diagram of the bioimpedance measurement system for local joint health assessment. E1-E4 represent the four electrodes on the body used for impedance measurement; $i(t)$ and $q(t)$ represent the static (slowly varying on the order of hours to days), and $\Delta i(t)$ and $\Delta q(t)$ represent the dynamic (rapidly varying on the order of milliseconds) bioimpedance components; $A(t)$ is the sensed electrical current delivery to the body being monitored in real-time to ensure safety and enable real-time calibration of the measured data on-board the microcontroller (μC).

2.2.1 Analog Front-End

Consisting of resistive body fluids (e.g., blood, intra-cellular fluid) and capacitive cell-walls, the EBI of a local joint body region can be modeled, to the first order, as a single RC network. It should be noted that the RC network has a static component related to the total fluid-volume and a dynamic component related to the time-dependent fluid-volume changes (e.g., blood flow periodic with the heart beat). An analog front-end was designed, to perform a single-frequency bioimpedance analysis to extract both static and dynamic components of the RC network (block diagram of front-end shown in Figure 2).

The circuit excites the body with a sine wave current at $f_o=50$ kHz, a frequency that enables current to flow through both extracellular and intracellular fluid paths and therefore is widely used in single-frequency bioimpedance analysis systems [54]. The design incorporates a diode-stabilized Wien-Bridge oscillator generating an 800 mV_{pp} sinusoidal signal at 50 kHz. The voltage output of the oscillator is converted to current by

a high output-impedance, high-bandwidth, voltage-controlled current source (VCCS). There are four on-board series RC loads for real-time calibration measurements. The VCCS current is delivered through either one of these loads or the tissue impedance (Z_{body}) through the use of an 8:1 multiplexer. The three multiplexer select bits are controlled by the MSP430 to select which load to deliver the current through. The VCCS current also passes through a resistive load, $R_{sense}=100\ \Omega$, in series to the selected load. Ag/AgCl wet gel electrodes are used to inject current to the tissue because of their lower skin-electrode interface impedance compared to dry electrodes.

Sweat, skin humidity and hair cause the skin-electrode interface impedance to vary [55, 56]. To cancel out these variations, a four-electrode configuration formed by two current injection and two voltage measurement electrodes was employed. Four digital potentiometers (one 10 k Ω and three 1k Ω in parallel for coarse and fine tuning, respectively) are used to digitally control the injection current amplitude (I_{pp}). The resistances of the potentiometers are controlled via five signals, through the MSP430. Voltage measurements across the on-board loads or Z_{body} and R_{sense} are made by means of two separate instrumentation amplifier (IA) stages, IA_{sense} and IA_{body} . The load which IA_{body} measures across (the on-board loads or Z_{body}) is chosen using two microcontroller-controlled 2:1 multiplexers. The signal at the output of IA_{body} , namely $v_{body}(t)$ is used to extract voltage measurements corresponding to both resistive and reactive components of Z_{body} through phase-sensitive detection circuitry. A differential high-pass filter (HPF) with a cut off frequency of 7.2 kHz reduces any electromyogram (EMG) bleed-through from the surrounding muscles. To reduce phase errors in demodulation, the same differential HPF is used for IA_{sense} as well. The signal at the output of the IA_{sense} , namely $v_{sense}(t)$, is used for (1) generating the clocks that drive the phase-sensitive detection circuitry using comparators and (2) monitoring the magnitude of the current delivered to the body, namely I_{pp} , through an envelope detector

formed by a diode and RC network, the output of which is the current monitoring signal $A(t)$ in Figure 2. The clocks for the in-phase and quadrature-phase sensitive detection are generated using comparators from the $v_{sense}(t)$ and a 90° phase shifted version of the $v_{sense}(t)$ obtained using an all-pass-filter, respectively. Both clocks are used to alternate analog switches between $v_{body}(t)$ and $-v_{body}(t)$.

The signal from each phase-sensitive detector is filtered to give the final output signals. For the very slowly-varying static in-phase and quadrature signals, namely $i(t)$ and $q(t)$, the outputs of phase-sensitive detectors are each filtered with a second order Sallen-Key low-pass filter (LPF) having a cutoff frequency of $f_{-3dB}=2$ Hz as seen in Figure 2. To extract the small-magnitude and more rapidly-varying dynamic in-phase and quadrature signals, namely $\Delta i(t)$ and $\Delta q(t)$, the signals from the phase sensitive detector are filtered by band-pass filters (BPF) with bandwidths of 0.1 Hz-20 Hz and gains of 51 V/V (Figure 2). The signals $A(t), i(t), q(t), \Delta i(t)$ and $\Delta q(t)$ are sampled and logged on a microSD card at a rate of 2 kHz, which is well above their Nyquist frequency.

It should be noted that, the sinusoidal voltage signal from the oscillator is amplified through the VCCS and the IA_{body} stages, which set the mid-band gain, namely A_{MB} . When determining A_{MB} , both noise and dynamic range considerations have been taken into account. For improved noise performance, A_{MB} needs to be sufficiently high. On the other hand, to obtain a large dynamic range that satisfies the linear operation of the circuit, A_{MB} cannot be arbitrarily large. For a typical knee impedance value of $R_{body}=80 \Omega$, high signal-to-noise ratio (SNR) signals can be obtained by setting $I_{pp}\approx 2$ mA, which is well below the safety threshold [57]. The multiplexer on and off leakage currents which are less than 10 nA have negligible effects given that the injection current amplitude is on the order of milli-Amps. However, it should be noted that Z_{body} will vary among different subjects. Therefore, the VCCS is designed as a digitally controlled variable-gain stage that can be tuned to ensure linear operation while not compromising

the noise performance. For instance, to obtain high SNR signals from small impedance loads, I_{pp} can be increased. On the other hand, for measurements from larger impedance loads, to keep the circuit in the linear region, I_{pp} can be reduced. The maximum and minimum possible values of I_{pp} are 4 mA_{pp} and 0.2 mA_{pp}, respectively. The gain of the IA_{body} , namely $A_{IA,body}$, is determined based on the dynamic range constraints. Setting $A_{IA,body}=10.67$ V/V, a dynamic range of $\sim 300 \Omega$, which exceeds the typical maximum bioimpedance values from the knee, is achieved. The gain of IA_{sense} , is set to $A_{IA,sense}=3.47$ V/V, which is sufficiently high for generating clocks at the comparator outputs.

The measurements from the analog front-end are converted to resistance and reactance values by following an automatic calibration procedure. During a measurement period, to compensate for the effects of environmental changes on the measurements, calibration is automatically repeated. Below, the calibration procedure is detailed.

2.2.2 Calibration and Current Control

As with any bioimpedance measurement system, a calibration procedure is necessary to map the static and dynamic voltage signals – namely $i(t), q(t), \Delta i(t), \Delta q(t)$ – into static and dynamic impedance signals; namely static resistance $r(t)$, static reactance $x(t)$, dynamic resistance $\Delta r(t)$ and dynamic reactance $\Delta x(t)$. In an ideal synchronous demodulation scheme, $i(t)$ and $q(t)$ would be proportional to $r(t)$ and $x(t)$ respectively, where the impedance being measured is $r(t) + jx(t)$. Therefore, ideally a one-time calibration of the circuitry would be sufficient to map the measured signals to impedance values. However, changes in environmental parameters (e.g., temperature, humidity), and circuit non-idealities, adversely affect the measurement consistency along the course of a measurement. To correct measurement errors caused by changes in the excitation current,

I_{pp} , and therefore increase the robustness of the system, the impedance measurements can be scaled by a correction factor (amplitude correction):

$$c_f = \frac{2 \times 10^{-3}}{I_{pp}} \quad (1)$$

where I_{pp} is monitored by $A(t)$. Furthermore, temperature variations also create phase delays at the clocks of the phase-sensitive detection circuitry switches, which affect both the magnitude and phase of an impedance measurement. The multiplexer R_{ON} resistances can also potentially cause measurement error by offsetting the measured impedances; accordingly, we have selected a multiplexer with close matching of on resistances between channels, and rely on the four-wire measurement approach to cancel the overall effect of R_{ON} . To further rule out those errors, calibration can be performed in an intermittent manner (real-time calibration) by a low-power TI MSP430 series microcontroller.

As an effort to reduce the calculation burden that real-time calibration could potentially place on the microcontroller, a computationally-efficient two-step calibration procedure is followed: (1) phase correction and (2) ordinary least squares linear regression.

The first calibration step is correcting the phase error. The non-ideal switching time, namely $t_{sw} > 0$, of the demodulator switches in phase-sensitive detection circuitry results in rotation of the measurement vector $[i(t) \ q(t)]^T$ by ϕ radians anti-clockwise, where $\phi = 2\pi t_{sw} f_0$. Therefore the phase error is corrected by rotating the vector by ϕ radians clockwise to obtain the corrected measurement vector:

$$\begin{bmatrix} \tilde{i}(t) \\ \tilde{q}(t) \end{bmatrix} = \begin{bmatrix} \cos\phi & \sin\phi \\ -\sin\phi & \cos\phi \end{bmatrix} \begin{bmatrix} i(t) \\ q(t) \end{bmatrix} \quad (2)$$

where $\tilde{i}(t)$ and $\tilde{q}(t)$ are proportional to $r(t)$ and $x(t)$, respectively.

The second step aims to map the corrected measurement vector to the impedance vector:

$$\begin{bmatrix} r(t) \\ x(t) \end{bmatrix} = \begin{bmatrix} m_R \\ m_X \end{bmatrix} \begin{bmatrix} \cos\phi & \sin\phi \\ -\sin\phi & \cos\phi \end{bmatrix} \begin{bmatrix} i(t) \\ q(t) \end{bmatrix} + \begin{bmatrix} c_R \\ c_X \end{bmatrix} \quad (3)$$

where m_R and c_R are the coefficients of linear regression between $\tilde{i}(t)$ and $r(t)$.

Similarly m_X and c_X are regression coefficients for the quadrature channel.

Finding the calibration coefficients in (3) – namely m_R, c_R, m_X, c_X , and ϕ – requires a series of static in-phase and quadrature measurements on test loads of known values. Four series RC test loads, which span the impedance dynamic range, with impedances $R_1 = 23.8 \Omega, C_1 = 47 \text{ nF}; R_2 = 98.2 \Omega; R_3 = 56.4 \Omega, C_3 = 94 \text{ nF}; R_4 = 75.4 \Omega, C_4 = 68 \text{ nF}$ are selected. The loads are connected to the analog front-end successively by means of a multiplexer controlled by the microcontroller. The phase correction step is performed by calculating $\phi = \arctan q_2/i_2$ using measurements from the purely resistive R_2 . Then, linear regression is performed using the measurements from all four test loads to calculate the remaining calibration coefficients. The offset vector $[c_R \ c_X]^T$ compensates for the offset introduced to the impedance measurements by the multiplexer R_{ON} resistances. The same coefficients are used to perform the mapping for the dynamic measurements:

$$\begin{bmatrix} \Delta r(t) \\ \Delta x(t) \end{bmatrix} = \frac{1}{G} \begin{bmatrix} m_R \\ m_X \end{bmatrix} \begin{bmatrix} \cos\phi & \sin\phi \\ -\sin\phi & \cos\phi \end{bmatrix} \begin{bmatrix} \Delta i(t) \\ \Delta q(t) \end{bmatrix} \quad (4)$$

where the factor $1/G$ is introduced to divide out the dynamic channel output gain. The offset vector $[c_R \ c_X]^T$ in (3) is filtered out by the dynamic channel output stages.

To rule out current drifts and increase consistency and accuracy furthermore, a current control algorithm is implemented in an intermittent manner before every real-time calibration cycle. The multiplexers are switched to measure the on-board resistive load (R_2). As $\alpha = i_2^2 + q_2^2$ is proportional to $I_{pp}R_2$, it can be used to monitor the current amplitude I_{pp} . Therefore, to reset I_{pp} to 2 mA_{pp} , first the digital potentiometers are set to the highest resistances resulting in minimum current amplitude. The resistance of the 10 k Ω potentiometer and the 1 k Ω potentiometers are adjusted respectively (coarse tuning and fine tuning) while α is monitored using i_2 and q_2 read from the ADCs. The tuning

ends when α is within some pre-determined range such that $1.9 \text{ mA}_{pp} < I_{pp} < 2.1 \text{ mA}_{pp}$. After this procedure, real-time calibration is performed with the newly set current.

The mapped signals obtained after calibration are then used to extract musculoskeletal and cardiovascular features from the knee joints, which is explained in the next sub-section.

2.2.3 Preprocessing and Feature Extraction Algorithms

The preprocessing and feature extraction is separately done for static and dynamic signals. The musculoskeletal features of tissue resistance and reactance are extracted from the static signals and the cardiovascular features of heart rate, local pulsatile blood volume and flow rate are extracted from the dynamic signals.

The preprocessing of the static signals $i[n]$ and $q[n]$ involves conversion to impedance signals $r[n]$ and $x[n]$ using (3). Then, the static signals and the current monitoring signal $A[n]$ are averaged in a 60 second window, to get r_{avg} , x_{avg} , and A_{avg} , respectively. The final joint resistance and reactance measurements of $R_{measured}$ and $X_{measured}$ are obtained by performing the amplitude correction explained in the calibration section on r_{avg} and x_{avg} using A_{avg} .

The signal processing performed on the dynamic signals involves calibration/filtering and ensemble averaging as shown in Figure 3. The dynamic signals, $\Delta i[n]$ and $\Delta q[n]$, are first converted to impedance signals via calibration using (4). The dynamic impedance signals are then amplitude corrected using A_{avg} which is followed by band-pass filtering by an FIR (finite impulse response) filter with bandwidth 0.4 Hz to 20 Hz to obtain $\widehat{\Delta r}[n]$ and $\widehat{\Delta x}[n]$. The filtering step reduces the respiratory artifacts which lie within a frequency range of 0.04-2 Hz [30]. Motion artifacts in EBI measurements consist of frequency components ranging from 0.1-10 Hz [58], which is in-band with the EBI signals of interest; accordingly, these artifacts are difficult to

remove and can compromise measurement integrity. This step completes the calibration/filtering of the impedance signals before they are ensemble averaged.

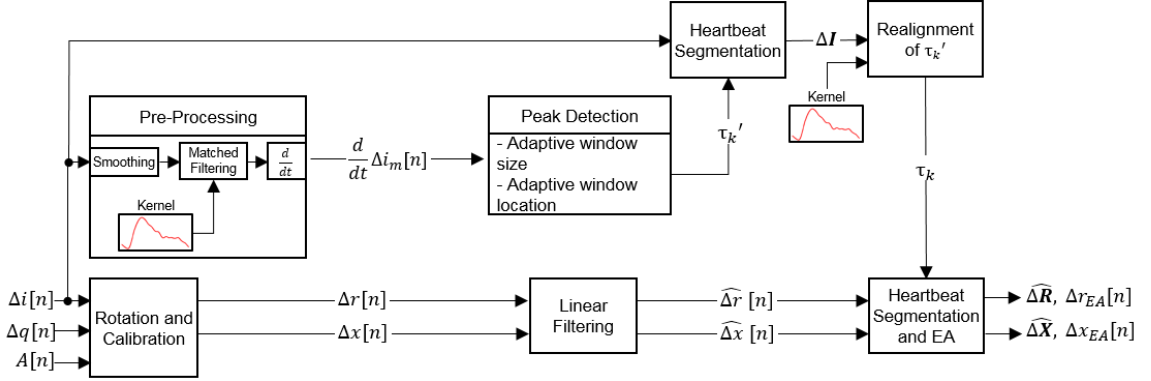


Figure 3: Physiology-driven algorithm design for extracting cardiovascular parameters automatically from the dynamic component (i.e. IPG) of the bioimpedance signals. First, the signals are pre-processed to reduce noise and detect heartbeats; then heartbeat segmentation is used to enable ensemble averaging to further improve the signal quality; finally, features of blood volume pulse and blood flow are then extracted from these ensemble averaged vector IPG traces.

Heartbeats from the knee are detected using $\Delta i[n]$. This signal is first smoothed using a Savitzky-Golay filter of 4th order and 21 taps, then filtered using a matched filtering approach [59, 60]. Savitzky-Golay filtering was used as it is more successful than standard averaging FIR filters in keeping the pertinent high frequency components of the signal. The order of the filter and the number of taps was chosen heuristically. The matched filter impulse response (kernel) is a clean, smoothed dynamic in-phase bioimpedance signal, also acquired from the knee previously. This kernel is stored for use and is not adaptive. The matched filtered signal is then differentiated using a Savitzky-Golay Filter of the same kind as used for the smoothing, to form the signal $\frac{d}{dt} i_m[n]$.

The signal $\frac{d}{dt} i_m[n]$ is fed to a peak detection algorithm to detect heart beats. Peaks in the waveform are searched window-by-window. When a peak is found within the given window, the window size is updated using previous heartbeat intervals. The window is then moved to its next location. To make sure the heartbeats are detected precisely, the window is re-located such that the peak is around the mid-point of the

given window. The peak times found are stored in a vector τ'_k . The number of peaks detected per minute gives the heart rate (HR) in bpm.

The signal $\Delta i[n]$ is segmented using the peak times τ'_k . The segments of $\Delta i[n]$ ($\Delta i_k[n]$) are stored in each row of the matrix $\Delta \mathbf{I}$. The cross correlation of each segment $\Delta i_k[n]$, with the kernel is calculated. The maximum of this cross correlation is used to correct the peak times τ'_k such that each $\Delta i_k[n]$ is aligned with the kernel. The corrected peak times are stored in the vector τ_k .

The peak times τ_k are used to segment $\widehat{\Delta r}[n]$ and $\widehat{\Delta x}[n]$. The segments $\widehat{\Delta r}_k[n]$ and $\widehat{\Delta x}_k[n]$ are stored in rows of the matrices $\widehat{\Delta \mathbf{R}}$ and $\widehat{\Delta \mathbf{X}}$ respectively. The ensemble average of $\widehat{\Delta r}[n]$ is calculated by averaging the segments $\widehat{\Delta r}_k[n]$ on a sample by sample basis equation:

$$\Delta r_{EA}[n] = \sum_{k=1}^N \widehat{\Delta r}_k[n] \quad (5)$$

The ensemble average of $\widehat{\Delta x}[n]$ ($\Delta x_{EA}[n]$) is then calculated in an analogous manner. The ensemble averaged signals $\Delta r_{EA}[n]$ and $\Delta x_{EA}[n]$ are used for feature extraction. The peak-to-peak amplitudes of these waveforms, Δr_{pp} and Δx_{pp} , are extracted as they might show differences in injured and healthy knees.

The signal $\Delta r_{EA}[n]$ is differentiated using the same Savitzky-Golay filter mentioned before, to obtain $\frac{d}{dt} \Delta r_{EA}[n]$. On the waveforms, the B, C and X points defined in [22] are identified. The amplitude difference between the points B and C ($\frac{d}{dt} \Delta r_{MAX}$ in Ω/s) and the timing difference between B and X (ejection time, T_{ET} in s) are used to calculate the local pulsatile blood volume ΔV_{blood} (in ml) using the equation suggested by Kubicek [28]:

$$\Delta V_{blood} = \rho \left(\frac{L}{R_{measured}} \right)^2 T_{ET} \frac{d}{dt} \Delta r_{MAX} \quad (6)$$

where ρ is the resistivity of blood which is taken as $135 \ \Omega \text{ cm}$, L (cm) is the distance between the voltage electrodes and $R_{measured}$ (Ω), is the measured resistance of the joint. The local blood flow rate \bar{Q}_{local} (in ml/min) is calculated using the equation $\bar{Q}_{local} = \Delta V_{blood} HR$. The cardiovascular features HR , ΔV_{blood} and \bar{Q}_{local} will be used in injury assessment as discussed previously.

2.3 System Verification Results and Discussion

2.3.1 Circuit Verification

The designed analog front-end was fabricated on a 78 mm x 90 mm printed circuit board, shown in Figure 4(a). The whole system was designed such that the analog front-end, the MSP430F5529 launch pad board, the SD card breakout board and the two 9V batteries stack on top of each other from bottom to top (65 mm tall). The modules were stacked rather than fabricated on the same printed circuit board in order to save board space.

To verify the calibration procedure, the measurements i_k and q_k were acquired from the four calibration loads mentioned previously using a 3024A oscilloscope (Keysight, Santa Rosa, CA). The calibration parameters were calculated using MATLAB. Static measurements $i(t)$ and $q(t)$ were acquired from the same loads, 10 times within a day. Using (3), the acquired voltage measurements were converted to impedance measurements using the calculated calibration parameters. The measured versus actual resistance (R) and reactance (X) of the loads are shown in Figure 4(b). The actual load impedances were measured using an Agilent 34410A 6 1/2 digit multimeter. A line was fitted for the R and the X measurements separately (red lines in Figure 4(b)). The impedance measurements made by the custom analog front-end were linear and consistent within the range $0 \ \Omega < R < 100 \ \Omega$ and $0 \ \Omega < -X < 70 \ \Omega$ ($R^2 \approx 1$ for both R and X).

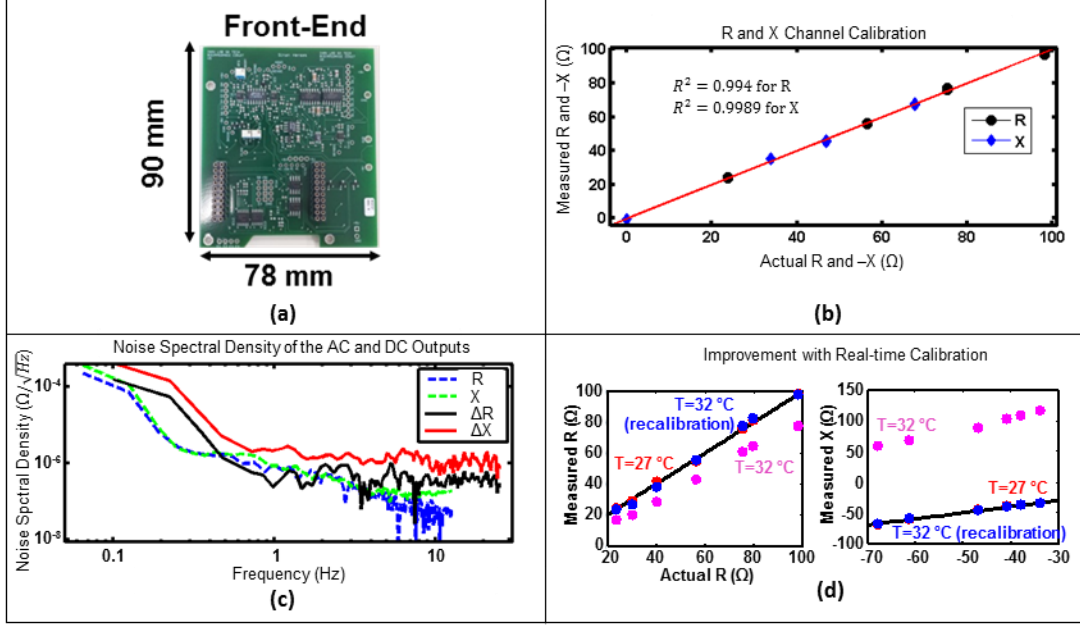


Figure 4: Circuit verification. (a) Photo of the printed circuit board (PCB) fabricated for the analog front-end. (b) Calibration of the resistance and reactance measurements demonstrated high linearity and consistency (points are shown for multiple measurements taken on different days). (c) Noise spectral density plots for dynamic impedance measurements (i.e. IPG). The total noise integrated from 0.8-20 Hz was found to be $18 \mu\Omega_{\text{rms}}$ for the resistive and $55 \mu\Omega_{\text{rms}}$ for the reactive dynamic components, lower than any other previously reported design in the existing literature. (d) Demonstration of improvement of calibration using the novel microcontroller-enabled automatic calibration methods described here.

To measure the relative error, four impedances, different then the calibration impedances but within the same impedance range, were used. The measured impedances were compared to those measured using the multimeter. The mean relative measurement errors were 3.9% for R , 5.9% for X , 1.4% for $|Z|$ and 1.8% for $\angle Z$.

Connecting a potentiometer to the circuit as a load, the dynamic range of the front-end was tested. The resistance at which the IA measuring across the potentiometer saturates, was defined as the dynamic range and was measured as 345Ω . The measured dynamic range covers the expected knee impedance values varying between 40Ω and 80Ω for R and -20Ω and -10Ω for X .

To calculate the input referred noise floor of the measured dynamic impedances, the noise spectral densities of $\Delta i(t)$ and $\Delta q(t)$ were acquired using an SR785 signal

analyzer (Stanford Research Systems, Sunnyvale, CA) with a $0\ \Omega$ load across the analog front-end. The cross spectra of $\Delta i(t)$ and $\Delta q(t)$ were also acquired. The voltage noise spectral densities were mapped to the noise spectral densities of $\Delta r(t)$ and $\Delta x(t)$ using (3) and (4). The resulting noise spectral densities are shown on Figure 4(c). As these spectra were calculated from the outputs of the circuit, they include the noise added by each stage. The noise floor was calculated for a bandwidth of 0.1–20 Hz. The resulting noise floors were $0.018\ \text{m}\Omega_{\text{rms}}$ for $\Delta r(t)$ and $0.055\ \text{m}\Omega_{\text{rms}}$ for $\Delta x(t)$.

The current consumption of the front-end was measured as 24.9 mA when supplied by $\pm 5\ \text{V}$ regulated from two 9 V batteries, leading to 0.249 W power consumption. The full system power consumption was measured as 0.36 W when sampling with the clock frequency set to 25 MHz and writing data to the SD card.

To demonstrate the effectiveness of the real-time calibration method, various series RC loads with known impedances were measured with the system while the analog front-end was at room temperature and heated up. The measurements were first performed when calibration was only done at room temperature. The PCB was then heated locally above the Wien Bridge oscillator. The temperature of the board was monitored using an RTD (HH126, Omega Engineering, Stamford, CT) and the load measurements were performed while the monitored temperature was stable. As seen on Figure 4(d), the measured R and X values showed large errors at 32°C because the calibration coefficients calculated at 27°C were no longer valid at this temperature. However, when re-calibration was performed at 32°C, the measured R and X values were accurate, demonstrating the benefit of real-time calibration in uncontrolled environments (e.g. the home).

To evaluate the system performance, the electronic and system specifications were compared against numerous bioimpedance measurement systems (see Table 1) [61-76]. The architectures used for these systems can be categorized as (i) computer assisted designs, (ii) application specific integrated circuits (ASICs), (iii) field programmable gate

array (FPGA) designs, and (iv) discrete designs. Computer-assisted systems such as [61-63] cannot be classified as wearable. ASIC systems such as [64-69] are advantageous due to their small size and low power consumption, but are expensive to prototype compared to discrete designs. FPGA based systems such as [70, 71] require high current levels, limiting their feasibility for wearable, continuous monitoring applications. Discrete designs such as [72-76] can provide an inexpensive, programmable alternative to existing approaches, can be rapidly prototyped and evaluated in human subjects testing, and – with the design described in this paper – can achieve sufficiently small size and low power consumption to serve as prototypes for wearable joint health monitoring systems.

In fact, as seen from Table 1, the proposed system has higher resolution in impedance measurements than all other bioimpedance measurement systems that reported their resolution [65, 69, 70]. The proposed system achieves 11-bits of effective resolution for a typical resistive peak-to-peak leg blood flow bioimpedance value of $100 \text{ m}\Omega_{\text{pp}}$ (based on [32], and Section 3.3.5.2) as opposed to 2-bits that can be achieved by the system in [70] while consuming an order of magnitude smaller power (0.36 W vs. 3.7 W). It should be noted that, the significance of resolution becomes more prominent when detection of smaller variations in blood flow due to physiological changes are of interest. The proposed system is the only one that has the resolution to detect the $\sim 20 \text{ m}\Omega_{\text{pp}}$ of change in pulsatile bioimpedance due to the cold-pressor test (8-bits of effective resolution) (Section 3.3.5.2). It is likely that any changes in local blood flow to the region following injury would be on the same order as the changes observed for the cold-pressor test, or even smaller. Compared with other systems in Table 1, our system is the only one (that can be deployed in a wearable device) enabling real-time calibration to minimize measurement errors due to environmental changes.

Table 1: Comparison of the electronic and system specifications of the system proposed in this work, with numerous other electrical bioimpedance measurement systems available in literature. ^aFS = Full system, FE = Front-end only; Noise RTI in [69] was calculated for a bandwidth of 20 Hz using the noise spectral density reported. ^bArchitecture sorted into four groups: (i) Computer-assisted architecture; (ii) ASIC; (iii) FPGA; (iv) Discrete design.

Ref.	Power Cons. (mW) ^a	Noise (RTI, $m\Omega_{rms}$)	Measurement Error	Dynamic Range (Ω)	Size	Architecture ^b	Functions
[61, 62]	-	-	Z :0.05 Ω $\angle Z$:0.003 $^\circ$	R: 100 – 1.1 k Ω	Non-wearable, PXI based	(i) PXI based synth. and demod.	Static / Dynamic Z and $\angle Z$, spectro.
[63]	-	-	R: 0.02 Ω	R: 100 Ω – 1 k Ω	Large, rack mounted modules	(i) Analog front end + computer	Static Z and $\angle Z$, spectro.
[64]	1.6 (FE)	-	-	Z : 1 Ω – 3.5k Ω $\angle Z$: 0 $^\circ$ – 90 $^\circ$	8 cm ² including antenna, wearable	(ii) ASIC	Static Z and $\angle Z$, spectro.
[65]	2.4 (FS)	100	-	-	5 mm ²	(ii) ASIC	Dynamic Z
[66]	14.4 (FS)	-	R:0.2 Ω X:0.2 Ω	R < 54 Ω X: 0.7 Ω – 15 Ω	4.8x3 cm ²	(ii) ASIC	Static R and X, spectro.
[67]	2.1 (FE)	-	-	Z : 100 Ω – 10k Ω $\angle Z$: 0 $^\circ$ – 30 $^\circ$	6.95 mm ²	(ii) ASIC	Static R and X, multi-freq.
[68]	3.4 (FS)	-	R,X: 5%	Z : 32 Ω – 5.3k Ω	1.52 mm ²	(ii) ASIC	Static R and X, multi-freq.
[69]	0.058 (FE) 0.345 (FS)	43.8	-	-	7x7 mm ²	(ii) ASIC	Static R
[70]	3700 (FS)	5	-	R < 3.2 k Ω	136x145 mm ²	(iii) FPGA based	Static / Dynamic Z and $\angle Z$, spectro.
[71]	-	-	Z :1.2% $\angle Z$: 0.18 $^\circ$	Z > 2 k Ω	-	(iii) FPGA based	Static Z and $\angle Z$
[72]	-	-	Z :1.1% $\angle Z$:1%	R > 10k Ω	-	(iv) AD5933 controlled by μC	Static Z and $\angle Z$, spectro.
[73]	-	-	R:1%	R: 50 Ω – 1.6 k Ω	Wearable	(iv) AD5933 based	Static R and X, spectro.
[74]	-	-	-	Z < 1k Ω	Portable	(iv) Discrete with sync. demod.	Static Z , Dynamic Z
[75]	-	-	Z :0.36 Ω $\angle Z$:0.0049 $^\circ$	Z : 9 Ω – 5.7k Ω $\angle Z$: 0 $^\circ$ – 180 $^\circ$	Handheld, 0.5 kg	(iv) AD8302 controlled by μC	Static Z and $\angle Z$, spectro.
[76]	546 (FS)	-	R:0.4 Ω X:0.3 Ω	-	145x40x4mm ³ , 30g	(iv) AD5933 based	Static R and X, spectro.
<i>This Work</i>	249 (FE) 360 (FS)	0.018	R:3.9% X: 5.9% Z :1.4%, $\angle Z$: 1.8%	Z < 345 Ω	78x90x65 mm ³	(iv) Discrete with, sync. demod.	Static and Dynamic R, Static and Dynamic X

2.4 Conclusion

This chapter describes a discrete design for high resolution electrical bioimpedance measurements from the knee joint based on embedded systems concepts. The combined use of high performance analog front-end electronics and digital programmability using a microcontroller allow high quality static (slowly varying over the course of hours to days) and dynamic (rapidly varying on the order of milli-seconds) impedance measurements on a platform that serves a system-level biomedical proof-of-concept. The overall system was designed from end-to-end, including the design of the circuit and customized physiology-driven algorithms for detecting features from the measured signals. A future wearable system based on the engineering foundation presented in this paper can enable high resolution, quantitative assessment of both the structural and hemodynamic characteristics of the knee joint longitudinally for the first time, paving the way to better understanding joint recovery physiology, and designing closed-loop personalized therapies to accelerate the recovery process. The ability of the designed system in monitoring knee joint health is demonstrated in the next chapter of this work.

CHAPTER 3: VALIDATION OF THE ELECTRICAL BIOIMPEDANCE SYSTEM IN THE CONTEXT OF KNEE JOINT HEALTH MONITORING

3.1 Introduction

In this chapter, a comprehensive validation of the electrical bioimpedance (EBI) measurement system designed is presented, in the context of knee joint health monitoring. A series of human subject studies are carried out for this purpose: (1) a study on 49 subjects (42 healthy, 7 injured) to validate the performance of the technology in quantifying physiological differences in the knee; (2) a study of the inter-day measurement variability to determine the minimum bioimpedance change that can, with confidence, be attributed to edema as compared to measurement error; (3) a physiological perturbation study aimed at creating small changes in local interstitial fluid volume in the knee based on modulating tissue temperature to quantify the sensitivity of the vector EBI system; (4) a study aimed to evaluate the validity of the cardiovascular features calculated using dynamic EBI signals, acquired by the proposed system, from the knee joint; (5) a demonstration of the sensitivity of the dynamic EBI measures, with a cold-pressor test.

3.2 Bioimpedance Measurement Setup and Electrode Placement

The custom analog front-end detailed in Section 2.2.1 was used for all bioimpedance measurements. The static in-phase and quadrature signals ($i(t)$ and $q(t)$ respectively), their dynamic counter-parts ($\Delta i(t)$ and $\Delta q(t)$) and the current amplitude monitoring signal ($A(t)$) measured using the analog front-end, were recorded using an MP150 Data acquisition system (Biopac Systems Inc., Goleta, CA) with a sampling rate of 2 kHz. The signal, $A(t)$, was used to rescale the static and dynamic voltage signals using (1), so that

any variations in the current amplitude were cancelled out (amplitude correction). The amplitude corrected static voltage signals were then calibrated using (3), to give the static resistance ($r(t)$) and reactance ($x(t)$) signals. The amplitude corrected dynamic voltage signals were calibrated using (4), to get the dynamic resistance ($\Delta r(r)$) and reactance ($\Delta x(t)$) signals. The amplitude correction and calibration steps were carried out using MATLAB (Mathworks, Natick, MA).

Standard wet gel (Ag / AgCl) adhesive backed electrodes (2660-3 Red dot electrodes, 3M, Maplewood, MN) were positioned on the subjects' legs as shown in Figure 5. The proximal current electrode (E1) was placed 7.6 cm above the crease on the quadriceps tendon, towards the medial side of the knee. The distal current electrode (E4) was placed 7.6 cm below the popliteal fossa, towards the lateral side of the knee. The voltage electrodes (E2, E3) were placed adjacent to the current electrodes.

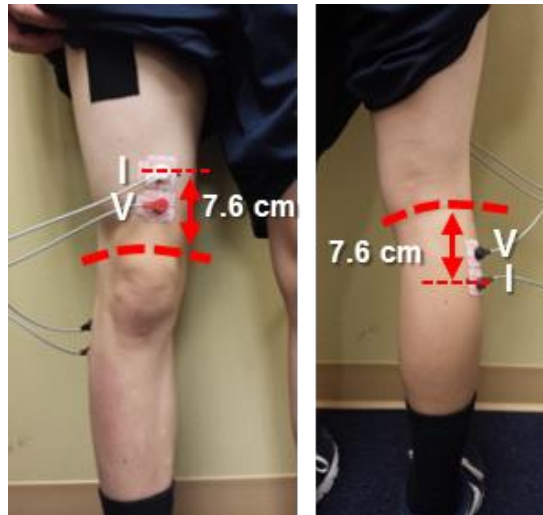


Figure 5: Placement of the wet gel (Ag/AgCl) electrodes for electrical bioimpedance measurements. The outer electrodes (E1 and E4) are current electrodes and the inner ones (E2 and E3), are voltage electrodes.

3.3 Human Subject Studies

Five separate human subject studies were conducted to assess the bioimpedance measurement system and the designed algorithm. All human subject studies were

approved by the Georgia Institute of Technology Institutional Review Board (IRB) and the Army Human Research Protection Office (AHRPO).

3.3.1 Discriminating Healthy versus Injured Knees and Monitoring Longitudinal Injury Recovery

3.3.1.1 Measurement Protocol

In the first test performed, the bioimpedance measurement system was used to acquire measurements from 49 subjects. Out of these subjects, 42 were healthy, control subjects (27 male, 15 female) with no history of recent injury to any knee. Seven subjects (six male, one female) had a recent acute, unilateral knee injury (within one month before the measurement date), requiring subsequent corrective surgery (torn anterior cruciate or medial collateral ligament, and / or lateral meniscus). All injured subjects and 36 of the healthy subjects were college athletes.

Standard wet gel (Ag / AgCl) electrodes were positioned on each subject's legs as shown in Figure 5. Each subject was asked to sit with his back against the wall, legs extended forward and supported from the bottom. While the subject sat still (to rule out motion artifacts), the signals were recorded on a laptop using the MP150 data acquisition system (Biopac Systems, Goleta, CA). Measurements were taken from both knees of each subject.

Later, the static in-phase and quadrature voltage signals were amplitude corrected and calibrated to get the static resistance and reactance signals. The mean of these signals over 60 seconds was taken to compute knee resistance and reactance of a given subject. This protocol was repeated on the seven injured subjects, on one occasion several months (4-7) after corrective surgery was performed and the subjects were rehabilitated to the point where they could resume functional activities.

3.3.1.2 Results and Discussion

The bioimpedance measurement results obtained for the first study are shown in Fig. 2(a). The difference in resistance between the knees for the healthy subjects (left minus right) was $1.9 \pm 5.6 \Omega$. The difference in reactance was $-1.1 \pm 2.4 \Omega$. The difference in resistance between the knees (injured side minus healthy side) for the injured subjects was $-11.8 \pm 4.5 \Omega$. The difference in reactance was $4.9 \pm 2.6 \Omega$. The absolute differences in resistance between the knees for the healthy subjects (left vs. right knee) were $4.9 \pm 3.3 \Omega$ while for injured subjects were $11.8 \pm 4.6 \Omega$ ($p < 0.05$, two sample t-test with unknown and unequal variances). Similarly, the absolute difference in reactance between the knees were $2.2 \pm 1.4 \Omega$ for the healthy subjects and $4.9 \pm 2.6 \Omega$ for the injured subjects ($p < 0.05$, two sample t-test with unknown and unequal variances).

For all of the injured subjects, the affected knee had lower resistance than the healthy one. For all but one injured subject, the affected side had a higher reactance (lower negative reactance) than the healthy one; the one outlier injured subject had almost no difference (0.02Ω) in reactance between the knees.

The effect of injury recovery on the difference in impedance between the knees is shown on Figure 6. The difference in resistance between the knees for the injured subjects (injured side minus healthy side) decreased from $-11.8 \pm 4.5 \Omega$ when the injury was acute (within a month of the injury date) to $-1.0 \pm 4.0 \Omega$ during recovery (four to seven months after corrective surgery). The difference in reactance decreased from $4.9 \pm 2.6 \Omega$ to $2.3 \pm 2.0 \Omega$. Furthermore, the absolute difference in resistance between the knees decreased from $11.8 \pm 4.6 \Omega$ to $3.6 \pm 1.7 \Omega$ ($p < 0.05$, two sample t-test with unknown and unequal variances).

The estimated probability density for the difference in resistance and difference reactance between the knees (left minus right) is also shown in Fig. 2(b). The probability density estimation was done using Gaussian kernel density estimation where the bandwidth is estimated using Scott's rule [77]. This kind of visualization helps show how

the injured subjects' data points move toward where the healthy subjects' data points are denser, as recovery occurs.

The results seen for the knee resistances were consistent with expected physiological changes, as edema commonly accompanies injuries and local excess fluid accumulation results in lower tissue resistance. The injected current at 50 kHz flows through both extracellular and intracellular space [57], however, we cannot differentiate the contribution of either fluid space to the resistance change measured. Tissue resistance has also been argued to be proportional to new tissue growth and to fibrin clotting which are processes that occur during wound healing [54]. Therefore, as the edema decreases and injured tissue repair occurs during injury recovery, the injured knee's resistance increases and the absolute difference in resistance between the injured and healthy knees decreases.

Tissue reactance is related to cell membranes as they are made of lipid layers which have a capacitive effect. Negative reactance increases with cell mass and cell wall integrity which can both decrease (thus elevating reactance) due to injury [54]. Therefore, the observed knee's reduced reactance after injury is consistent with anticipated physiological changes as well. The results presented also agree with previous studies existing on assessing knee or lower limb health using bioimpedance [25, 78-80].

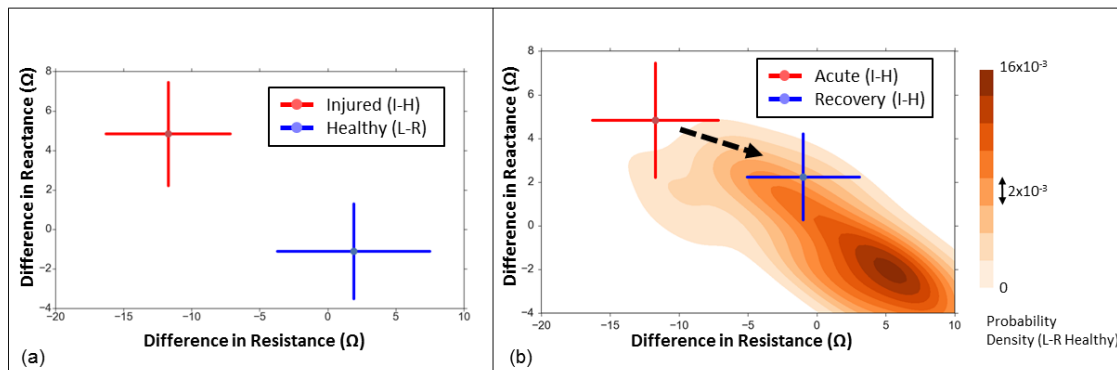


Figure 6: Discriminating healthy versus injured knees and monitoring longitudinal injury recovery using static EBI measurements. (a) The difference in resistance versus the difference in reactance for the healthy and injured subjects. For the healthy subjects

(shown in blue, N=42), the difference is that between the left and the right knee (L-R) and for the injured subjects (shown in red, N=7) it is that between the injured and the healthy knee (I-H). The error bars indicate one standard deviation. (b) The difference in resistance versus the difference in reactance for the injured subjects (N=7), when the injury is acute (within one month of the measurement take, shown in red) and during recovery (four to seven months after corrective surgery, in blue). For these subjects, the difference shown is I-H. The probability density of the healthy subjects' data (N=42, L-R difference), estimated using 2-dimensional Gaussian kernel density estimation is also visualized in shades of orange for comparison. The error bars indicate one standard deviation.

3.3.2 Day-to-Day Variability in EBI Measurements

3.3.2.1 Measurement Protocol

A second test was performed to investigate the day-to-day variability of the knee impedance measures. EBI measurements were acquired from five healthy subjects for three days within a week under standard conditions (e.g., no previous exercise and same time of day). The electrodes and electrode configuration in Section 3.2 were used and measurements were taken from both knees. Signals were acquired while the subject sat still, with their back against the wall, legs extended and supported from the bottom. Since the human study outlined in Section 3.3.1 indicated that the difference in resistance from left to right knee was an important parameter for separating healthy from injured knees, the day-to-day variability in this parameter in particular was quantified.

3.3.2.2 Results and Discussion

Knee bioimpedance measurements taken from five subjects in three different days (within a week) showed that the average day-to-day variability (standard deviation) of the absolute difference in knee resistances were 2.5Ω . The average day to day variability for the absolute difference in reactance was 1.2Ω . Therefore changes in knee impedance exceeding these values can be attributed to reasons other than measurement errors (e.g. edema).

3.3.3 Investigating Effects of Local Heating/Cooling on EBI

3.3.3.1 Measurement Protocol

A third test was performed for seven healthy subjects to investigate the effects of local tissue heating and cooling on knee bioimpedance. Tissue (skin and muscle) heating will decrease pre- to post-capillary resistance ratios thus resulting in net capillary filtration and increasing interstitial fluid, while local cooling will have the opposite effect [81]. In this test, the subject's knee bioimpedance was recorded (with the same electrodes, electrode placement and subject positioning as the test in Section 3.3.1.1) while the knee was locally cooled using a standard ice-pack (Pro-Tec Athletics, Richmond WA) on the anterior patella for 20 minutes. Skin temperature on the patella was measured using a resistance temperature detector (SA2C-RTD-3-1000-A, Omega Engineering, Stamford, CT). The temperature was logged using a data logger (HH126, Omega Engineering, Stamford, CT) with a sampling rate of 1 Hz. After waiting for the skin temperature to return to its baseline value, the test was repeated with a hot pack (Chattanooga Medical Supply Inc., Chattanooga, TN).

3.3.3.2 Results and Discussion

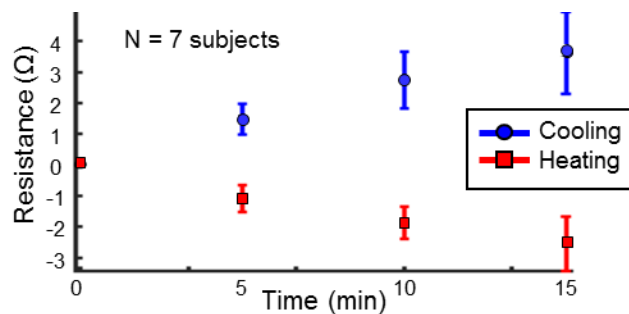


Figure 7: Mean knee resistances for seven subjects during heating (in red) and cooling (in blue) along with the standard deviations (shown in error bars). Note that each subject's baseline knee resistance (at time=0 minutes) was subtracted from the rest of their measurements to emphasize the change in knee resistance with heating/cooling. The data points shown are at 0,5,10 and 15 minutes into heating/cooling. The skin temperatures at the patella, at these time instances during heating were: $25.7\pm 3.0^{\circ}\text{C}$, $34.7\pm 2.8^{\circ}\text{C}$, $36.1\pm 1.8^{\circ}\text{C}$ and $36.1\pm 1.4^{\circ}\text{C}$. The temperatures for cooling were: $25.6\pm 1.3^{\circ}\text{C}$, $19.5\pm 2.7^{\circ}\text{C}$, $18.3\pm 3.1^{\circ}\text{C}$ and $18.0\pm 3.3^{\circ}\text{C}$.

The results for the local tissue heating/cooling test are shown in Figure 7. The mean knee resistance has been shown with error bars at 0 (baseline), 5, 10, 15 minutes into the heating/cooling for the seven subjects. Note that for each subject, the baseline knee resistance was subtracted from the measured resistance to show the deviation from the baseline. The difference between the baseline resistances for the subjects and the resistances measured at 5, 10 and 15 minutes was statistically significantly different than the baseline resistances ($p < 0.01$, two-sample t-test with unequal and unknown variances) for both heating and cooling. The skin temperature at the patella, at these time instances during heating were: $25.7 \pm 3.0^\circ\text{C}$ (baseline), $34.7 \pm 2.8^\circ\text{C}$, $36.1 \pm 1.8^\circ\text{C}$ and $36.1 \pm 1.4^\circ\text{C}$, respectively. The temperatures for cooling were: $25.6 \pm 1.3^\circ\text{C}$ (baseline), $19.5 \pm 2.7^\circ\text{C}$, $18.3 \pm 3.1^\circ\text{C}$ and $18.0 \pm 3.3^\circ\text{C}$, respectively. Though the temperature values are similar, for the third and fourth data points during heating and cooling respectively, these skin temperatures were held for an additional five minutes between the third and fourth data points; accordingly, the temperature within the tissue itself continued to increase (or decrease for cooling) throughout the measurement. The temperature data points also demonstrate that the heating or cooling rate of the patella, decreased with time, approaching zero towards the fourth data point.

Modulation of tissue temperature should cause changes in the local interstitial fluid volume. Heating will decrease the pre- to post-capillary resistance ratios causing net capillary filtration, while cooling will increase the pre- to post-capillary resistance ratio and thus cause net capillary absorption [81]. Figure 7 demonstrates that the EBI measures were sufficiently sensitive to detect the small theoretical changes in interstitial fluid volume with local heating (increased interstitial fluid) and cooling (decreased interstitial fluid). It can be noted as the skin and underlying tissue progressively warmed or cooled, an expected progressive change in resistivity was observed. This demonstrates that the bioimpedance measurement system is sufficiently sensitive to detect small changes in interstitial fluid (edema) corresponding to a few Ohms change in tissue resistance.

These results also suggest that changes in knee temperature due to environmental factors (e.g. hot or cold weather) or activity (e.g. exercise) is expected to effect EBI measurements. This suggests that the a temperature sensor would be a good addition to a future wearable device for knee joint health monitoring. Such a sensor could be used to gate the EBI signals such that measurements are accepted, only when the knee temperature is within certain limits. This will allow the measurements taken in a wearable setting to be more consistent.

3.3.4 Evaluating the Validity of Cardiovascular Features Computed Using the Dynamic EBI

3.3.4.1 Measurement Protocol

A test was performed on seven subjects with no recent history of injuries to the knees in order to evaluate the ability of the proposed system in computing various cardiovascular features, using the dynamic EBI signals obtained from the knee joint. The electrode configuration and subject positioning used was identical to that in Section 3.3.1.1. To evaluate the ensemble averaging algorithm and the cardiovascular features computed using the dynamic knee EBI signals, ECG signals from the subjects were acquired using a BioNomadix (Biopac Systems Inc, Goleta, CA) wireless ECG acquisition module.

While the subject was still, 60 seconds of EBI and ECG signals were acquired. The measurement was repeated for the other knee of the subject as well. For pulsatile blood volume calculations, the distance between the voltage electrodes on each knee were measured.

The pre-processing and feature extraction algorithms described in Section 2.2.3, were used to calculate the cardiovascular features HR, ΔV_{blood} and \bar{Q}_{local} for the human subjects tested. These features were also calculated using an ECG-assisted ensemble averaging algorithm for comparison.

3.3.4.2 Results and Discussion

The signals obtained at intermediate and final steps of the ensemble averaging algorithm, detailed in Section 2.2.3, are presented in Figure 8(a). The accurate detection of heart beats enabled the dynamic (IPG) impedance signals to be segmented accurately. Therefore, high SNR waveforms were obtained after ensemble averaging leading to clear detection of B, C, and X points.

It was observed that the cardiovascular features calculated using the dynamic EBI signals obtained from 14 knees (seven subjects), with and without the ECG were consistent (Figure 8(b)) with no statistically significant differences observed.

The results presented indicate that, the proposed EBI measurement system can quantify local blood flow patterns, without the necessity of a reference signal such as the ECG. In addition to quantifying edema with static EBI, quantifying the local blood flow patterns following a joint injury with IPG could provide significant insight into joint rehabilitation progress. An increase in local blood flow may follow an injury to the joint, associated with inflammation and scar tissue formation, while decrease in local blood flow may be indicative of improving status [38].

3.3.5 Demonstrating the Sensitivity of the Dynamic EBI Measures to Minute

Changes in Local Blood Flow

3.3.5.1 Measurement Protocol

For one of the subjects, a separate experiment was performed to examine the effects of vasoconstriction on the dynamic impedance signal measured from one knee. The methodology was analogous to a cold pressor test [82], with the subject's bare foot being submerged in ice water, to increase downstream peripheral vascular resistance (PVR). The purpose of this experiment was to evaluate the sensitivity with which the system

developed in this work could detect minute changes in knee joint blood flow associated with modified downstream PVR.

The subject's skin temperature was measured on the bare foot prior to submerging and found to be 30 °C. The impedance signals were acquired from the knee for 60 seconds with the electrode and subject positioning in Section 3.3.1.1. The foot of the same side was immersed into ice water until the foot skin temperature dropped to 17 °C. The foot was taken out of the cold water and impedance signals were again recorded for 60 seconds from the knee in the same position as before. The dynamic resistance signals before and after immersion, were compared.

3.3.5.2 Results and Discussion

A plot of the resistance signal ensemble averaged using the algorithm described in Section 2.2.3 ($\Delta r_{EA}(t)$) and its derivative ($\frac{d}{dt} \Delta r_{EA}(t)$) taken using a Savitzky-Golay filter are shown on Figure 8(c). The minute changes in this IPG signal associated with downstream vasoconstriction can be observed on both waveforms as a significant drop in amplitude (20 m Ω decrease for the resistance, and 0.2 Ω/s decrease for the time derivative of resistance). Accordingly, the system was sufficiently sensitive to detect both the reduction in local blood volume pulse and blood flow with increased PVR, consistent with physiological expectations.

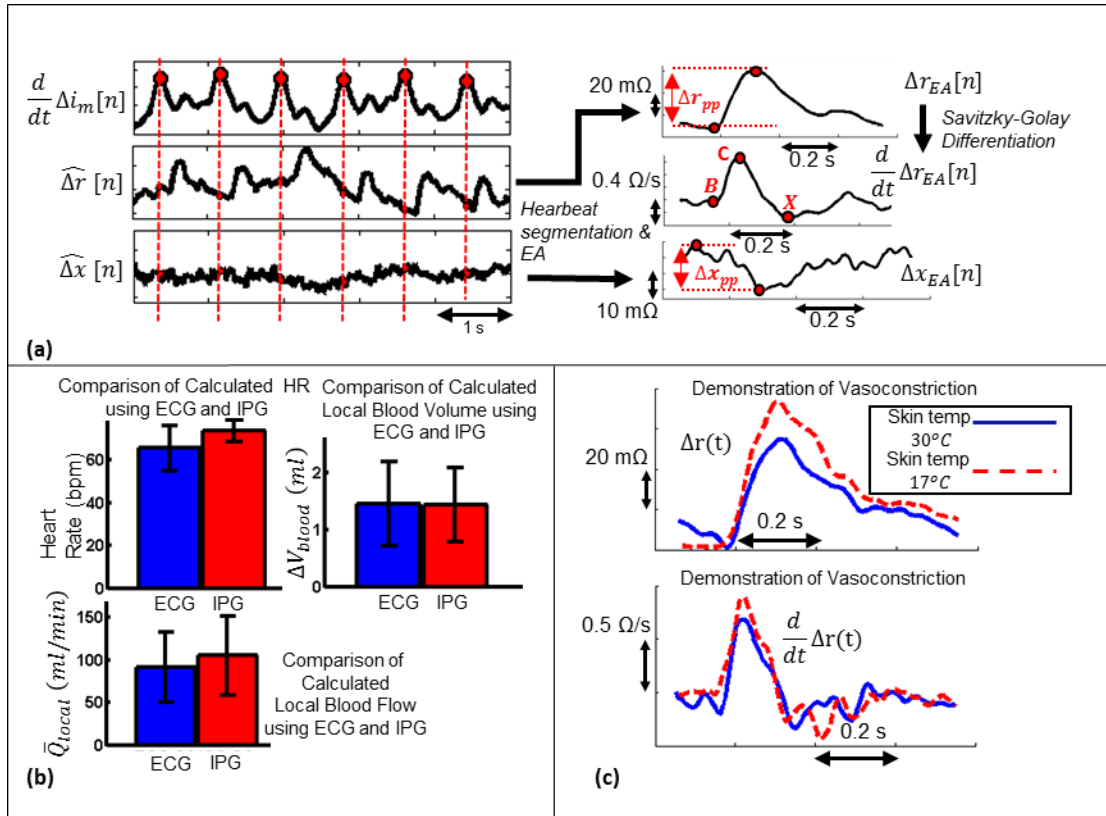


Figure 8: Human subject study results related to the dynamic EBI measures. (a) Example waveforms from the intermediate stages of the preprocessing and the feature extraction. (b) Comparison of extracted features using ECG-based vs. IPG-based ensemble averages. (c) Evaluation of the system in response to changes in physiology (vasoconstriction after 2 min. cold pressor test).

3.4 Conclusion

In this chapter, the ability of the proposed EBI measurement system in acquiring physiologically relevant measurements from the knee joint is demonstrated. Human subject experiments were used to demonstrate how the knee impedance measured using the system provides information related to knee joint edema and injury, along with longitudinal changes during recovery. A validation study was conducted to show the ability of the measurement system in detecting small changes in interstitial fluid volume due to local tissue heating or cooling, demonstrating the sensitivity of the measurement system to small changes in interstitial fluid volume. The validity and sensitivity of the system in monitoring local blood flow was demonstrated.

The work presented so far, on the use of EBI measurements for knee joint health monitoring, was limited to controlled laboratory settings where an initial proof-of-concept system was used. The ultimate goal is to provide a wearable system for long-term use following musculoskeletal injury and provide feedback to the user to titrate care. In the next chapter, steps towards translating the technology developed to wearable, uncontrolled settings are described.

CHAPTER 4: TRANSLATION OF THE ELECTRICAL BIOIMPEDANCE MEASUREMENT SYSTEM TO WEARABLE, UNCONTROLLED SETTINGS

4.1 Introduction

One limitation of the implementation presented that must be overcome in translating these technologies to wearable, daily measurements is the signal degradation due to motion artifacts that will be present in unsupervised conditions (e.g., in the home). The approach presented in this chapter uses inertial sensing as guidance to automatically gate the bioimpedance measurements only during periods of “low” motion, when the signals can be of high quality and reliability.

A second limitation that must be addressed is the use of gel electrodes with adhesive. In this chapter, the system is interfaced to dry (copper) electrodes [83], which are more amenable to a wearable form factor. The reliability of the dry electrodes, in acquiring EBI measurements similar to those acquired using wet gel electrodes is presented.

4.2 Position Identification Algorithm

Bioimpedance measurements are greatly impacted by motion artifacts and subject position [84-86]. The ultimate goal is to design a wearable system that can be used outside of laboratory / clinical settings, and thus must be “smart” in that it can automatically identify times at which the body position is such that robust, and consistent, EBI measurements can be obtained. An algorithm that can detect such instants in time based on signals from two dual axis accelerometers, placed laterally on the thigh and shank (Figure 9(a)) was developed. The EBI signals are then gated by determining

instances where the subject is still and in a certain position, using information obtained from the accelerometers.

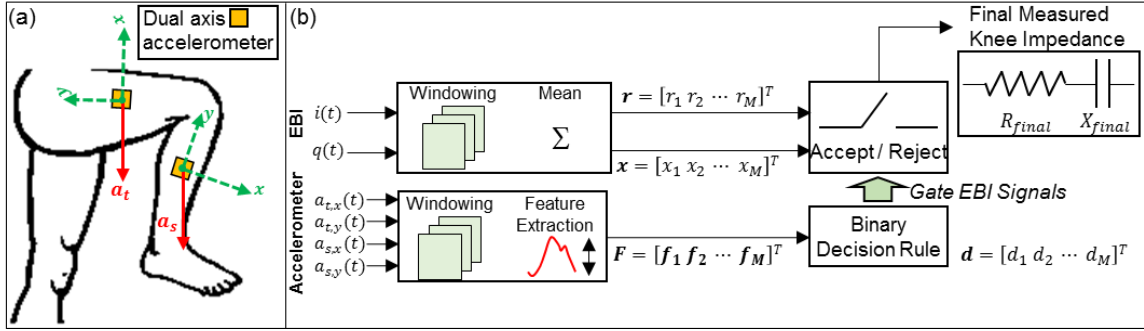


Figure 9: (a) Accelerometers placed on the thigh and the shank, are used to gate the EBI signals. The acceleration vector obtained from the accelerometer on the thigh is: $\mathbf{a}_t = [a_{t,x} \ a_{t,y}]^T$. That obtained from the shank is: $\mathbf{a}_s = [a_{s,x} \ a_{s,y}]^T$. (b) Algorithm for identifying the time intervals when the user is in the optimal position to acquire measurements (sitting, legs extended and supported). The acceptable time intervals are identified by extracting features from the dual axis accelerometer signals ($a_{t,x}(t)$, $a_{t,y}(t)$, $a_{s,x}(t)$, $a_{s,y}(t)$) and using these features to make a decision. The binary decision rule is trained once before-hand. The accepted time intervals are used to obtain the knee resistance (R_{final}) and reactance (X_{final}) using the voltage signals $i(t)$ and $q(t)$.

The signals from the dual axis accelerometers placed on the thigh ($\mathbf{a}_t(\mathbf{t}) = [a_{t,x}(t) \ a_{t,y}(t)]^T$) and the shank ($\mathbf{a}_s(\mathbf{t}) = [a_{s,x}(t) \ a_{s,y}(t)]^T$) are used, to determine a consistent body position for measurement: seated posture with legs fully extended and supported (as in the experiments presented in Section 3.3). This position is preferred for EBI measurements as it provides a completely unloaded and easily repeatable position, which will reduce artifacts and variability in measurements. The position identification algorithm is summarized in Figure 9(b) and includes windowing (10 sec windows, 50% overlap), feature extraction, and binary classification. Features extracted from each ten second frame are used to label the frame as reject (0) meaning the subject is not in the desirable position described above or accept (1). The labels for these frames are then used to determine which resistance/reactance measurements can be assumed as robust and thus stable.

The binary decision rule mentioned is trained separately before it is applied to new data (a testing set). For this training, the signals from the two accelerometers are recorded from multiple subjects (six in our case), while the subject performs the following activities with known labels: (1) standing (label 0), (2) sitting legs bent (label 0), (3) sitting legs crossed (label 0), (4) sitting legs extended and supported (label 1) and (5) walking (label 0) each for 1 minute. The subjects perform a combination of the listed activities for 13 minutes, where for approximately three minutes, the subject is sitting with legs extended and supported. Feature extraction is performed on the accelerometer signals from the six subjects as shown on Figure 9(b) to produce a feature vector $\mathbf{F}_{training}$ and the corresponding known labels $\mathbf{d}_{training}$.

Exhaustive grid search with leave-one-subject-out (LOSO) cross-validation is used to determine the set of hyper-parameters and kernel to be selected for the support vector machine (SVM) classifier to be trained [87, 88]. The kernels considered in the search are linear and radial basis function (RBF) kernels. The set of values considered for the hyper-parameter C are numbers logarithmically spaced between 10^{-2} and 10^3 for both kernels. The γ parameter for the RBF kernel is chosen from the set $\{10^{-4}, 10^{-3}, 10^{-2}\}$. A kernel and a value for C (and γ if the RBF kernel is selected) is chosen and the LOSO cross-validation accuracy score of the model is computed using $\mathbf{F}_{training}$ and $\mathbf{d}_{training}$. The same procedure is repeated for all combinations of kernels, C values and γ values (for models where the kernel is RBF). The model that maximizes the LOSO cross-validation accuracy within the models included in the search is selected. Finally an SVM classifier with the selected kernel and hyper-parameter(s) is trained on $\mathbf{F}_{training}$ and $\mathbf{d}_{training}$ resulting in the binary decision rule to be used. The training and model selection is done once and is expected to generalize well for new subjects. SVM was chosen as a classification algorithm as it provides many degrees of freedom in model selection by allowing the use of various kernels and multiple hyper-parameters (C and γ).

An exhaustive grid-search is used to be able to select the one that will generalize the best, from the set that is considered. The model selection and SVM training steps are carried out using the Scikit-learn library for the Python programming language.

The features extracted for each frame are the mean and the standard deviation of each of the four accelerometer signals ($a_{t,x}(t)$, $a_{t,y}(t)$, $a_{s,x}(t)$, $a_{s,y}(t)$) resulting in eight features per frame. The feature extraction stage was performed in MATLAB.

4.2.1 Human Subject Study and Measurement Protocol

Experiments were performed with seven healthy subjects to evaluate the position identification algorithm. Dual axis accelerometers (ADXL203EB, Analog Devices, Norwood, MA) were placed on the subjects' right leg as shown on Figure 10(a). The accelerometer on the thigh was placed 15.2 cm above the crease on the quadriceps tendon on the lateral side of the knee. The accelerometer on the shank was placed 15.2 cm below the crease on the popliteal fossa at the lateral side of the knee as well. The accelerometers were held in place using Kinesio Tex tape. The electrodes and electrode configuration used were the same as described in Section 3.2 and repeated in Figure 10(a). The accelerometer and EBI signals were recorded from each subject while the subject performed the following activities; (1) standing, (2) sitting legs bent, (3) sitting legs crossed, (4) sitting legs extended and supported (the acceptable position) and (5) walking, for one minute each. A combination of these activities was performed for 13 minutes, where the subject performed (4) for approximately three minutes (one minute at a time). LOSO cross-validation was performed to assess the performance of the designed position identification algorithm.

For each subject to be used for testing, an SVM classifier was trained using the data from all other subjects (training subjects). The SVM model (kernel and hyper-parameters) was determined by running cross-validated grid search on the training subjects (nested cross-validation [88]). The model was tested on the testing subject and

the accuracy and precision were calculated. The resistance and reactance signals for the testing subject were gated using the predicted labels such that the frames labeled “1” were kept and the rest were removed. The variability of the resistance and reactance signals across frames was computed both when gating was performed and not performed. This comparison was done to demonstrate how gating reduces measurement variability and increases consistency. The train-test procedure was repeated for all subjects and the accuracy, precision and variability metrics were averaged across the LOSO cross-validation folds.

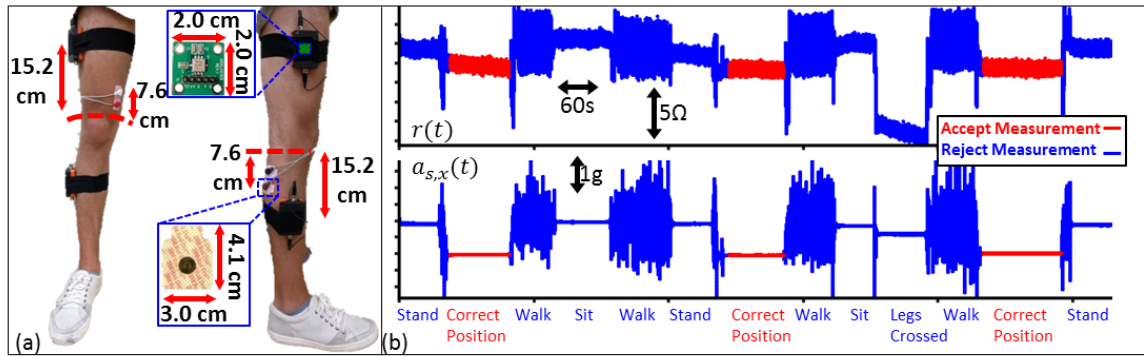


Figure 10: (a) Electrode positioning using wet Ag/AgCl electrodes as well as the positioning used for the two dual axis accelerometers. (b) The resistance ($r(t)$) signal and the x-axis shank acceleration signal ($a_{s,x}(t)$) measured from a subject during various activities. The time intervals marked in red are when the subject is in the correct position for taking measurements (sitting, legs extended and supported). The measurements taken when the subject is in the correct position are to be accepted, all other measurements (shown in blue) should be rejected.

4.2.2 Results and Discussion

The static resistance signal and the x-axis acceleration signal from the accelerometer on the shank ($a_{s,x}(t)$) are shown on Figure 10(b). The time intervals where the subject is in the correct position (seated, legs extended and supported) for the measurement to be acceptable are shown in red, while all others are shown in blue: subject standing, seated with legs bent 90° , seated leg crossed, walking). The dependence of the resistance signal on knee posture and the variability of the signal due to motion can be seen on this figure. It can also be seen that the mean value of $a_{s,x}(t)$ within a given window can be a good

indicator of the subject's knee posture, while the standard deviation of $a_{s,x}(t)$ can be a good indicator of the presence of motion artifacts. Similar arguments can be made about the mean and standard deviations of the signals $a_{s,y}(t)$, $a_{t,x}(t)$ and $a_{t,y}(t)$; justifying the use of these features in the position identification algorithm.

The LOSO cross-validated accuracy of the algorithm proposed in Section 4.2 and tested as described in Section 4.2.1 was $97.4 \pm 2.6\%$. The baseline misclassification rate (when the most probable class, reject (0), is always chosen) was 71.4%, and the accuracy achieved using the aforementioned algorithm was considerably higher. The LOSO cross-validated precision of the algorithm was $98.2 \pm 2.8\%$. The standard deviation of the resistance signal without gating as discussed in 4.2.1, averaged over all subjects was $3.3 \pm 1.2\Omega$ (range: 1.7Ω - 5.5Ω). With the application of the algorithm and gating, the averaged standard deviation dropped to $0.5 \pm 0.3\Omega$ (range: 0.2Ω - 1.2Ω). The standard deviation of the reactance signal without gating, averaged over all subjects was $0.8 \pm 0.5\Omega$ (range: 0.4Ω - 1.2Ω) and with gating it dropped to $0.2 \pm 0.1\Omega$ (range: 0.1Ω - 0.3Ω). The signals obtained using gating were less variable due to consistent subject positioning.

Consistent subject positioning in EBI measurements are critical in order to eliminate posture and motion related signal variability, which can blur the changes in the signals due to physiological effects. This consistency is established in the experiments in Section 3.3, by user guidance. The results presented in this section are a demonstration of how accelerometers can be used to automatically decide to take EBI measurements when the subject is in a certain position, eliminating the need for user guidance. An algorithm requiring a one-time offline training similar to this can be implemented on a smart phone that wirelessly communicates with the bioimpedance hardware, which is a step towards creating a "Smart Brace" monitoring knee impedance.

4.3 Evaluation and Design of a Knee Wrap with Integrated Dry Electrodes

A dry-electrode integrated knee wrap was designed as a step in transitioning the EBI measurement system to a wearable setting. The design is shown in Figure 11(c). The wrap consists of two wraps, each containing the proximal (E1 and E2) and distal (E3 and E4) electrodes. Each electrode consists of five 4.1 cm by 3.0 cm rectangles cut out of plastic and covered with copper tape, that are electrically shorted to each other. The reliability of the dry-electrode integrated knee wrap in acquiring static EBI measurements similar to those acquired using wet gel electrodes was tested in a human subject study.

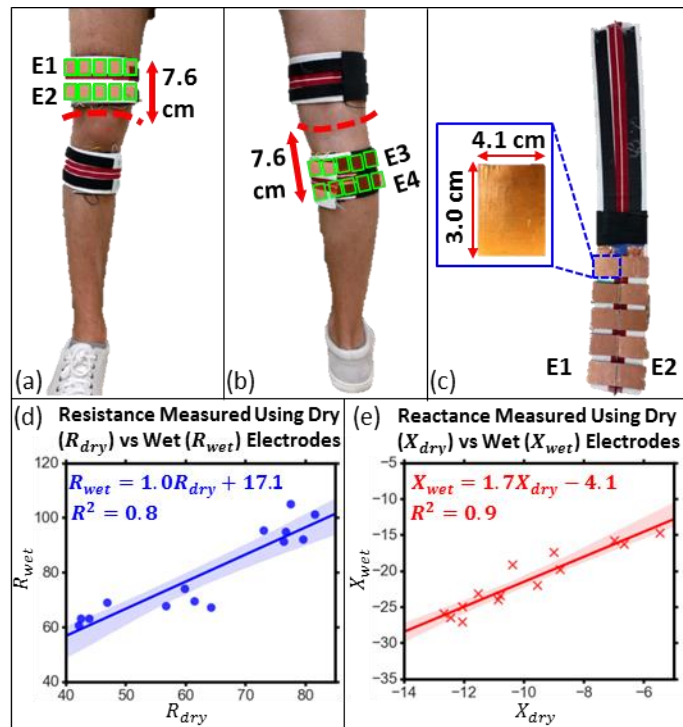


Figure 11: (a) Electrode placement for the knee wrap with integrated dry copper electrodes. The electrode positions inside the wrap are indicated using green rectangles. (c) Dry, copper electrodes integrated into a knee wrap. Each electrode is made of five 4.1 cm by 3.0 cm rectangles cut out of plastic, covered with copper tape. (d) Resistance measured using dry electrodes (R_{dry}) versus that measured using wet electrodes (R_{wet}) along with the linear regression line and the 95% confidence interval for the regression shaded. (e) Reactance measured using dry electrodes (X_{dry}) versus that measured using wet electrodes (X_{wet}) along with the linear regression line and the 95% confidence interval for the regression shaded.

4.3.1 Human Subject Study and Protocol

An experiment was performed with seven healthy subjects to demonstrate the usability of the bioimpedance measurement system with dry electrodes integrated into a knee brace. For this test, bioimpedance signals were acquired from a subject using the Ag/AgCl wet gel electrodes and electrode configuration detailed in Section 3.2, while the subject was seated, with legs extended and supported from the bottom, for 60 seconds. Then the subject was asked to wear the designed knee wrap as shown in Figure 11(a) and (b). The brace was positioned such that, the copper electrodes were at similar positions to the ones in the prior tests done using wet gel electrodes. Signals were acquired while the subject was still, in the same position for 60 seconds. The signals were amplitude corrected and calibrated to get the resistance and reactance signals measured using wet and dry electrodes.

4.3.2 Results and Discussion

Another step towards the smart wrap for knee impedance monitoring is to test functionality with dry electrodes rather than wet electrodes. Wet Ag/AgCl electrodes are less suitable for a wearable system as they are disposable and need to be replaced frequently; dry electrodes on the other hand are more durable. However, dry electrodes are more challenging to use due to higher skin-electrode interface impedance and lack of an adhesive material (as found in wet Ag/AgCl electrodes) to fix the location of the electrode [83]. Increased contact area will reduce the skin electrode impedance [89], hence the use of multiple copper plates to make up electrode (E1 to E4).

The resistance measured using dry electrodes (R_{dry}) from seven subjects (14 knees), plotted against that measured using wet electrodes (R_{wet}) is shown on Figure 11(d), along with the linear regression line and the 95% confidence interval for the regression. The r^2 score for the regression was 0.8. The corresponding plot for the reactance (X_{dry} versus X_{wet}) is shown in Figure 11(e). The r^2 score for the corresponding regression was 0.9. These results indicate that the variations in the EBI measurements by

wet electrodes can also reliably be measured using the dry versions within the designed knee brace.

The resistance measurements obtained using wet electrodes are larger than that obtained using dry electrodes. A similar argument is true for the measured negative reactance. This can be attributed to the phenomenon of current constriction [90]. The wet gel electrodes used have an electrode surface area of 12.3 cm^2 (4.1 cm by 3.0 cm), while the dry electrodes have a total surface area of 61.5 cm^2 (five copper plates), which is 5 times larger than that of the wet electrodes. The smaller surface area of the wet electrodes constricts the path the injected current takes, causing a higher resistance to be measured compared to the resistance measured using the larger dry electrodes. A similar argument can be made for the measured reactance. The absolute difference in measurements between the dry and the wet electrodes can be compensated for by using a mapping between the wet and dry electrode measurements as shown in Figure 11 (d) and (e).

4.4 Conclusion and Future Work

An EBI measurement system architecture, intended for knee joint health monitoring was presented and validated previously. A position detection algorithm and the usability of the system using dry copper electrodes were presented in this chapter as a step towards reducing user guidance and making the system more feasible for a wearable setting. The principles presented in the context of wearable knee joint health monitoring using EBI, can be used to develop a fully wearable “smart knee brace” intended for clinical or home use. This would be the first ever system that can quantify knee edema outside of clinical settings with wearable technology.

Future efforts to develop a wearable system will focus on (a) hardware miniaturization and integration into a knee brace and including textile electrodes rather than copper ones; (b) applying this technology to other joints such as the shoulder; (c) developing a system sufficiently robust for unilateral rather than bilateral use (i.e.,

without the need for comparing the left to right knee); (d) the integration of a temperature sensor to the system, to gate EBI signals, so that measurements are taken with consistent knee temperatures; (e) exploration of the dynamic EBI signals in terms of knee joint injury and recovery.

CHAPTER 5: NOVEL METHODS FOR SENSING ACOUSTICAL EMISSIONS FROM THE KNEE FOR WEARABLE JOINT HEALTH ASSESMENT

5.1 Introduction

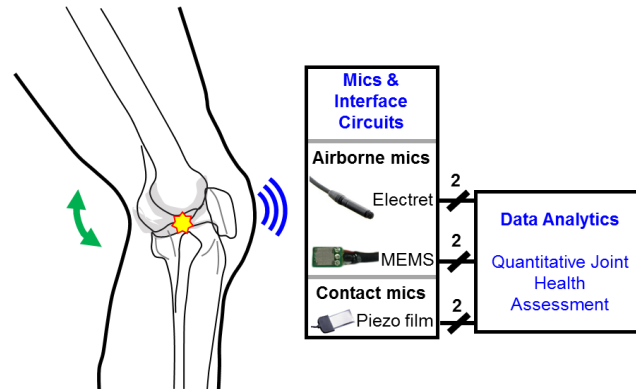


Figure 12: Block diagram of knee joint acoustic emissions sensing and interpretation for quantifying joint health during rehabilitation.

Using multiple sensing modalities in physiological sensing systems has significant advantages over using a single sensing modality [91]. Different sensing modalities are sensitive to different aspects of the underlying physiology. In the context of knee joint physiology, EBI measurements can provide information related to tissue swelling cell and wall integrity. The addition of another sensing modality along with EBI measurements can provide more accurate characterization of knee joint health via multi-sensor fusion [92].

Acoustics can potentially provide an additional non-invasive method for acquiring information about the underlying structures of the knee joint. The ability to monitor joint acoustics can enable the discovery of signatures that elicit specific signatures indicative of improving or worsening joint health. Furthermore, the capability of sensing joint acoustics in a wearable setting can enable around-the-clock monitoring of the knee joint, during normal activities of daily living, and prescribed rehabilitation activities. Towards

this goal, miniature sensors that can be readily integrated into a wearable device will be explored in this chapter. This will enable for the first time, wearable acoustics sensing from the knee (Figure 12). Furthermore, by acquiring inertial measurements from the knee along with joint sounds, the relationship between the sounds and the knee angle will be explored quantitatively. The work presented in this chapter was published in [93]

5.2 System Design and Methods

5.2.1 Microphone Selection

When selecting the types of microphones to include in the joint sound acoustic sensing system, the ability of the microphone to sense acoustical emissions along with its practicality for integration within a wearable system was considered. Analysis of how joint sounds propagate through the tissue and transmit to the air suggest contact microphones are the most appropriate sensor for acquiring joint sounds, and a review of prior art [18] shows that most researchers employ contact microphones successfully in *clinical / lab* applications. Contact microphones should theoretically acquire the highest quality acoustic signal since it senses the original, non-attenuated signal and is not sensitive to background noise. However, during motion and unsupervised *at-home* activity, loss of the sensor-to-skin interface is likely and of significant concern, for any compromise to the interface will be detrimental to the signal. In the extreme case that the sensor loses contact with the skin, the system will be unable to record joint sounds completely. To improve robustness, air microphones provide complementary sensing capabilities. The signal obtained by the air microphones will be inherently different from the contact microphones; the air microphones will only detect the airborne sounds: attenuated, higher frequency signals. Additionally, while not limited by the sensor-to-skin interface like contact microphones, air microphones are much more susceptible to background noise. For these reasons, both sensing modalities—contact and air

microphones—were employed, to more robustly capture the acoustical emissions from the joint in future implementation in a wearable device.

For the contact microphone, we selected a piezoelectric film (SDT, Measurement Specialties, Hampton, VA) because its form factor seemingly lends itself to a wrap and other devices conventionally worn on the knee. Furthermore, piezoelectric films have wider bandwidths compared to miniature, low cost accelerometers, allowing for sensing of high frequency audio signals.

Two types of air microphones were chosen to supplement the piezoelectric film in acquiring acoustical emissions from the knee joint. The first was a commercially available electret microphone (Sanken Microphone Co., Ltd., Japan). The second was a microelectromechanical systems (MEMS) microphone, specifically the MP33AB01 (STMicroelectronics, Geneva, Switzerland), which was mounted on a custom printed circuit board (PCB). Electret and MEMS microphones sense sounds in a similar manner; however, the commercial electret microphone is much more expensive (~x100) compared to the MEMS microphone. The MEMS's low-cost and sensing capabilities provide a realistic solution for implementation in a wearable device; however, both the electret and MEMS microphones were used during experimentation, with the electret microphone acting as the industry standard in terms of the quality of the sound acquired. This work focuses on the recordings from the air microphones because, at this time, they provide higher quality recordings as discussed in Section 5.3.1.

5.2.2 Methods for Microphone Comparison

The similarity of the MEMS and electret microphones in detecting knee joint acoustical emissions was quantified by computing the information radius between the normalized histograms of these signals, which were acquired by both sensors at the same time placed in the same location on the lateral side of the patella. To construct the aforementioned histograms, the signals acquired from the microphones were first normalized such that

their amplitudes were limited to the range $[0, 1]$. The histogram was formed from this normalized signal using 1000 bins.

Next, the quality of each sensor was evaluated by computing the signal-to-noise-and-interference ratio (SNIR). The SNIR for each microphone was calculated by finding the ratio of the peak power of a “click” (i.e., acoustical emission) emitted by the knee joint to the peak power of interface noise in the vicinity of the click. For this calculation, acoustical emissions from the microphones positioned at the medial side of the patella for the air microphones and distal side of the patella for the contact microphone were used.

Lastly, a proof-of-concept experiment was conducted to compare signals measured on and off of the skin. A subject performed three cycles of seated, unloaded knee flexion/extension with two electret microphones positioned at the lateral side of the patella, one on the skin and one located 5 cm off the skin. The resulting signals were then compared.

5.2.3 Interfacing Circuits

The analog front-end for the MEMS microphones consists of a non-inverting amplifier stage with 33 dB gain, which was selected such that the signals do not saturate but are amplified to utilize the full dynamic range of the subsequent analog to digital converter, and a high-pass 15 Hz cutoff frequency. This stage is followed by a second-order low-pass filter with a cutoff frequency of 21 kHz. A bandwidth of 15 Hz – 21 kHz was chosen, as knee joint sounds can range between these frequencies [44].

The analog front-end for the piezoelectric film microphones consists of an amplification stage of gain 45 dB and 100 Hz high-pass cut off. This stage is followed by a fourth-order low pass filter with a 10 kHz cut-off frequency. A 100 Hz high-pass cut off was chosen attenuate the interface and motion artifact noise.

5.2.4 Human Subject Study and Measurement Protocol

Thirteen male subjects without history of knee injuries participated in the study approved by the Georgia Institute of Technology Institutional Review Board (IRB) and the Army Human Research Protection Office (AHRPO) and gave written informed consent before participating. The subject population was reasonably homogenous in terms of physical activity level (collegiate athletes) and ranged in age (19 – 21 years), weight (84.1 – 135.3 kg), and height (174 – 195 cm). With this approach, the plan was to assess the variability in the measurements separately from variability due to age or knee joint health. Following preliminary measures of body composition, height, and weight, an electret and MEMS microphone were both positioned at the lateral and medial sides of the subject's patella targeting the patellofemoral joint while two piezoelectric film sensors were placed on the skin just proximal and distal to the patella. Each sensor was attached using Kinesio Tex tape. In addition to the tape, a thin piece of silicone (5 mm thick) was placed over the piezoelectric film to reduce the interface noise of the tape rubbing against the film. The skin was not prepped with alcohol or other debridement procedures to improve signal quality. Lastly, two wireless inertial measurement units (IMUs) (MTW-38A70G20, Xsens, Enschede, The Netherlands), which contained three-axis accelerometer, gyroscope, and magnetometer as well as built-in sensor fusion outputs, were positioned on the lateral sides of the thigh and shank. These sensor placements are displayed in Figure 13(a).

While wearing these sensors, each subject completed two exercises: (1) seated, unloaded knee flexion/extension and (2) sit-to-stand. For knee flexion/extension, each subject sat on a rigid seat adjusted to their height to prevent the foot from contacting the floor during motion. For the sit-to-stand exercise, each subject sat on a rigid seat with its height set such that the point 50% down the thigh aligned with the edge of the seat. While this procedure does not truly simulate a natural sit-to-stand technique, its use of an anatomical marker standardizes the measurement setup for both inter- and intra-subject purposes.

For each exercise, the subject repeated the motion five times while the microphone and IMU outputs were recorded in a quiet room. The signal acquisition setup is shown in Figure 13(b). The signals from the piezoelectric and MEMS microphones were passed through custom circuits and then collected at 50 kHz (16 bits/sample) using Biopac data acquisition hardware (Biopac Systems Inc, Goleta, CA) while the signals from the electret microphones were sampled at 44.1 kHz (16 bits/sample) using a Zoom H6 recorder (Zoom Corp., Tokyo, Japan). The IMU signals were acquired at 50 Hz (16 bits/sample) using their device-specific software suite (MT Manager, Xsens, Enschede, The Netherlands) synced with the Biopac system. Apart from the electret microphone signals, which were stored on an SD card (SanDisk, Milpitas, CA) via the Zoom recorder, all signals were recorded on a laptop. The data were then processed using Matlab (The Mathworks, Natick, MA).

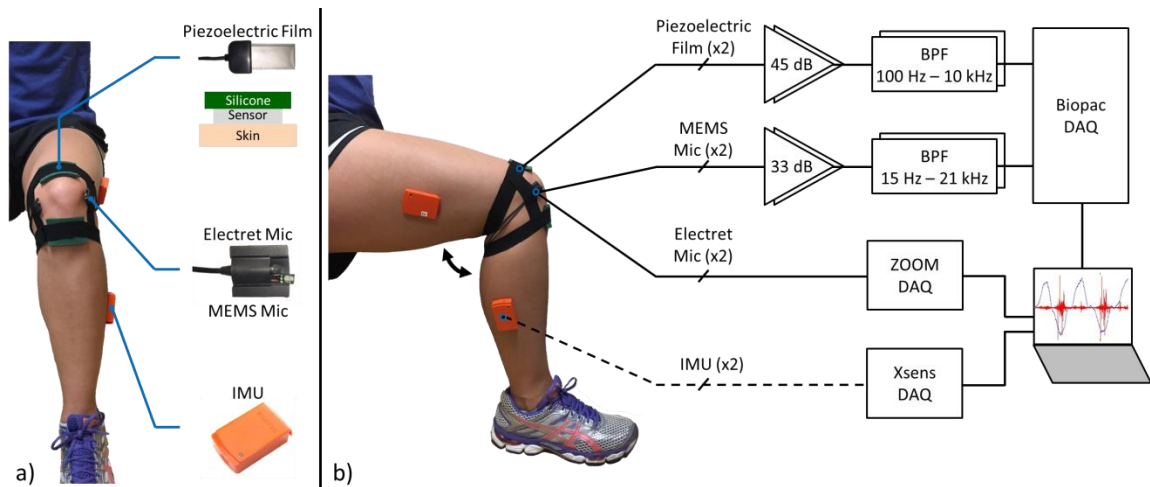


Figure 13: Sensor placement and measurement block diagram. (a) Eight sensors were used during human subject testing. Two IMUs were placed laterally on the thigh and shank. Piezoelectric film sensors were placed directly proximal and distal of the patella. The air microphones (MEMS and electret) were attached on the lateral and medial sides of the patella. (b) Block diagram of the data collection hardware used during human subject studies.

5.2.5 Joint Sound Processing

The signal processing consisted of (1) calculation of knee joint angle and contextualization of the joint sounds with joint angle, (2) identification of significant high

frequency acoustical emissions or clicks, and (3) statistical analysis to quantify the consistency of occurrence of the main clicks with respect to joint angle. Although all of the algorithms were performed as post-processing operations, the methodology was developed with the aim of enabling future real-time implementation in hardware.

First, the knee joint angle was calculated using the methods described in [94], which leverage the sensor fusion outputs of 3-axis accelerometer, gyroscope, and magnetometer provided by Xsens, namely the rotation matrix (i.e., Direction Cosine Matrix), and the kinematic constraints of a hinge joint to provide angle data. This method allowed for arbitrary sensor placement and orientation on each segment of the joint (i.e., thigh and shank), eliminating the need for precise calibration techniques and measures [94]. However, this method is potentially susceptible to error, due to deviations from a true hinge joint as a result of skin and motion artifacts [94]. Nevertheless, since we analyzed the cycles of repetitive motions against one another, this error was common to each cycle and thus did not present in our results; strict adherence to accurate absolute angle was not required. Finally, the signal was normalized between 0° and 90° such that subjects could be compared against one another with respect to location within each subject's range of motion.

Once knee joint angle was calculated, the “critical” points of the signal (flexion angle vs. time) were identified. These critical points were used to specify the beginning and ending of each cycle of an exercise (e.g., five sit-to-stand repetitions recognized). Additionally, these points were used to further classify the signal by the type of angular motion—either flexion or extension. To find these points, first the peaks of the signal were obtained. For each cycle, either one or two peaks were found. Because some subjects did not pause at the peak of the exercise (i.e., when fully extended), only one peak was found. These peak(s) identified the end of extension and beginning of flexion movements for each cycle. Next, the peaks representing the start of flexion and end of extension were paired, and between these peaks, the segment (1.1 ms) with the lowest

standard deviation of flexion angle was determined. This segment of relatively-constant (i.e., low standard deviation) flexion angle occurred during the pause between cycles, which was well-defined for each subject. Next, the signal between the peaks was flipped over the mean of this specified segment (with the smallest standard deviation), and the two points where the original and flipped signals intersected defined the end of flexion and beginning of extension. The joint angle calculation and segmentation was performed by Caitlin Teague from Inan Research Lab, Georgia Institute of Technology.

Next, significant acoustical emissions were identified. The most distinct audio signals that were detected by the air microphones were the high amplitude, short duration clicks. Figure 15 (a) provides an example 60 ms signal acquired from an electret microphone that clearly shows these broadband signatures. Observing the signal's frequency content (i.e. short-time Fourier transform, STFT), these clicks were seen to be broadband with frequencies as high as 20 kHz. This unprocessed signal contains two main sources of noise; ambient noise ranges in frequency up to 7 kHz while interface noise appears as baseline movement with components up to 1 kHz.

The block diagram of the significant acoustical emission identification algorithm is shown on Figure 14(a). The first step of this identification stage is outlier rejection such that any loud “clicks” that are not from the knee joint are eliminated from the signal. For this, the portions of the signal that were 10 standard deviations above the signal mean were replaced by the signal mean.

Next the signal was put through a filter bank consisting of 5 band-pass filters, the outputs of which were $x_{FBk}[n]$ ($k=1,2,3,4,5$). As seen from Figure 15 (a), the filtered signal ($x_{FBk}[n]$) lacks the original baseline movement, and the clicks are more distinct from other artifacts in the signal, compared to the original signal segment. The significant acoustical emissions within each of the signals $x_{FBk}[n]$, were identified using a “click detection” algorithm as outlined in Figure 14(b). The detection of clicks within different frequency bands rather than the whole signal bandwidth enabled the identification of

clicks that are prominent only within certain frequency bands. Filtering before this identification stage also minimized interface noise which could lead to the detection of false clicks (not emitted by the knee joint).

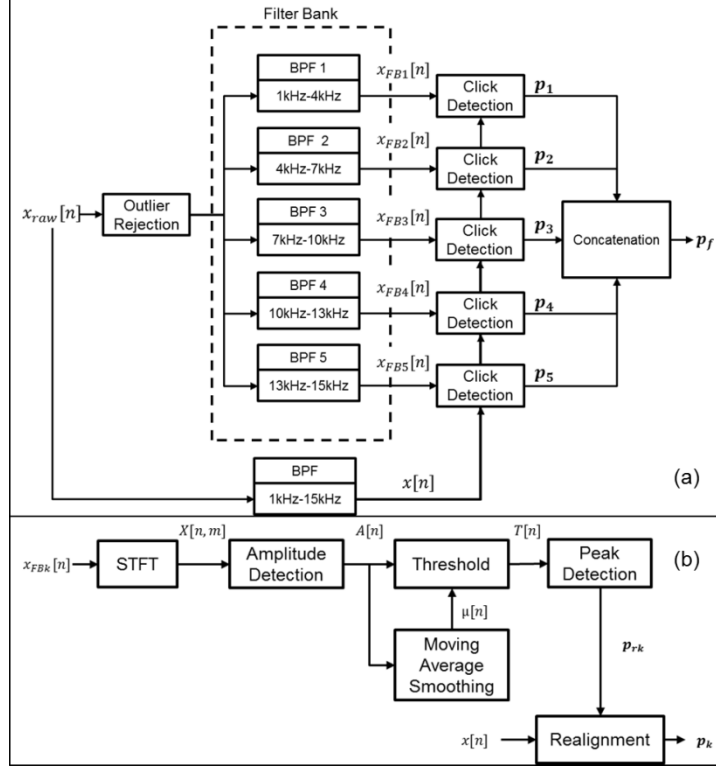


Figure 14: Significant acoustical emission identification algorithm (a) Block diagram of the whole algorithm. (b) Block diagram of the click detection portion of the algorithm.

For the click detection (block diagram shown in Figure 14(b)), a modified envelope detection algorithm was implemented. A 1024-bin spectrogram of the signal $x_{FBk}[n]$ ($X[n, m]$) was calculated with a window size of 5 ms and 90% overlap. The amplitude of the signal was calculated by summing the logarithmic amplitude of the spectrogram across the frequency bins as follows:

$$A[n] = \sum_j (20 \log |X[n, j]| + \delta) \quad (7)$$

where, $\delta = -\min_{n,m} 20 \log |X[n, m]|$ so that $A[n] > 0$. A moving average ($\mu[n]$) of $A[n]$

using a window size of 100 ms was calculated. $A[n]$ was then thresholded such that:

$$T[n] = \begin{cases} A[n], & A[n] > \alpha \cdot \mu[n] \\ 0, & \text{otherwise} \end{cases} \quad (8)$$

where $T[n]$ is the thresholded amplitude signal and α was the threshold, which was selected as 1.125 by inspection.

Next, the peaks of $T[n]$ were detected by standard peak detection techniques. The peaks that result from the same click (i.e. resonances of the initial click, which are specified as peaks within 8 ms of each other) and peaks with amplitude lower than the 50th percentile were eliminated, resulting in the raw click locations vector $\mathbf{p}_{rk} = [p_{rk1} \ p_{rk2} \ \dots \ p_{rkL}]$. An example of these detected clicks is shown in Figure 15 (a) along with the amplitude signal $A[n]$. The raw click locations \mathbf{p}_{rk} were realigned such that each click location corresponds to the point on the signal $x[n]$ (the original signal filtered with a band-pass filter, 1kHz-15kHz) where the click achieved its maximum absolute amplitude (the refined click locations vector is $\mathbf{p}_k = [p_{k1} \ p_{k2} \ \dots \ p_{kL}]$).

The click locations \mathbf{p}_k ($k=1,2,3,4,5$) were then concatenated, any repeated click locations were eliminated, resulting in the final click locations vector \mathbf{p}_f . An example of the detected clicks \mathbf{p}_f and the signal $x[n]$, along with the knee angle $\theta[n]$ is shown on Figure 15(b).

Once the clicks were identified, the consistency of these acoustical emissions was analyzed. Figure 15 (c) provides a visualization of consistent acoustical emissions during repetitive motion. For each cycle of a particular exercise (i.e., flexion or extension), the three clicks with the largest amplitudes and their corresponding angular locations were determined. Each permutation of the clicks across cycles (i.e., selection of one of the three clicks from each cycle) was found. The permutation with the smallest standard deviation for angular location yielded the most consistently occurring major acoustic event. The mean and standard deviation of these locations were calculated.

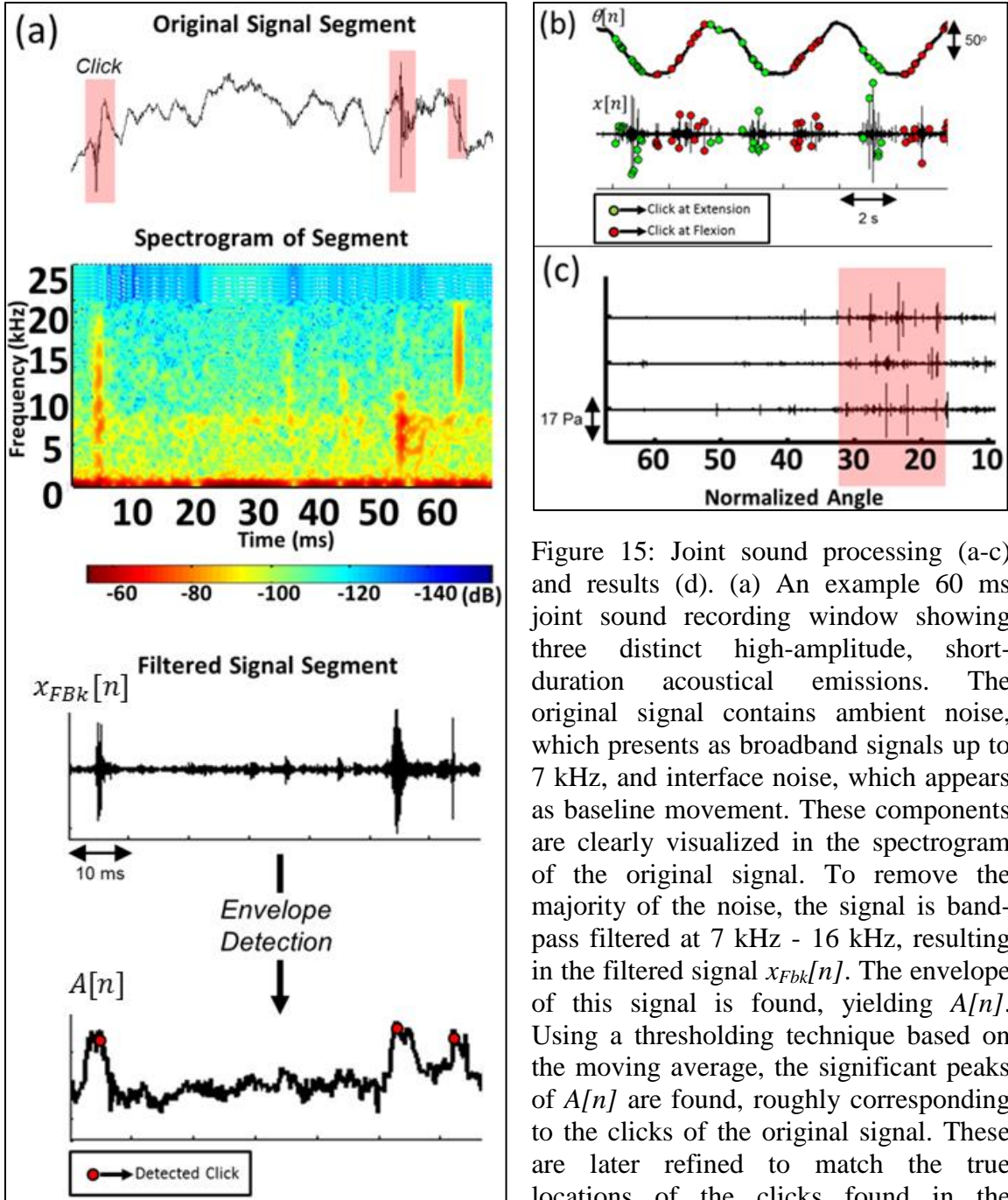


Figure 15: Joint sound processing (a-c) and results (d). (a) An example 60 ms joint sound recording window showing three distinct high-amplitude, short-duration acoustical emissions. The original signal contains ambient noise, which presents as broadband signals up to 7 kHz, and interface noise, which appears as baseline movement. These components are clearly visualized in the spectrogram of the original signal. To remove the majority of the noise, the signal is band-pass filtered at 7 kHz - 16 kHz, resulting in the filtered signal $x_{FBk}[n]$. The envelope of this signal is found, yielding $A[n]$. Using a thresholding technique based on the moving average, the significant peaks of $A[n]$ are found, roughly corresponding to the clicks of the original signal. These are later refined to match the true locations of the clicks found in the original signal (i.e., such that the locations correspond to where the clicks achieve their maximum amplitudes, positive or negative, in the original signal). (b) Final result of the click detection algorithm, which displays the identified clicks for three cycles of flexion/extension. (c) Three extension cycles with artificial offsets. These qualitatively show that the main acoustic event of each cycle occurs at similar angular locations.

Given these mean locations, three methods were used to analyze the data. For the first two methods, test-retest reliability was estimated using the intraclass correlation

coefficient (ICC). We organized the data into “subjects” and “raters.” There were 52 “subjects,” one for each human subject and exercise combination (e.g., subject 1’s extension data represented one “subject”). The “raters” consisted of the five click locations (one per cycle) from the selected permutation. This dataset will be referred to as the test-retest dataset. Given this dataset, two ICC values were calculated using one-way random single (i.e., ICC(1, 1)) and average measure (i.e., ICC(1, k)) models to show the reliability of a single cycles’ measure and mean of the fives cycles’ measures. Additionally, the 95% confidence intervals (CI) for these two ICC values were determined. The last method for analyzing the data was a paired t-test, which was used to assess whether there were significant differences between the mean click locations for left and right legs. The joint angle calculation and segmentation was performed by Caitlin Teague from Inan Research Lab, Georgia Institute of Technology.

5.3 Results and Discussion

5.3.1 Microphone Comparison

In evaluating the microphones, many different parameters were considered. First, the similarity of the signals measured by the electret and MEMS microphones were compared. The quality of these microphones was also determined by evaluating the quality of their sensing capabilities in terms of SNIR. Moreover, when investigating the interface issues for the air microphones, the effect that proximity of the sensor to knee had on the signal acquired was examined. Finally, we researched the quality of the contact microphone.

As shown in Figure 16 (a) and (b), the electret and MEMS microphones, measuring frequencies as high as 20 kHz, performed similarly in detecting joint sounds, which were acquired from a subject performing flexion/extension and sit-to-stand exercises respectively. This was confirmed by computing the information radius between

the normalized histograms of signals captured by these two microphones, which yielded a value of 0.0025. This value shows a high similarity between these two types of microphones since the information radius ranges from 0 for identical distributions to 2 for maximally different distributions [95]. This shows that the more cost-effective MEMS microphones are a viable substitute for the more expensive electret microphones. This is an important result when designing deployable systems.

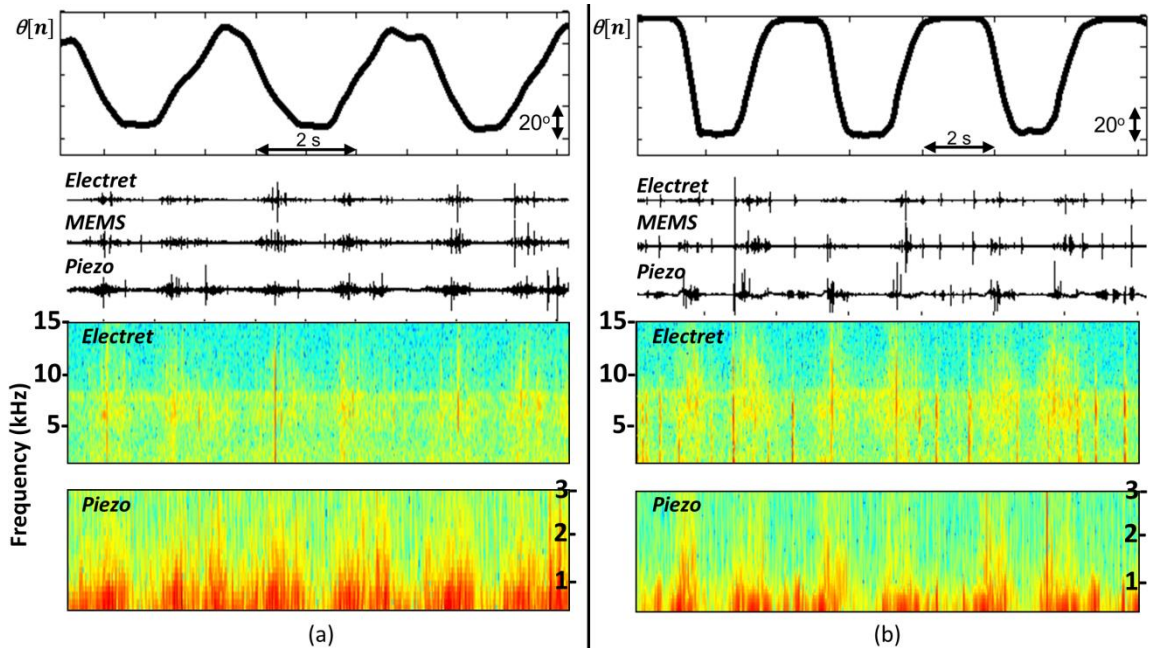


Figure 16: Joint sounds simultaneously sensed by electret, MEMS, and piezoelectric film microphones during three repetitions of (a) flexion/extension and (b) sit-to-stand exercises. For both parts (a) and (b), the top plot displays the joint angle ($\theta[n]$). The middle and bottom graphs show the time and frequency domain signals from the various microphones. (The acoustic signatures of the electret and MEMS microphones exhibit similar characteristics.)

As predicted, the signal recorded by the air microphones included noise and interface components in addition to the desired joint sounds; both ambient background interference and interface noise caused by the rubbing of athletic tape, which was used to hold the sensors in place, were sensed by the microphones. The SNIR was 11.7 dB for the electret microphone and 12.4 dB for the MEMS microphone. To minimize issues with noise during initial experiments, measurements were taken in a quiet room; however, this

will need to be addressed for implementation of a deployable, wearable system, especially given the fact that many ambulant sounds, such as speech, will reside in-band with the joint sounds.

One important observation made during proof-of-concept experiments showed that the air microphones did not need to be directly located at the skin surface to detect airborne joint sounds. As shown in Figure 16, the sounds obtained from an electret microphone placed on the skin and one located 5 cm off the skin captured similar acoustic signals in both morphology and timing (~4.5x smaller amplitude). This is an important observation because it suggests that the air microphones will be able to record joint sounds in a wearable device where direct contact with the skin may not be constant. However, it will be important to consider this distance when analyzing the captured signals, particularly when the analysis depends on the amplitude of the signal. In this sense, maintaining a fixed distance between the microphone and skin, especially for use in longitudinal analysis, will be required. Furthermore, placing the microphone off of the skin introduces increased potential for noise; the microphone may have a greater opportunity to strike or rub against the skin. These issues must be addressed in the design of a wearable system.

The piezoelectric film measured signals up to approximately 3 kHz as seen from the spectrograms of the signals acquired shown in Figure 16. While the piezoelectric film had the advantage of not detecting background noise, it acquired significantly more interface noise—8.4 dB SNIR—due to the sensor rubbing on the skin and the athletic tape rubbing on both the skin and the sensor. This interface noise had frequency components up to 1.5 kHz, and was thus in-band.

During early pilot data collections, the piezoelectric film was attached to the skin using only Kinesio Tex tape. However, this method proved to be very susceptible to interface noise; as the knee extends and flexes, the tape, though stretchable, deformed the film which obscured the low frequency and low amplitude signatures. Furthermore,

though acceptable for collecting pilot data, tape proves to be undesirable for long-term monitoring. To mitigate this issue, a piece of silicone was placed above the piezoelectric film. Because silicone has similar compliant mechanical properties to skin and subcutaneous tissue, the joint sounds received did not experience dampening, and the silicone surface provided a suitable surface to stick the tape. Though this method did not completely eliminate interface noise—the sensor still experienced some movement along the skin—it did help to reduce the recorded noise.

Accordingly, while using piezoelectric film or other contact microphones is desired to capture the vibration signal, which represents the majority of the acoustical energy generated, implementation presents practical issues. The piezoelectric film was significantly affected by interface noise; a smaller portion of the signal bandwidth was corrupted by interface noise for the air microphones compared to contact microphones. Furthermore, contact microphones did not pick up higher frequency vibrations as distinctly as air microphones. For these reasons, air microphone signals were used in this work to explore knee joint acoustical emissions. However, in future studies and in a future wearable device, both air and contact microphone signals can be used by employing multi-sensor fusion techniques.

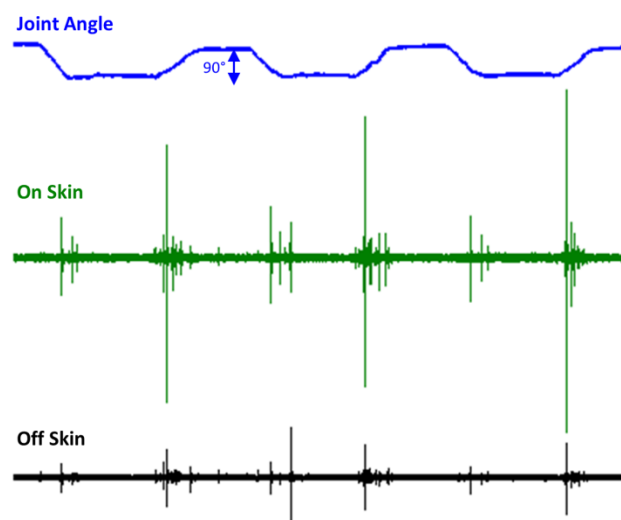


Figure 17: Joint sounds measured on the skin and 5 cm off the skin during flexion/extension exercises. Though the off-skin microphone captured a signal with

decreased amplitude, the on- and off-skin measurements showed significant similarities in their acoustic signatures. The main acoustic event of each signal occurred at similar locations.

5.3.2 Joint Sound Consistency

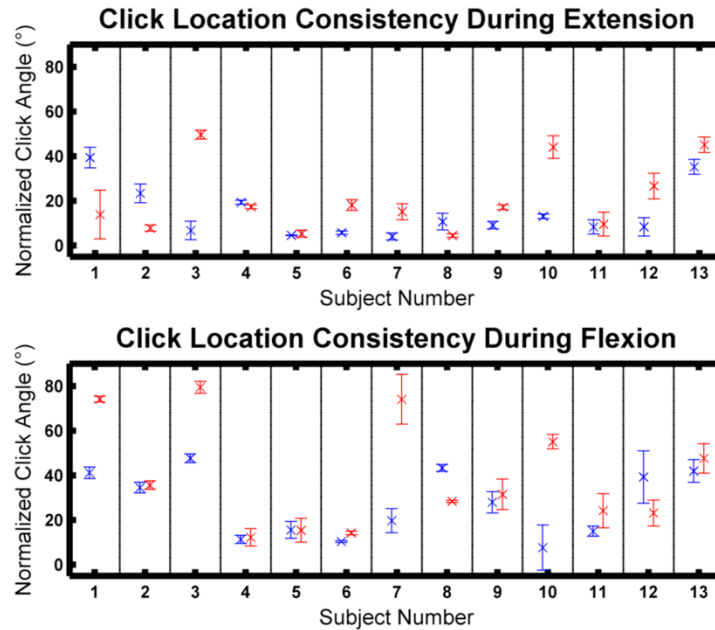


Figure 18: The final results of click location consistency for five repetitions of flexion/extension for 13 subjects on left (blue) and right (red) legs. Across subjects, the standard deviation for click location is small, supporting observations of consistent angular location cycle-to-cycle. Additionally, the mean locations of these clicks are consistent between left and right legs for most of the subjects.

Figure 18 summarizes the results for mean angular click location for the left and right legs of 13 seated subjects performing five repetitions of knee flexion/extension. Two important findings resulted from this data: (1) significant acoustic events are repeatable during single trial measures and (2) left and right legs produce similar sounds.

First, two ICC values were found for the test-retest dataset. An ICC(1,1) value of 0.94 with a 95% CI of 0.92-0.97 and an ICC(1, k) value of 0.99 with a 95% CI of 0.98-0.99 were calculated. Since the ICC values were greater than 0.7, these values showed that the main acoustical emission per cycle of activity were consistent within a single trial of monitoring for both single and average measure reliability [96]. Given that audible joint sounds have not been extensively explored, this was an important finding,

demonstrating that airborne signals emit a stable pattern with repeated movement in a healthy hinge joint.

Second, the difference between legs for each exercise suggested that a healthy subject's knees produce similar joint sounds; the difference between left and right legs were not significant at the $p < 0.05$ level. While as a group, there were no significant differences between the left and right legs, some subjects could be grouped as having relatively no difference between right limb and left limb click locations whereas others had notable differences between right and left suggesting the potential for defining clinically relevant "signature traits". Such variations in click location could represent useful knee joint health biomarkers.

Though these results are promising, there are some limitations to our current system and analysis. First, with regard to the IMUs, sensor positioning, drift, and motion artifacts can all contribute to flexion angle calculations that differ from the true joint angle. Techniques will need to be employed to minimize these errors, especially when considering their application in a system which measures longitudinal data. For example, ensuring more rigid sensor positioning [94] and leveraging the joint's kinematic constraints directly into the calculation of joint angle to minimize the effect of drift [97, 98] would help minimize error. Second, future work will need to investigate the effect of lubrication (e.g., diminished boundary lubrication after an injury [99]) and differing structural components (e.g., damaged ligaments [100], etc.) on acoustical emissions. These variables may introduce "error" when calculating click location consistency for repeated cycles and measuring differences between legs. In this sense, these isolated, one-time measurements may not prove to be useful biomarkers. However, future studies may find them to be more important during longitudinal analysis. Future work is required to determine the efficacy of these observations as clinically relevant data.

These quantitative findings in terms of measurement consistency will form the foundation for understanding the significance of changes in joint sound signatures

associated with injury, as well as changes in such signatures during rehabilitation. Moreover, while longitudinal studies will be important towards understanding injury recovery, this work and its focus on robust implementation in a wearable platform also presents opportunities for exploring day-to-day and within-day changes of joint acoustics.

5.4 Conclusion

This chapter describes the measurement and analysis of acoustical emissions from the knee joint during loaded and unloaded activities. A multi-modal, wearable sensing system is developed to acquire knee joint acoustical emissions. It is demonstrated, quantitatively, that major acoustic events, measured using the designed system, occur at consistent joint angles during repetitive motions for healthy subjects. Furthermore, it is observed that these locations are similar between left and right legs for most subjects (without any prior knee injuries). These findings showed that joint sound measurements from air microphones are repeatable, with sensing technology that can be implemented in an inexpensive, wearable form factor. While extensive analysis of the piezoelectric film was not conducted in this work due to corruption of the signal with interface noise, its use in a wearable device holds promise based on the preliminary findings showing that packaging techniques have a large influence on the signal recorded.

In the following chapter, audio feature extraction and data science techniques will be employed to calculate a metric related to knee joint health, from knee joint acoustical emissions. As the electret microphones presented are widely used in many commercial applications, the signals acquired by these microphones are used to derive the aforementioned metric.

CHAPTER 6: ACOUSTICAL EMISSION ANALYSIS BY UNSUPERVISED GRAPH MINING: A NOVEL BIOMARKER FOR KNEE HEALTH STATUS

6.1 Introduction

Over the past century, many researchers have employed large precision microphones and surface vibration sensors for in-clinic measurements of joint sounds to diagnose degenerative diseases from a snapshot measurement that was compared against a population norm [101-104]. While some promising results were obtained, a major challenge is the large inter-subject variability in joint acoustical emission signatures, and thus the relatively low specificity of such diagnostic approaches as compared to costly medical imaging. Moreover, a lack of mechanistic understanding of how specific structural changes in the knee can impact specific joint sound patterns has hindered progress in the field. Indeed, rather than focusing on diagnostics of specific sounds, the unveiled potential of joint sounds may be in the longitudinal assessment of the same person's knee health over time. It is anticipated that knee acoustical emissions may exhibit more complexity or erratic patterns following injury as compared to a healthy joint and will after corrective surgery and recovery.

In the previous chapter, a system for facilitating wearable joint acoustical emissions measurements outside of clinical settings was presented. The acoustical emissions from subjects with healthy knees only were examined, and the focus was on developing a robust interface between the sensor and the knee, to ensure that high quality measurements could be obtained. It was found that consistent and robust recordings could be obtained with inexpensive and miniature microphones placed on the knee.

This chapter examines joint acoustical emissions in the context of knee injury. It is hypothesized that joint acoustical emission heterogeneity will be more pronounced

after knee injury (compared to when healthy) and abate with corrective surgery and recovery. A novel unsupervised learning based algorithm for visualizing the acoustical emissions from the knee joints of the subjects, and for providing a quantitative output representing the heterogeneity of the measures is introduced. It is shown, for the first time that the heterogeneity of graphs constructed using knee sound data (quantified using the graph community factor, GCF) is higher for injured subjects than that for healthy subjects. Furthermore, it is shown that the heterogeneity decreases in injured subjects following corrective surgery and recovery.

6.2 Materials and Methods

6.2.1 Human Subject Protocol and Subject Demographics

Table 2: Demographic data for study participants (n=42 intercollegiate athletes). The lower extremity functional score (LEFS) was evaluated using the questionnaire presented in [105] on 80 point scale. *=Groups significantly different ($p < 0.01$), std.= standard deviation.

	Healthy	Injured
Number of Subjects	33	9
Injury Onset (range, in days)	N/A	2-22
# Females (% of group)	7 (21%)	1 (11%)
# Males (% of group)	26 (79%)	8 (89%)
Age (mean \pm std., in years)	19.8 \pm 0.9	20.8 \pm 1.6
Height (mean \pm std., in cm)	184.0 \pm 8.0	186.1 \pm 7.9
Weight (mean \pm std., in kg)	94.6 \pm 18.0	106.6 \pm 22.3
LEFS	78.8 \pm 2.5	36.3 \pm 10.5*

The protocol was an extension of the protocol presented in Section 5.2.4, in which knee joint sounds from thirteen male subjects with no recent knee injuries was acquired. Forty-two subjects participated in the study described in this chapter, which, was approved by the Georgia Institute of Technology Institutional Review Board (IRB) and the Army Human Research Protection Office (AHRPO). Thirty-three of these subjects had no recent injury (within the last six months) to any of their knees, and nine subjects had an acute, unilateral knee injury (the injury date was within a month of the study date). The

injuries included torn anterior cruciate ligament (six subjects), torn lateral meniscus (one subject) and sprained medial collateral ligament (two subjects).

For each subject, age, height and weight were recorded. Subject demographics and physical characteristics are presented in Table 2. Subjects were similar in age, height and weight between injured (n=9) and non-injured groups (n=33). A lower extremity functional scale questionnaire validated and utilized in clinical decision making (Binkley, et al.[105]) was completed at each laboratory visit. This self-reported score has a maximum value of 80 when no symptom limitations in daily function or activity are reported in the lower extremity. The questionnaire is made up of 20 questions related to the level of difficulty the subject has in doing various daily and sports activities (standing, sitting, running, squatting etc.). A significantly lower extremity functional score was reported by the injured subjects compared to the healthy subjects ($p < 0.01$ using a two sample t-test with unequal variances).

For each subject, air microphones, piezoelectric films and IMUs were placed around the subject's knees as described in Section 5.2.4 and as depicted in Figure 13 (a). The subject then performed five repetitions of unloaded knee extension and flexion while seated without foot contact with the ground. The signals from the microphones and IMUs were recorded as described in Section 5.2.4. The measurement procedure was repeated on both knees for all subjects (healthy and injured).

The aforementioned measurement protocol was repeated longitudinally for the subjects with knee injury who went through corrective surgery (seven subjects, torn ligament or meniscus) and across the recovery phase (4-8 months after injury date, 3-6 months after surgery date). The two injured subjects with medial collateral ligament sprains did not require corrective surgery, nor an extended period of rehabilitation; accordingly, a second recording was not available for these subjects.

Thus, a total of two recordings each were measured for seven of the nine subjects with acute injury (except for the two with sprains): once immediately following injury (within 22 days of the injury) and a second after surgery and 4-6 months of recovery (once the subject was able to resume functional activities). For the 33 healthy subjects, only one recording was obtained.

6.2.2 Signal Processing and Feature Extraction

The electret microphone on the medial side of the knee was used for signal processing and feature extraction. The other sensors (the electret microphone on the lateral side of the knee, the MEMS microphones, the piezoelectric films and the IMUs) were not used in this study. The sound signals recorded from a knee with an acute injury during knee extension and flexion cycles is shown in Figure 19 (a) as $x(t)$. The signal $x(t)$ contains high energy and short duration (order of magnitude of 10 ms) acoustic signatures that have a “spike-like” appearance in the plot of the signal. As seen from the spectrogram of the signal $x(t)$ in Figure 4(B), these joint sound signatures occupy broad frequency bands with frequency components as high as 20 kHz, but are mostly limited to frequencies lower than 15 kHz. The signal $x(t)$ also has frequency content below 1 kHz, most of which can be attributed to the microphone and Kinesio Tex tape rubbing on the subject’s skin (interface noise).

The signal processing and feature extraction workflow for the knee joint sound signals is illustrated in Figure 19 (b). The sound signals acquired during five extension and flexion cycles from the left knee of the subject are digitally filtered using a finite impulse response band-pass filter with a bandwidth of 1 kHz-15 kHz. The lower cutoff 1 kHz removes most of the interface noise in the signal, and the upper cutoff of 15 kHz limits the bandwidth of the signal to be analyzed while keeping most of the information from the high energy and short duration joint sound signatures.

Table 3: Description of the audio features extracted from each 200 ms signal frame. For detailed information on features f_1 - f_{35} , refer to [106]. Features marked with a (*) in the “Feature Number and Name” column are time domain feature; the rest are frequency domain features. ZCR=zero-crossing rate, MFCC = Mel-Frequency Cepstrum Coefficients.

Feature Number and Name	General Description	Significance in terms of knee joint sounds
f_1) Energy *	Total signal energy.	High in frames with knee joint sound signatures.
f_2) ZCR *	The rate of sign change.	High in frames with knee joint sound signatures.
f_3) Energy Entropy	Measures sudden signal energy changes.	Low in frames with joint sound signatures and lots of interface noise.
f_4) Spectral Centroid	The first moment of the signal spectrum.	High in frames dominated by joint sound signatures.
f_5) Spectral Spread	The second central moment of the signal spectrum.	High in frames with joint sound signatures.
f_6) Spectral Flux	A measure of the difference between the signal spectra of successive frames.	Lower in frames rich in joint sound signatures as the spectra of these signatures are more consistent than that of random background and interface noise.
f_7) Spectral Entropy	A measure of the “complexity” of the spectrum of the signal.	High in frames with lots of joint sound signatures as these frames have irregularly shaped spectra. Background and interface noise have flatter spectra.
f_8) Spectral Roll-off	The frequency below which 90% of the signal energy is concentrated.	High in frames with joint sound signatures.
f_9 - f_{21}) MFCC	A popular speech processing feature related to the signal cepstra [107].	Especially coefficients f_9 - f_{13} have discriminative capability in identifying frames that have joint sound signatures vs. background/interface noise.
f_{22} - f_{35}) Fundamental frequency, harmonic ratio and Chroma vector	Features widely used in music information retrieval [106].	These features are capable of indicating frames rich of joint sound signatures.
f_{36} - f_{64}) Band powers	Power of the signal in 29 distinct frequency bands, between 30 logarithmically spaced frequencies in the range of 1-15 kHz.	Higher frequency band powers obtain high values at frames rich of joint sound signatures while low frequency band powers are high in frames dominated by interface noise.

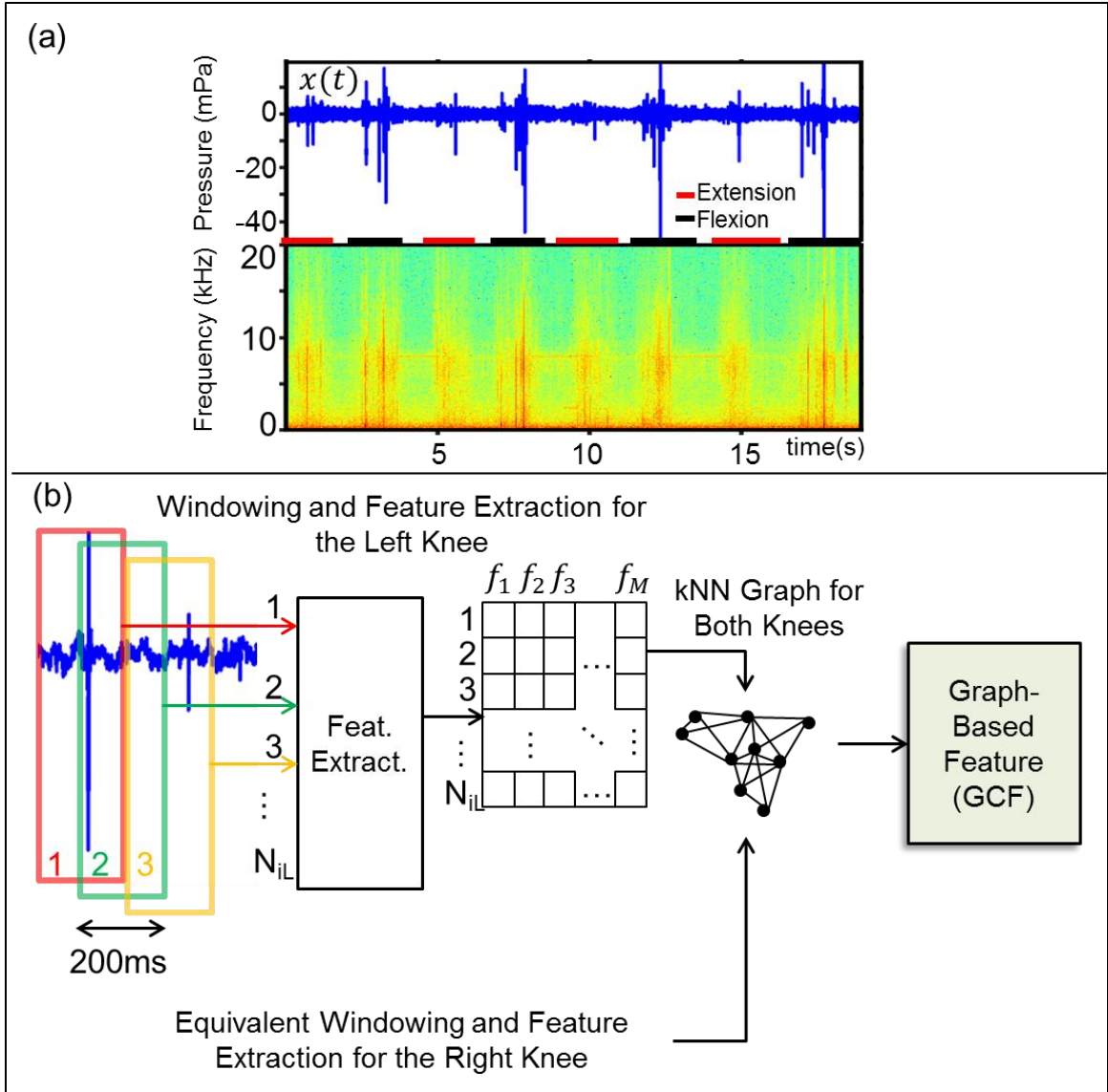


Figure 19: An overview of the methods by which the signals acquired from the knee joint are analyzed. (a) The knee joint sound signal ($x(t)$, in blue) and the spectrogram of $x(t)$, measured from the knee of a human subject during four leg extension and flexion cycles. (b) The signal analysis workflow for knee joint sounds. The signals from the left knee of the subject are filtered and standardized (to zero mean and unity variance) and windowed (frame length of 200 ms with 50% overlap). $M=64$ features (f_1, f_2, \dots, f_M) are extracted from each of the N_{iL} frames and stored in an $N_{iL} \times M$ matrix where each row represents a frame and each column represents a feature. The aforementioned steps are repeated for the right knee and the data matrices formed using both knees are concatenated. A k-nearest neighbor graph (kNN graph) is constructed from the matrix formed using data from both knees. The graph community factor (GCF) is calculated from the kNN graph.

The filtered signal is then standardized to have zero mean and unity variance to compensate for variations in the distance between the microphone and the skin. The standardized signal (shown in blue in Figure 19 (b)) is then windowed with a frame duration 200 ms and 50% overlap between frames, resulting in N_{iL} signal frames from the left knee (L) of the i^{th} subject. The frame duration was chosen heuristically to allow for multiple joint sound signatures to be present within a given frame. A total of $M=64$ features are extracted from each frame and placed in an $N_{iL} \times M$ matrix where each column represents a feature and each row represents a frame. The features extracted from each frame are summarized in Table 3 (refer to [106] for more detail on features $f_1 - f_{35}$). The aforementioned steps are repeated for the right knee of the i^{th} subject as well, resulting in another $N_{iR} \times M$ data matrix. The matrices formed using both knees are concatenated to form a final $(N_{iL} + N_{iR}) \times M$ data matrix, \mathbf{X}_i for the i^{th} subject.

6.2.3 Graph Community Factor Calculation

The data matrix \mathbf{X}_i from each subject is used to construct a k -nearest neighbor (kNN) graph for each subject. The rows of \mathbf{X}_i are represented as vertices in the graph and connect each vertex to its k nearest neighboring vertices, using the Euclidean distance metric. Weights are then assigned to each graph edge using dice similarity [108]. Letting vertices v_p and v_q be two connected vertices within the graph, the weight for the edge between these vertices is defined as,

$$w_{pq} = \frac{2 * |\{A_p \cap B_q\}|}{(|D_p| + |D_q|)} \quad (9)$$

where A_p and B_q are the set of k -nearest neighbors of v_p and v_q respectively, D_p and D_q denote the degree of v_p and v_q and $|\cdot|$ indicates the number of elements in a set. Therefore, for a kNN graph, the dice similarity is the ratio of the number of neighbors that v_p and v_q have in common to k .

After the weighted graph is constructed, the potential communities within the graph are detected. The Infomap community detection algorithm is used for this purpose [109]. This algorithm considers the amount of time spent in different portions of the graph, by a random walking process, to reveal different communities within the graph [109, 110]. The computational complexity of this algorithm is $O(|E|)$, where E is the set of edges in the graph. The version of Infomap available in [16] is used in this work. Once the communities are detected, the GCF is calculated as the number of communities discovered.

It is expected that the data from both knees of a healthy subject would be more homogeneously distributed within the features space than the data from a subject with a unilateral knee injury. However, modeling the distribution of \mathbf{X}_i using models such as Gaussian or student's t-distribution[111] requires strong assumptions to be made about the shape of the data in the high-dimensional space (e.g. ellipsoid, convex). Furthermore, such models need parameters to be estimated about the underlying distribution of the data, which is difficult in high dimensions due to the curse of dimensionality [112, 113] (in high dimensional space where all data points appear to be sparse, it becomes increasingly difficult to understand the properties of the data). Kernel-density estimation based clustering techniques suffer from the same problem due to the existence of parameters to be estimated, such as kernel bandwidth.

Rather than modelling the distribution of the data in the high-dimensional feature space, a kNN graph is used, which has been used in previous studies to model and cluster high dimensional data in bioinformatics[114, 115]. The heterogeneity of the data distribution is quantified using the number of communities within the graph, which is expected to be higher for data that is more heterogeneously distributed.

Communities are detected within the data graph instead of finding clusters within the data using regular clustering algorithms such as k -means, Gaussian mixture models, or spectral clustering, as such algorithms take the number of clusters to be found as an

input. Using a kernel density estimate based clustering algorithms [116] to estimate the number of clusters in the data is not a feasible solution either. Such techniques are very time consuming for high-dimensional data, and the curse of dimensionality makes it difficult to robustly detect dense areas within the data distribution.

Another critical aspect of the proposed method is the use of dice similarity as graph edge weights. A kNN graph with $k=3$ that contains three predefined communities represented in black, blue, and red respectively is shown in Figure 20. If a similarity metric based on the Euclidean distance between the vertices is used (such as the reciprocal of the Euclidean distance) as the edge weights, the blue and red communities, are merged during community detection, leading to two communities being detected instead of three. This happens because v_p and v_q are edges that are close to each other but belong to different communities and therefore the edge weight, w_{pq} , would be non-zero. The merging of distinct communities can be exacerbated by the existence of communities that are concavely shaped such as the red community. Using a metric derived from the Euclidean distance also makes the number of communities detected very sensitive to the parameter k . However, using the dice similarity for edge weights addresses these problems. The weight, w_{pq} , of the edge between the vertices v_p and v_q (shown in green) is zero when dice similarity is used, as these vertices have no common neighbors, thus making the dice similarity zero. Using dice similarity also makes the algorithm more robust to changes in the parameter k , making it more easily generalizable.

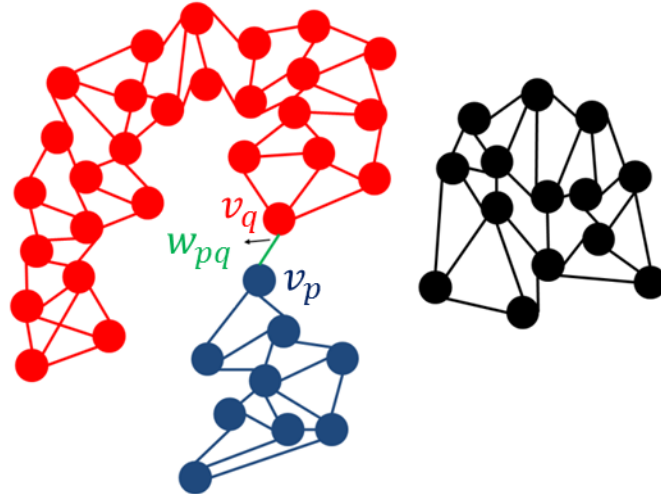


Figure 20: A representative k -nearest neighbor graph where $k=3$. The graph contains three underlying communities shown in red, blue, and black. The communities in red and blue cannot be distinctly detected using edge weights, derived from the Euclidean distance between the vertices, as the weight of the edge in green (w_{pq}) would be non-zero. Using dice similarity to calculate edge weights solves this problem, as this makes w_{pq} zero.

6.3 Results and Discussion

6.3.1 Results

The capability of the GCF metric in discriminating healthy from injured subjects by analyzing knee sounds gathered from forty-two college athlete human subjects, with and without recently acquired acute, unilateral knee injuries is demonstrated.

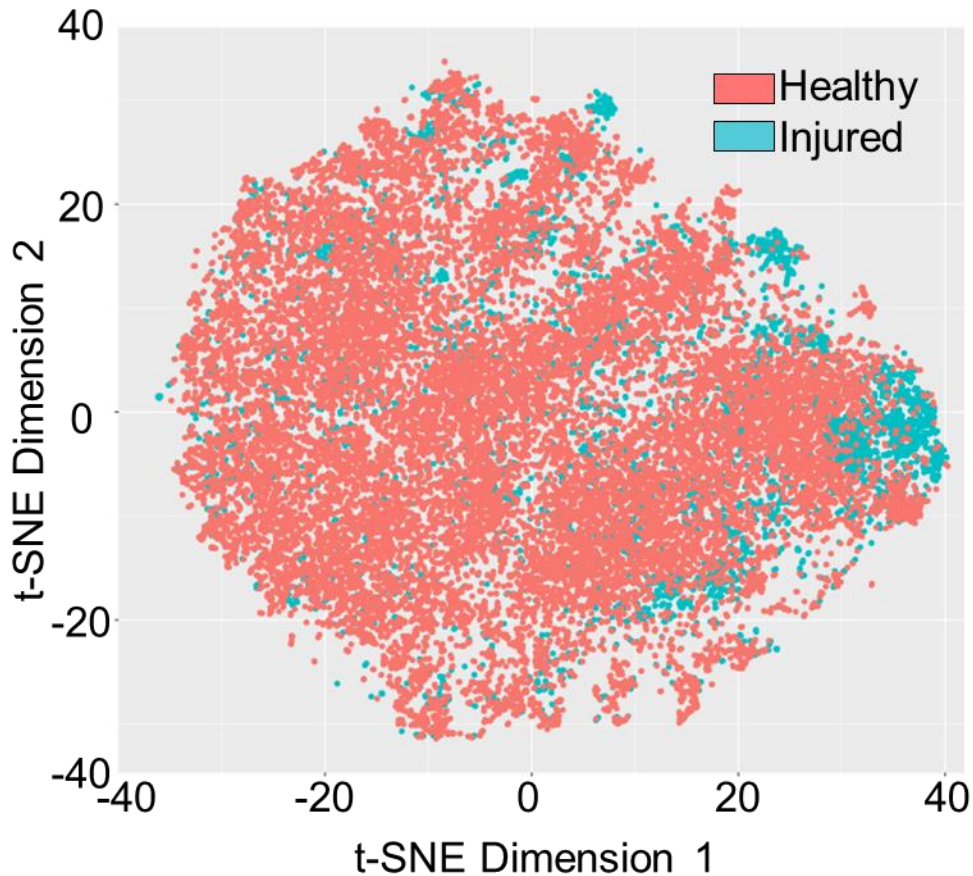


Figure 21: Visualization of the audio signal frames from nine subjects with acute unilateral knee injury (in cyan) and 33 healthy subjects (in pink), using t-Stochastic Neighbor Embedding (t-SNE). t-SNE computes a distance matrix corresponding to distances between every pair of frames. It converts this distance matrix to joint probabilities and minimizes the Kullback-Leibler divergence [117] between the joint probabilities of the 2D embedding space and the high-dimensional feature space. Note that the new calculated dimensions (e.g. t-SNE dimension 1 and t-SNE dimension 2) do not correspond to any specific acoustical features. These dimensions integrate the relations between the individual data points in the high dimensional space to represent them in a lower dimensional space.

The data from all forty-two human subjects are visualized in Figure 21 using t-Stochastic Neighbor Embedding (t-SNE) [118]. Each data point on this plot corresponds to a 200 ms window of an acoustic signal acquired from a subject’s knee joint. Each window is represented using 64 audio features and the dimensionality of the data is reduced to two using t-SNE. The two t-SNE dimensions do not necessarily have physical meanings. This visualization of the data shows that the frames from injured subjects (in

cyan) and healthy ones (in pink) cannot be separated using the extracted features. To overcome this challenge, an unsupervised graph mining approach is proposed in order to devise a metric that can distinguish injured subjects from healthy ones.

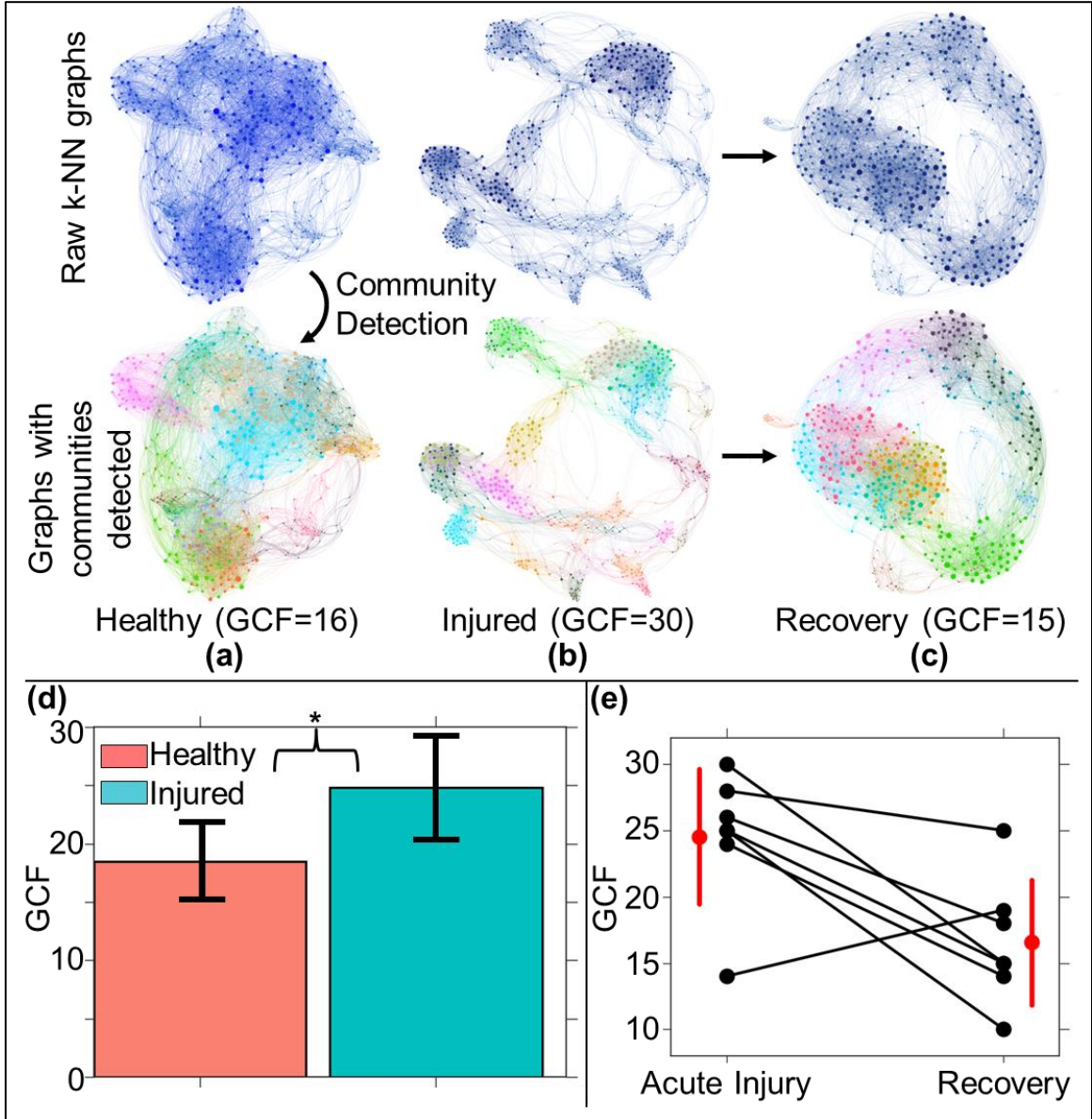


Figure 22: The relationship between graph heterogeneity (quantified using the graph community factor, GCF) and acute unilateral knee injury. (a) The graph constructed using features extracted from the audio signals acquired from both knees of a healthy subject (top). The Infomap community detection algorithm discovered 16 communities (GCF=16) in the graph, all shown in distinct colors on the graph in the bottom. (b) The graph constructed using the data acquired from a subject with an acute unilateral knee injury, where 30 communities are detected. The heterogeneity of the features for the injured subject is visually and quantitatively greater than for the healthy subject. (c) The

graph constructed using the data acquired from the injured subject shown in Figure 1(B), after corrective surgery, where the number of communities detected has decreased to 15, and the heterogeneity has decreased visually. (d) The GCF calculated for subjects with an acute unilateral knee injury (shown in cyan) and for healthy subjects (shown in pink). The bars represent the mean of the GCF within the population and the error bars represent one standard deviation. (*) represents a statistically significant difference ($p=0.01$), where the p-value is calculated using a paired t-test with unequal variances. (D) The GCF metric for seven subjects with unilateral knee injury before and after corrective surgery. The black data points connected with lines represent each subject. The red data points and error bars represent the mean and one standard deviation of the GCF, for all the seven subjects, before and after surgery.

The graph constructed using both knees of each subject provides a new method of visualizing acoustical emissions from the knee. Figure 22 (a) and (b) show the graphs constructed for a healthy and injured subject respectively. As described in the methods, each node in the graph represents the high dimensional vector of time and frequency domain features extracted from one windowed segment of the acoustical emission waveform. The different communities detected within these graphs are shown in different colors at the bottom. The number of communities detected within the healthy subject's data graph was 16 (GCF=16) while for the injured subject's graph it was 30. In addition, the GCF metric decreased to 15 for the same injured subject after corrective surgery and six months of recovery as shown in Figure 22 (c). Visually, the plots on the top of the figure are qualitatively in agreement with these quantitative findings. The graph on the upper left (healthy subject) shows a set of densely clustered, homogeneous nodes, with many of the nodes falling close to one another in the high dimensional space. The graph on the upper middle (subject with recently acquired acute injury), on the other hand, shows a more heterogeneous set of nodes, geometrically spread out in space rather than clustering together densely. Finally, the graph on the upper right (injured subject following surgery and recovery) demonstrates that the same subject's nodes become much more homogeneous following recovery, resembling closely those observed in the healthy subject's graph.

Figure 22 (d) compares the GCF metric of nine subjects with acute, unilateral knee injuries to that of 33 healthy subjects. While the GCF is derived from each subject's data independently, the metric can be compared among subjects in an absolute manner, with a lower GCF indicating more homogeneous acoustical emission signatures and a higher GCF more heterogeneous emissions. In the bar-plots shown in Figure 22 (d), the height of the bar represents the mean value of the GCF metric within the population (injured or healthy) while the error bars represent one standard deviation. The GCF metric was higher for subjects with an acute, unilateral knee injury than the healthy subjects, and the difference between the groups was statistically significant ($p=0.01$). A two sample t-test with unequal and unknown variances was performed to evaluate the statistical significance.

Figure 22 (e) presents the change in the GCF metric during injury recovery for seven subjects with unilateral knee injuries that were treated with corrective surgery. This figure depicts that the GCF metric decreased for six out of seven of these injured subjects. In the exceptional case, the GCF metric showed an ascending pattern. The overall results for all subjects were found to be significantly lower following surgery and recovery using a paired t-test ($p = 0.01$). The changes in GCF indicating improved knee health were consistent with the lower extremity functional scores obtained for all subjects as well. The lower extremity functional score for these subjects increased from 36.1 ± 12.1 in the first measurement to 63.7 ± 11.0 after surgery and recovery ($p < 0.01$ using a two sample t-test with unknown and unequal variances).

The proposed algorithm has a hyper-parameter, k , which is the number of neighbors each node in the kNN-graph is connected to, for each subject. Figure 23 shows the effect of varying the value of the parameter k (number of nearest neighbors for each vertex in the graph of a subject; see the section Graph Community Factor Calculation), on the ability of the GCF metric in discriminating healthy from injured subjects. It can be seen that the discriminating ability of the GCF metric is the best for $k=5$ in the set of

values considered, {5,10,15,20}. For all values of k except for 20, the differences between the injured and healthy groups were significant ($p < 0.05$). This shows that the discriminative ability of the GCF metric is robust to variations in the parameter k .

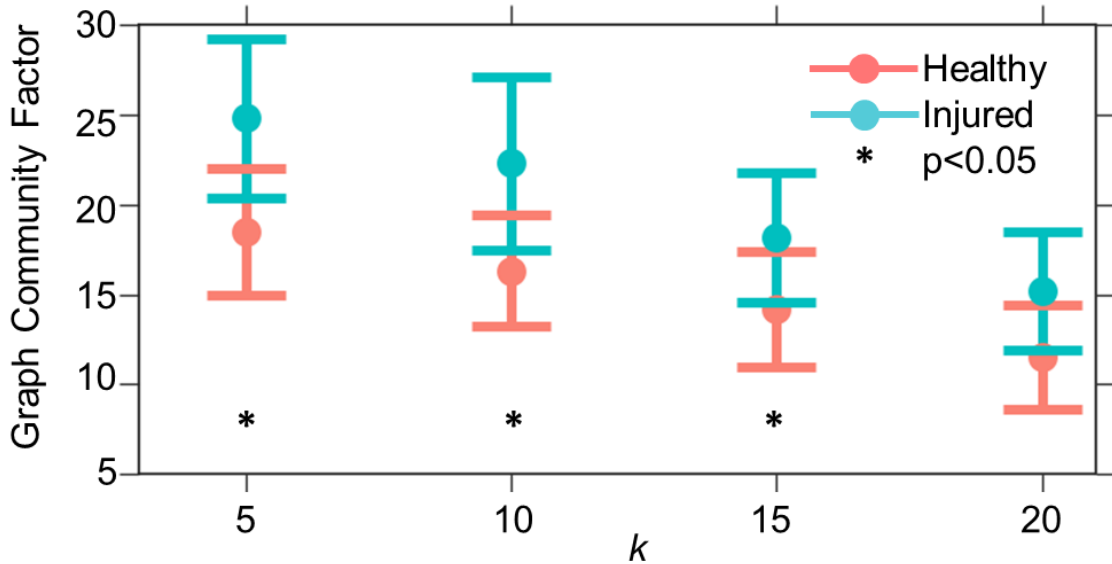


Figure 23: The effect of the parameter k , which is the number of neighbors each vertex is connected to in the constructed graph, on the ability of the graph community factor (GCF) metric in discriminating between subjects with an acute unilateral knee injury (in cyan) and healthy subjects (in pink). The values of k in the set {5,10,15,20}, are considered. All differences were found to be significant ($p < 0.05$) except for the case of $k = 20$, as denoted by the asterisks (*).

6.3.2 Discussion

This work represents, to the best of our knowledge, the first time that unsupervised graph mining algorithms have been applied to bioacoustical signals. These powerful algorithms designed for visualizing and quantifying similarities in high dimensional datasets have been used previously in genomics, single cell data analyses [114], and other such fields but have never been used to derive new knowledge from bioacoustical signals such as knee sounds. Compared to other physiological signals that have been studied extensively, namely signals of electrophysiological origin such as the electrocardiogram, knee acoustical emission waveforms do not have readily identifiable characteristic points or features and exhibit high inter-subject variability. Each person's knees vary in size,

shape, composition, and structure, and thus the sounds emitted during motion are, as expected, quite variable in nature. Accordingly, conventional feature extraction and classification algorithms based on identifying peaks, time intervals, frequency domain characteristics, or even combined time-frequency analyses (e.g., wavelet transform) cannot discriminate readily between healthy and injured joints in recordings taken from a population of subjects. Importantly, there is no existing knowledge of what knee acoustical emission features are associated with an injured versus healthy joint; thus supervised learning approaches are confined to black box models only, requiring very large datasets. Graph mining algorithms, on the other hand, are designed specifically to visualize and quantify the distribution of the data – even smaller datasets – in high dimensional spaces. In particular, the use of k-Nearest Neighbor (kNN) graphs for high dimensional data have been demonstrated to be more robust than other methods [119]. The presented unsupervised graph mining technique can be applied to other physiological signals as well, and presents a novel method of biomedical signal analysis.

The entire unsupervised learning algorithm used in this paper only requires a single parameter to be tuned – the value of k , which represents the number of neighbors connected to each vertex in the graph. Thus, the sensitivity of the results to the value of this parameter can readily be computed, as shown in Figure 23. The results were remarkably insensitive to the value of k that was chosen with statistically significant differences between the two populations manifesting for a wide range of values. Thus, it is anticipated that the approach defined in this work will generalize well to other datasets of joint acoustical emissions for healthy and injured knees.

In this study, the value of k was chosen to be 5, which was the value of k that minimized the p-value of a paired t-test performed to the GCF metrics of injured and healthy subjects, where k was chosen from the set {5,10,15,20}. In reality, when the GCF metric for a new subject is to be calculated, a certain value of k should be chosen beforehand. The choice of k in this case would be the one that minimizes the p-value of

the paired t-test performed to the GCF metrics of injured and healthy subjects, excluding the new subject. The reason for this is that, in a real life scenario, one might not know if the subject to be tested has a knee injury or not, hence the GCF metric for the subject is to be calculated to find this out. To present the ability of the GCF metric in distinguishing between healthy and injured subjects that better represents the scenario described, a p-value averaged over the folds of a leave-one subject out (LOSO) cross-validation scheme should be calculated. For this, first a subject is left out of the dataset, and the GCF metric is calculated for the remaining subjects using values of k chosen from a set (or a grid), such as $\{5,10,15,20\}$. The p-value of the GCF in distinguishing between the injured and healthy subjects would be noted for each value of k and the one that minimizes this p-value would be chosen. Then the GCF metric would be calculated for all the subjects including the one that was previously left-out, using the k value chosen and the p-value of the GCF metric, $p(i)$ (the p-value in the fold of the cross-validation where the i^{th} subject is left out) would be calculated using a paired t-test between the healthy and injured subjects. The process would be repeated, until each subject in the data set is left out exactly once, and the p-values, $p(i)$, calculated at each fold of the cross-validation would be averaged to obtain p_{avg} . The averaged p-value more closely mimics the ability of the GCF metric in distinguishing between a healthy and an injured subject in the real life scenario described, where the value of k is chosen prior to testing the new subject. In this study, we did not use cross-validation due to the limited number of injured subjects in our dataset.

The required memory for the implementation of the proposed method is a potential limitation of using the method in a wearable system. The space complexity of the proposed algorithm to store the knee graph (using an adjacency matrix) is $O(|V|^2)$, where V is the set of nodes in the graph. Hence, if the signal has too many windows, the size of the graph would increase in a quadratic fashion, making the method impossible to be implemented on a wearable system with limited memory. To overcome this limitation,

one simple solution can be the use of an adjacency list instead of an adjacency matrix to store the graph, since the space complexity of an adjacency list is $O(|E|+|V|)$ where $|E|$ and $|V|$ are the number of edges and vertices in the knee graph, respectively. The aforementioned complexity is more affordable in a wearable implementation of the system.

Another limitation is that only one microphone was used on the knee for each recording, positioned at the medial side of the patella. The electret microphone located at the lateral side of the knee, the MEMS microphones, piezoelectric films and the IMUs were not used for data processing. In future work, all the sensors could be used to extract more features from the knee joint acoustical emissions. Some new features can be derived based on the correlation of signals acquired simultaneously from different microphones. Also, the use of miniature microphone arrays positioned around the knee joint could provide more information about the knee joint by fusing the recordings from these arrays of microphones to better capture the overall acoustical emission patterns.

The scientific findings regarding joint sound complexity elucidated in this work by unsupervised knee graph mining can provide significant benefits in the future for patients rehabilitating knee injuries. The microphones and electronics used can be readily implemented in wearable systems, such as a knee brace worn by a user at home or austere environments. Such a wearable knee brace that can provide a biomarker relating to knee joint health can improve the quality of care by providing feedback to patients and physicians. Additionally, the feature extraction and unsupervised learning algorithms can be performed nearly in real-time, do not require computational complexity beyond what would be available on a smartphone or tablet device, and can potentially provide an output to the user indicative of joint health status – namely, the GCF metric. Thus, a user could wear a brace with embedded microphones and electronics that could send the acoustical waveforms captured from these sensors wirelessly to a smartphone or tablet for the GCF metric to be computed. Future studies with more granular data recordings during

rehabilitation can allow particular GCF scores to be mapped to rehabilitation progress, such that users can then potentially modify the rehabilitation protocol based on the GCF score. This could lead to more effective rehabilitation for patients at home with therapies being tuned in real-time according to their changing knee health status.

6.4 Conclusion and Future Work

An unsupervised graph mining algorithm is introduced in this chapter, in order to analyze knee joint acoustical emissions. In this method, audio features are extracted from acoustical emissions acquired from the knee joint and the data from both knees are used to construct a kNN graph. The constructed graph is found to be more heterogeneous for subjects with unilateral knee injuries compared to subjects with healthy knees. The heterogeneity of the constructed graph is quantified using the GCF, which represents the number of potential communities in a graph. The GCF is found to be higher in subjects with unilateral knee injury compared to healthy subjects, presenting a potential biomarker for knee joint health. Furthermore, the proposed algorithm has a single hyper-parameter k , which is the number of neighbors each vertex connects to in the kNN graph and the results are found to be robust to changes in k . The algorithm provided presents a novel way of processing physiological signals that can be applied to other biomedical signals as well.

Future work should involve the use of an array of microphones for acquiring knee joint acoustical emissions, consisting of both air and contact microphones. Feature extraction techniques which fuse the information obtained from all the microphones should be developed.

Furthermore, state of the art techniques such as deep learning can be used to devise new, more abstract but more effective audio features that are related to knee joint health in future work. Time-frequency analysis techniques such as spectrograms or wavelet scalograms could be used to construct images from the knee joint acoustical

emissions. These images could be used to find patterns related to knee joint health within the acoustical signals using convolutional neural networks. Convolutional neural networks can also be used directly on the time domain acoustical signals, to extract patterns relating to knee joint health in the time domain. The new features extracted via deep learning can then be used to construct kNN-graphs and compute the GCF, which can potentially provide a better biomarker than the one presented which uses simple audio features.

CHAPTER 7: CONCLUSION AND FUTURE DIRECTIONS

7.1 Conclusion

This work presents systems and algorithms that can be used to monitor knee health using wearable technology and validates the methods presented using human subject studies. The ultimate vision of the work is to have a “smart knee brace”, which is a knee brace with embedded, miniature, multi-modal sensors. The circuits that interface the sensors and the microprocessor for recording the acquired signals will also be integrated into the brace. The microprocessor would acquire the sensed signals, pre-processes them and send the acquired information wirelessly to a smart-phone or a computer. In the smart-phone or computer, an algorithm (that was “trained” previously using data mining techniques) would run to calculate a knee joint health score (a biomarker) for the user’s knee.

In this thesis, key scientific and engineering gaps were addressed towards facilitating the described scenario. Two sensing modalities were conceived and advanced, the combination of which can provide in-depth information about knee health. The first one of these sensing modalities is electrical bioimpedance (EBI), which can reflect changes in the local tissue structure or fluid volume. A high resolution EBI system with low power consumption was developed, targeted to measure knee joint EBI in a wearable setting. A novel, real-time calibration algorithm was introduced that minimizes measurement errors due to environmental changes in uncontrolled settings. Signal processing methods are presented to extract information from the EBI measurements related to knee health. To adapt the data collection process to wearable settings, a position detection algorithm making use of accelerometers was presented, which allows EBI measurements to be taken that are not corrupted by motion artifacts and are taken when the subject’s knee is in a consistent position. Furthermore, a knee brace with dry electrodes integrated (which are more appropriate than wet electrodes for use in a wearable device) is designed. The systems and methods developed are validated using

human subject experiments. Most importantly, it is shown that EBI measurements acquired using the designed system and methods can be used to distinguish between healthy and injured knees. Furthermore, it is demonstrated that EBI measurements can be used to monitor injury recovery quantitatively.

Another sensing modality for knee health monitoring that is utilized in this work is knee acoustical emissions. A multi-modal sensing system to acquire knee acoustical emissions is designed. It is shown that the characteristic signatures of these acoustical emissions are short duration, high energy and broad band acoustical emissions. The ability of electret, MEMS and contact microphones (piezoelectric film) in acquiring these acoustical emissions is evaluated and discussed. An unsupervised, data-driven algorithm that utilizes graph mining is designed to devise a biomarker from knee acoustical emissions, acquired using electret microphones. The biomarker's ability in distinguishing between healthy subjects and subjects with acute unilateral knee injury is demonstrated. Furthermore, it is shown that the devised biomarker can potentially be used to monitor injury recovery.

7.2 Future Directions

There are many potential projects that can emerge from the work presented. First, the presented technology can be used on other joints such as the shoulder and ankle as well. This could be done by adapting the presented systems and methods for the other joints and acquiring data via human subject experiments.

Second, the biomarkers developed using EBI measurements (knee resistance and knee reactance) and the knee acoustical emissions (the graph community factor, GCF), can be understood better by conducting further human subject experiments. Using larger datasets, normal and abnormal ranges for these biomarkers can be defined, signaling a healthy knee or an injured knee respectively.

Currently, both sensing modalities use data acquired from both knees to monitor knee joint health. A third area of future work would involve development of methods that allow only one knee to be used, alleviating the need to wear a brace on both knees. For EBI measurements, this might be done by measuring a reference impedance to subtract from the knee impedance measured, instead of subtracting the impedance of the other knee from this. For knee joint acoustical emissions, more data, the development of new methods and even additions to the system (e.g. more microphones) might be required for this.

Specifically for knee acoustical emissions, a fourth area of future work would involve extracting improved biomarkers by leveraging deep learning. Such an approach can potentially be used to devise novel and more effective audio features and patterns related to knee joint health.

Finally, future work towards designing a “smart brace” should focus on both known engineering methods and further research and development efforts. Both the EBI measurement system and the knee joint acoustical emission sensing systems introduced should be further miniaturized. This requires the development of miniaturized interfacing circuits using conventional engineering approaches. This miniaturization should be done in a way that yields a form factor that can be integrated into a knee brace (e.g. using flexible printed circuit boards). Furthermore, all the sensors involved should be integrated into a single knee brace, in a way that does not cause discomfort for the user. Towards this goal, the use of textile electrodes for EBI measurements rather than copper electrodes should be explored. Furthermore, the signal processing methods described should be implemented using microprocessors and smart-phone applications/computer programs to transition the technology presented to a “smart brace”. In terms of scientific understanding, there is still a significant amount of work that needs to be done to better understand the underlying origin of joint sounds and their propagation to the skin. Future studies can help elucidate some of these basic mechanisms.

7.3 Final Remarks

The scientific and technological advances stemmed by this work could significantly improve the rehabilitation of patients with knee injuries in the future. A patient using the “smart knee brace” can track her progress toward recovery quantitatively and continuously, and then use this information to as guidance during their recovery. This type of out-of-clinic monitoring can also guide physicians and physical therapists in planning treatments and rehabilitation programs for their patients that are personalized, dynamic, and more effective. This dissertation constructs the basis of such a “smart brace” for monitoring the health of joints such as the knee.

REFERENCES

- [1] "American Academy of Orthopedic Surgeons," January 3, 2015; <http://orthoinfo.aaos.org/topic.cfm?topic=a00325>.
- [2] B. E. Gage, N. M. McIlvain, C. L. Collins, S. K. Fields, and R. Dawn Comstock, "Epidemiology of 6.6 Million Knee Injuries Presenting to United States Emergency Departments From 1999 Through 2008," *Academic Emergency Medicine*, vol. 19, no. 4, pp. 378-385, 2012.
- [3] W. L. Calmbach, and M. Hutchens, "Evaluation of patients presenting with knee pain: Part I. History, physical examination, radiographs, and laboratory tests," *American family physician*, vol. 68, no. 5, pp. 907-912, 2003/09//, 2003.
- [4] E. Hefti, W. Müller, R. P. Jakob, and H. U. Stäubli, "Evaluation of knee ligament injuries with the IKDC form," *Knee Surgery, Sports Traumatology, Arthroscopy*, vol. 1, no. 3-4, pp. 226-234, 1993/09/01, 1993.
- [5] L. Friedman, K. Finlay, and E. Jurriaans, "Ultrasound of the knee," *Skeletal Radiology*, vol. 30, no. 7, pp. 361-377, 2001/07/01, 2001.
- [6] P. D. Austermuehle, "Common Knee Injuries in Primary Care," *Nurse Practitioner*, vol. 26, no. 10, pp. 26, 2001.
- [7] B. E. Gage, N. M. McIlvain, C. L. Collins, S. K. Fields, and R. D. Comstock, "Epidemiology of 6.6 million knee injuries presenting to United States emergency departments from 1999 through 2008," *Acad. Emerg. Med.*, vol. 19, no. 4, pp. 378-85, Apr, 2012.
- [8] P. J. McMahon, and H. B. Skinner, "Sports medicine," *Current diagnosis & treatment in orthopedics*, H. B. Skinner, ed., pp. 155-173, New York: Lange Medical Books, 2003.
- [9] W. C. Whiting, "Biomechanics of musculoskeletal injury," R. F. Zernicke, ed., Champaign, IL, 2008, pp. 166-184.
- [10] W. R. Smith, J. R. Shank, H. B. Skinner, E. Diao, and D. W. Lowenberg, "Musculoskeletal trauma surgery," H. B. Skinner, ed., pp. 134-142: New York : Lange Medical Books, 2003.
- [11] M. Majewski, H. Susanne, and S. Klaus, "Epidemiology of athletic knee injuries: A 10-year study," *Knee*, vol. 13, no. 3, pp. 184-8, Jun, 2006.
- [12] J. M. Hootman, R. Dick, and J. Agel, "Epidemiology of collegiate injuries for 15 sports: summary and recommendations for injury prevention initiatives," *J. Athl. Train.*, vol. 42, no. 2, pp. 311-9, 2007 Apr-Jun, 2007.

- [13] J. G. Ingram, S. K. Fields, E. E. Yard, and R. D. Comstock, "Epidemiology of knee injuries among boys and girls in US high school athletics," *Am J Sports Med*, vol. 36, no. 6, pp. 1116-22, Jun, 2008.
- [14] G. S. Smith, A. L. Dannenberg, and P. J. Amoroso, "Hospitalization due to injuries in the military. Evaluation of current data and recommendations on their use for injury prevention," *Am. J. Prev. Med.*, vol. 18, no. 3 Suppl, pp. 41-53, Apr, 2000.
- [15] J. M. Hootman, C. A. Macera, B. E. Ainsworth, C. L. Addy, M. Martin, and S. N. Blair, "Epidemiology of musculoskeletal injuries among sedentary and physically active adults," *Med. Sci. Sports Exerc.*, vol. 34, no. 5, pp. 838-44, May, 2002.
- [16] Aug. 10, 2015; <http://orthoinfo.aaos.org/topic.cfm?topic=a00325>.
- [17] Z. Ya-Li, D. Xiao-Rong, C. C. Y. Poon, B. P. L. Lo, Z. Heye, Z. Xiao-Lin, Y. Guang-Zhong, Z. Ni, and Z. Yuan-Ting, "Unobtrusive Sensing and Wearable Devices for Health Informatics," *IEEE Trans. Biomed. Eng.*, vol. 61, no. 5, pp. 1538-1554, 2014.
- [18] A. Rampp, J. Barth, S. Schuelein, K. G. Gassmann, J. Klucken, and B. M. Eskofier, "Inertial Sensor-Based Stride Parameter Calculation From Gait Sequences in Geriatric Patients," *IEEE Trans. Biomed. Eng.*, vol. 62, no. 4, pp. 1089-1097, 2015.
- [19] L. Atallah, G. G. Jones, R. Ali, J. J. H. Leong, B. Lo, and Y. Guang-Zhong, "Observing Recovery from Knee-Replacement Surgery by Using Wearable Sensors," *Body Sensor Networks (BSN), 2011 International Conference on, Dallas, TX*, pp. 29-34, Dallas, TX, 2011.
- [20] L. D. Toffola, S. Patel, M. Y. Ozsecen, R. Ramachandran, and P. Bonato, "A wearable system for long-term monitoring of knee kinematics," *Biomedical and Health Informatics (BHI), 2012 IEEE-EMBS International Conference on, Hong Kong, China*, pp. 188-191, Hong Kong, China, 2012.
- [21] J. Nyboer, M. M. Kreider, and L. Hannapel, "Electrical Impedance Plethysmography A Physical and Physiologic Approach to Peripheral Vascular Study," *Circulation*, vol. 2, no. 6, pp. 811-821, 1950.
- [22] A. Sherwood, M. T. Allen, J. Fahrenberg, R. M. Kelsey, W. R. Lovallo, and L. J. P. v. Doomen, "Methodological Guidelines for Impedance Cardiography," *Psychophysiology*, vol. 27, no. 1, pp. 1-23, 1990.
- [23] R. Patterson, W. Kubicek, E. Kinnen, D. Witsoe, and G. Noren, "Development of an electrical impedance plethysmography system to monitor cardiac output." pp. 56-71.

- [24] E. B. Neves, A. V. Pino, R. M. V. R. d. Almeida, and M. N. d. Souza, "Knee bioelectric impedance assessment in healthy/with osteoarthritis subjects," *Physiological Measurement*, vol. 31, no. 2, pp. 207, 2010.
- [25] L. Nescolarde, J. Yanguas, H. Lukaski, X. Alomar, J. Rosell-Ferrer, and G. Rodas, "Localized bioimpedance to assess muscle injury," *Physiological Measurement*, vol. 34, no. 2, pp. 237, 2013.
- [26] L. Nescolarde, J. Yanguas, H. Lukaski, X. Alomar, J. Rosell-Ferrer, and G. Rodas, "Effects of muscle injury severity on localized bioimpedance measurements," *Physiological Measurement*, vol. 36, no. 1, pp. 27, 2015.
- [27] C. Pichonnaz, J.-P. Bassin, D. Currat, E. Martin, and B. M. Jolles, "Bioimpedance for Oedema Evaluation after Total Knee Arthroplasty," *Physiotherapy Research International*, vol. 18, no. 3, pp. 140-147, 2013.
- [28] W. G. Kubicek, R. P. Patterson, and D. A. Witsoe, "Impedance Cardiography as a Noninvasive Method of Monitoring Cardiac Function and Other Parameters of the Cardiovascular System," *Annals of the New York Academy of Sciences*, vol. 170, pp. 724-732, 1970.
- [29] F. Risacher, J. Jossinet, E. McAdams, J. McLaughlin, Y. Mann, M. Schmitt, A. Matias, and R. Jarry, "Impedance plethysmography for the evaluation of pulse-wave velocity in limbs," *Medical and Biological Engineering and Computing*, vol. 31, no. 3, pp. 318-322, 1993.
- [30] X. Hua, X. Chena, R. Rena, B. Zhoua, Y. Qianc, H. Lic, and S. Xiaa, "Adaptive Filtering and Characteristics Extraction for Impedance Cardiography," *Journal of Fiber Bioengineering and Informatics*, vol. 7, no. 1, pp. 81-90, 2014.
- [31] H. Woltjer, H. Bogaard, and P. De Vries, "The technique of impedance cardiography," *European Heart Journal*, vol. 18, no. 9, pp. 1396-1403, 1997.
- [32] B. Brown, W. Pryce, D. Baumber, and R. Clarke, "Impedance plethysmography: can it measure changes in limb blood flow," *Medical and biological engineering*, vol. 13, no. 5, pp. 674-682, 1975.
- [33] P. J. Langlois, N. Neshatvar, and A. Demosthenous, "A Sinusoidal Current Driver With an Extended Frequency Range and Multifrequency Operation for Bioimpedance Applications," *Biomedical Circuits and Systems, IEEE Transactions on*, vol. 9, no. 3, pp. 401-411, 2015.
- [34] L. Constantinou, I. F. Triantis, R. Bayford, and A. Demosthenous, "High-Power CMOS Current Driver With Accurate Transconductance for Electrical Impedance Tomography," *Biomedical Circuits and Systems, IEEE Transactions on*, vol. 8, no. 4, pp. 575-583, 2014.

- [35] R. C. Kubendran, S. Lee, S. Mitra, and R. F. Yazicioglu, "Error correction algorithm for high accuracy bio-impedance measurement in wearable healthcare applications," *IEEE Trans Biomed Cir and Syst*, vol. 8, no. 2, pp. 196-205, 2014.
- [36] M. Ulbrich, J. Muhlsteff, D. Teichmann, S. Leonhardt, and M. Walter, "A Thorax Simulator for Complex Dynamic Bioimpedance Measurements With Textile Electrodes," *Biomedical Circuits and Systems, IEEE Transactions on*, vol. PP, no. 99, pp. 1-1, 2014.
- [37] J. G. Webster, *Medical Instrumentation: Application and Design*, 4 ed., New York: Wiley, 2010.
- [38] R. C. Bray, D. J. Butterwick, M. R. Doschak, and J. V. Tyberg, "Coloured microsphere assessment of blood flow to knee ligaments in adult rabbits: Effects of injury," *Journal of Orthopaedic Research*, vol. 14, no. 4, pp. 618-625, 1996.
- [39] R. E. Kleiger, P. K. Stein, and J. T. Bigger, "Heart Rate Variability: Measurement and Clinical Utility," *Annals of Noninvasive Electrocardiology*, vol. 10, no. 1, pp. 88-101, 2005.
- [40] R. D. Berger, S. Akselrod, D. Gordon, and R. J. Cohen, "An Efficient Algorithm for Spectral Analysis of Heart Rate Variability," *Biomedical Engineering, IEEE Transactions on*, vol. BME-33, no. 9, pp. 900-904, 1986.
- [41] V. Lindh, U. Wiklund, and S. Håkansson, "Heel lancing in term new-born infants: an evaluation of pain by frequency domain analysis of heart rate variability," *Pain*, vol. 80, no. 1-2, pp. 143-148, 3/1/, 1999.
- [42] Y. Wu, S. Krishnan, and R. M. Rangayyan, "Computer-aided diagnosis of knee-joint disorders via vibroarthrographic signal analysis: a review," *Crit. Rev. Biomed. Eng.*, vol. 38, no. 2, pp. 201-24, 2010.
- [43] R. A. Mollan, G. C. McCullagh, and R. I. Wilson, "A critical appraisal of auscultation of human joints," *Clin Orthop Relat Res*, no. 170, pp. 231-7, Oct, 1982.
- [44] S. C. Abbott, and M. D. Cole, "Vibration arthrometry: a critical review," *Crit. Rev. Biomed. Eng.*, vol. 41, no. 3, pp. 223-42, 2013.
- [45] L. K. Shark, H. Chen, and J. Goodacre, "Discovering differences in acoustic emission between healthy and osteoarthritic knees using a four-phase model of sit-stand-sit movements," *Open Med. Inform. J.*, vol. 4, pp. 116-25, 2010.
- [46] J. H. Lee, C. C. Jiang, and T. T. Yuan, "Vibration arthrometry in patients with knee joint disorders," *IEEE Trans. Biomed. Eng.*, vol. 47, no. 8, pp. 1131-3, Aug, 2000.

- [47] S. Tavathia, R. M. Rangayyan, C. B. Frank, G. D. Bell, K. O. Ladly, and Y. T. Zhang, "Analysis of knee vibration signals using linear prediction," *IEEE Trans. Biomed. Eng.*, vol. 39, no. 9, pp. 959-970, 1992.
- [48] R. M. Rangayyan, and Y. F. Wu, "Screening of knee-joint vibroarthrographic signals using statistical parameters and radial basis functions," *Med. Biol. Eng. Comput.*, vol. 46, no. 3, pp. 223-32, Mar, 2008.
- [49] L. Tsair-Fwu, L. Wei-Chun, W. Li-Fu, and W. Hung-Yu, "Analysis of Vibroarthrographic Signals for Knee Osteoarthritis Diagnosis," *Genetic and Evolutionary Computing (ICGEC), 2012 Sixth International Conference on, Kitakyushu, Japan*, pp. 223-228, Kitakyushu, Japan, 2012.
- [50] S. Krishnan, R. M. Rangayyan, G. D. Bell, and C. B. Frank, "Adaptive time-frequency analysis of knee joint vibroarthrographic signals for noninvasive screening of articular cartilage pathology," *IEEE Trans. Biomed. Eng.*, vol. 47, no. 6, pp. 773-783, 2000.
- [51] K. Umopathy, and S. Krishnan, "Modified local discriminant bases algorithm and its application in analysis of human knee joint vibration signals," *IEEE Trans. Biomed. Eng.*, vol. 53, no. 3, pp. 517-523, 2006.
- [52] S. Cai, S. Yang, F. Zheng, M. Lu, Y. Wu, and S. Krishnan, "Knee joint vibration signal analysis with matching pursuit decomposition and dynamic weighted classifier fusion," *Comput. Math Methods Med.*, vol. 2013, pp. 904267, 2013.
- [53] S. Hersek, H. Töreyn, and O. T. Inan, "A Robust System for Longitudinal Knee Joint Edema and Blood Flow Assessment Based on Vector Bioimpedance Measurements," *IEEE transactions on biomedical circuits and systems*, vol. 10, no. 3, pp. 545-555, 2016.
- [54] H. Lukaski, and M. Moore, "Bioelectrical Impedance Assessment of Wound Healing," *J Diabetes Sci Technol*, vol. 6, no. 1, pp. 209-212, 2012.
- [55] E. McAdams, J. Jossinet, A. Lackermeier, and F. Risacher, "Factors affecting electrode-gel-skin interface impedance in electrical impedance tomography," *Medical and Biological Engineering and Computing*, vol. 34, no. 6, pp. 397-408, 1996.
- [56] M. Ulbrich, J. Mühlsteff, A. Sipilä, M. Kamppi, A. Koskela, M. Myry, T. Wan, S. Leonhardt, and M. Walter, "The IMPACT shirt: textile integrated and portable impedance cardiography," *Physiological measurement*, vol. 35, no. 6, pp. 1181, 2014.
- [57] S. Grimnes, and O. Martinsen, *Bioimpedance and Bioelectricity Basics*, 2nd ed., Oxford, UK: Academic, 2008.

- [58] A. K. Barros, M. Yoshizawa, and Y. Yasuda, "Filtering noncorrelated noise in impedance cardiography," *Biomedical Engineering, IEEE Transactions on*, vol. 42, no. 3, pp. 324-327, 1995.
- [59] J. Pan, and W. J. Tompkins, "A Real-Time QRS Detection Algorithm," *Biomedical Engineering, IEEE Transactions on*, vol. BME-32, no. 3, pp. 230-236, 1985.
- [60] J. H. Nagel, L. Y. Shyu, S. P. Reddy, B. E. Hurwitz, P. M. McCabe, and N. Schneiderman, "New signal processing techniques for improved precision of noninvasive impedance cardiography," *Annals of Biomedical Engineering*, vol. 17, no. 5, pp. 517-534, 1989/09/01, 1989.
- [61] B. Sanchez, J. Schoukens, R. Bragos, and G. Vandersteen, "Novel Estimation of the Electrical Bioimpedance Using the Local Polynomial Method. Application to In Vivo Real-Time Myocardium Tissue Impedance Characterization During the Cardiac Cycle," *Biomedical Engineering, IEEE Transactions on*, vol. 58, no. 12, pp. 3376-3385, 2011.
- [62] B. Sanchez, E. Louarroudi, E. Jorge, J. Cinca, R. Bragos, and R. Pintelon, "A new measuring and identification approach for time-varying bioimpedance using multisine electrical impedance spectroscopy," *Physiological Measurement*, vol. 34, no. 3, pp. 339, 2013.
- [63] A. Hartov, R. A. Mazzaresse, F. R. Reiss, T. E. Kerner, K. S. Osterman, D. B. Williams, and K. D. Paulsen, "A multichannel continuously selectable multifrequency electrical impedance spectroscopy measurement system," *Biomedical Engineering, IEEE Transactions on*, vol. 47, no. 1, pp. 49-58, 2000.
- [64] J. Ramos, J. L. Ausín, A. M. Lorido, F. Redondo, and J. F. Duque-Carrillo, "A wireless, compact, and scalable bioimpedance measurement system for energy-efficient multichannel body sensor solutions," *Journal of Physics: Conference Series*, vol. 434, no. 1, pp. 012016, 2013.
- [65] L. Yan, J. Bae, S. Lee, T. Roh, K. Song, and H.-J. Yoo, "A 3.9 mW 25-Electrode Reconfigured Sensor for Wearable Cardiac Monitoring System," *Solid-State Circuits, IEEE Journal of*, vol. 46, no. 1, pp. 353-364, 2011.
- [66] S. Lee, S. Polito, C. Agell, S. Mitra, R. F. Yazicioglu, J. Riistama, J. Habetha, and J. Penders, "A Low-power and Compact-sized Wearable Bio-impedance Monitor with Wireless Connectivity," *Journal of Physics: Conference Series*, vol. 434, no. 1, pp. 012013, 2013.
- [67] A. Yufera, A. Rueda, J. M. Munoz, R. Doldan, G. Leger, and E. O. Rodriguez-Villegas, "A tissue impedance measurement chip for myocardial ischemia detection," *Circuits and Systems I: Regular Papers, IEEE Transactions on*, vol. 52, no. 12, pp. 2620-2628, 2005.

- [68] P. Kassanos, L. Constantinou, I. F. Triantis, and A. Demosthenous, "An Integrated Analog Readout for Multi-Frequency Bioimpedance Measurements," *Sensors Journal, IEEE*, vol. 14, no. 8, pp. 2792-2800, 2014.
- [69] N. Van Helleputte, M. Konijnenburg, J. Pettine, J. Dong-Woo, K. Hyejung, A. Morgado, R. Van Wegberg, T. Torfs, R. Mohan, A. Breeschoten, H. de Groot, C. Van Hoof, and R. F. Yazicioglu, "A 345 µW Multi-Sensor Biomedical SoC With Bio-Impedance, 3-Channel ECG, Motion Artifact Reduction, and Integrated DSP," *Solid-State Circuits, IEEE Journal of*, vol. 50, no. 1, pp. 230-244, 2015.
- [70] S. Kaufmann, A. Malhotra, G. Ardelt, and M. Ryschka, "A high accuracy broadband measurement system for time resolved complex bioimpedance measurements," *Physiological Measurement*, vol. 35, no. 6, pp. 1163, 2014.
- [71] S. Sun, L. Xu, Z. Cao, H. Zhou, and W. Yang, "A high-speed electrical impedance measurement circuit based on information-filtering demodulation," *Measurement Science and Technology*, vol. 25, no. 7, pp. 075010, 2014.
- [72] C. Margo, J. Katrib, M. Nadi, and A. Rouane, "A four-electrode low frequency impedance spectroscopy measurement system using the AD5933 measurement chip," *Physiological Measurement*, vol. 34, no. 4, pp. 391, 2013.
- [73] F. Seoane, J. Ferreira, J. J. Sánchez, and R. Bragós, "An analog front-end enables electrical impedance spectroscopy system on-chip for biomedical applications," *Physiological Measurement*, vol. 29, no. 6, pp. S267, 2008.
- [74] L.-Y. Shyu, C.-Y. Chiang, C.-P. Liu, and W.-C. Hu, "Portable impedance cardiography system for real-time noninvasive cardiac output measurement," *Journal of Medical and Biological Engineering*, vol. 20, no. 4, pp. 193-202, 2000.
- [75] Y. Yang, J. Wang, G. Yu, F. Niu, and P. He, "Design and preliminary evaluation of a portable device for the measurement of bioimpedance spectroscopy," *Physiological Measurement*, vol. 27, no. 12, pp. 1293, 2006.
- [76] T. Schlebusch, Ro, x, thlingsho, x, L. fer, K. Saim, Ko, x, M. ny, and S. Leonhardt, "On the Road to a Textile Integrated Bioimpedance Early Warning System for Lung Edema." pp. 302-307.
- [77] M. C. Jones, J. S. Marron, and S. J. Sheather, "A brief survey of bandwidth selection for density estimation," *Journal of the American Statistical Association*, vol. 91, no. 433, pp. 401-407, 1996.
- [78] C. Pichonnaz, J.-P. Bassin, E. Lécureux, D. Currat, and B. M. Jolles, "Bioimpedance spectroscopy for swelling evaluation following total knee arthroplasty: a validation study," *BMC Musculoskeletal Disorders*, vol. 16, no. 1, pp. 1-8, 2015.

- [79] L. Nescolarde, J. Yanguas, H. Lukaski, X. Alomar, J. Rosell-Ferrer, and G. Rodas, "Effects of muscle injury severity on localized bioimpedance measurements," *Physiological measurement*, vol. 36, no. 1, pp. 27, 2014.
- [80] E. B. Neves, A. V. Pino, R. M. V. R. de Almeida, and M. N. de Souza, "Knee bioelectric impedance assessment in healthy/with osteoarthritis subjects," *Physiological measurement*, vol. 31, no. 2, pp. 207, 2009.
- [81] M. N. Sawka, "Body Fluid Responses and Hypohydration During Exercise-Heat Stress," *Human Performance Physiology and Environmental Medicine at Terrestrial Extremes*, K. B. Pandolf, M. N. Sawka and R. R. Gonzalez, eds., pp. 236-240, Indianapolis, IN: Brown & Benchmark Press, 1988.
- [82] E. A. Hines Jr, and G. E. Brown, "The cold pressor test for measuring the reactivity of the blood pressure: Data concerning 571 normal and hypertensive subjects," *American Heart Journal*, vol. 11, no. 1, pp. 1-9, 1936.
- [83] Y. M. Chi, T.-P. Jung, and G. Cauwenberghs, "Dry-contact and noncontact biopotential electrodes: methodological review," *Biomedical Engineering, IEEE Reviews in*, vol. 3, pp. 106-119, 2010.
- [84] L. Fabrizi, A. McEwan, E. Woo, and D. S. Holder, "Analysis of resting noise characteristics of three EIT systems in order to compare suitability for time difference imaging with scalp electrodes during epileptic seizures," *Physiological measurement*, vol. 28, no. 7, pp. S217, 2007.
- [85] P. C. Choudhari, and M. Panse, "Artifact Removal from the Radial Bioimpedance Signal using Adaptive Wavelet Packet Transform," *International Journal of Computational Engineering Research (IJCER)* vol. 4, no. 7, pp. 2250-3005, July 2014.
- [86] G. Medrano, S. Leonhardt, and P. Zhang, "Modeling the influence of body position in bioimpedance measurements." pp. 3934-3937.
- [87] J. Friedman, T. Hastie, and R. Tibshirani, *The elements of statistical learning*, p.^pp. 417-426: Springer series in statistics Springer, Berlin, 2001.
- [88] S. Raschka, *Python Machine Learning*, p.^pp. 210-213: Packt Publishing Ltd, 2015.
- [89] Y.-H. Chen, M. O. de Beeck, L. Vanderheyden, E. Carrette, V. Mihajlović, K. Vanstreels, B. Grundlehner, S. Gadeyne, P. Boon, and C. Van Hoof, "Soft, comfortable polymer dry electrodes for high quality ECG and EEG recording," *Sensors*, vol. 14, no. 12, pp. 23758-23780, 2014.
- [90] O. G. Martinsen, and S. Grimnes, *Bioimpedance and bioelectricity basics*, p.^pp. 169: Academic press, 2011.

- [91] J. K. Hackett, and M. Shah, "Multi-sensor fusion: a perspective." pp. 1324-1330.
- [92] D. L. Hall, and J. Llinas, "An introduction to multisensor data fusion," *Proceedings of the IEEE*, vol. 85, no. 1, pp. 6-23, 1997.
- [93] C. N. Teague, S. Hersek, H. Toreyin, M. L. Millard-Stafford, M. L. Jones, G. F. Kogler, M. N. Sawka, and O. T. Inan, "Novel Methods for Sensing Acoustical Emissions from the Knee for Wearable Joint Health Assessment," 2016.
- [94] T. Seel, J. Raisch, and T. Schauer, "IMU-Based Joint Angle Measurement for Gait Analysis," *Sensors*, vol. 14, no. 4, pp. 6891, 2014.
- [95] W. L. Martinez, A. Martinez, and J. Solka, *Exploratory Data Analysis with MATLAB, Second Edition*: CRC Press, 2010.
- [96] B. Rosner, *Fundamentals of Biostatistics*: Cengage Learning, 2010.
- [97] F. S. L. a. D. K. Jonathan, "Human pose recovery using wireless inertial measurement units," *Physiological Measurement*, vol. 33, no. 12, pp. 2099, 2012.
- [98] L. Kun, L. Tao, K. Shibata, and Y. Inoue, "Visual estimation of lower limb motion using physical and virtual sensors." pp. 179-184.
- [99] K. A. Elsaid, G. D. Jay, M. L. Warman, D. K. Rhee, and C. O. Chichester, "Association of articular cartilage degradation and loss of boundary-lubricating ability of synovial fluid following injury and inflammatory arthritis," *Arthritis & Rheumatism*, vol. 52, no. 6, pp. 1746-1755, 2005.
- [100] S. L. Woo, S. D. Abramowitch, R. Kilger, and R. Liang, "Biomechanics of knee ligaments: injury, healing, and repair," *J Biomech*, vol. 39, no. 1, pp. 1-20, 2006.
- [101] L.-K. Shark, H. Chen, and J. Goodacre, "Discovering Differences in Acoustic Emission Between Healthy and Osteoarthritic Knees Using a Four-Phase Model of Sit-Stand-Sit Movements," *The Open Medical Informatics Journal*, vol. 4, pp. 116-125, 2010.
- [102] J.-H. Lee, C.-C. Jiang, and T.-T. Yuan, "Vibration arthrometry in patients with knee joint disorders," *IEEE Transactions on Biomedical Engineering*, vol. 47, no. 8, pp. 1131-1133, 2000.
- [103] T. F. Lee, W. C. Lin, L. F. Wu, and H. Y. Wang, "Analysis of Vibroarthrographic Signals for Knee Osteoarthritis Diagnosis." pp. 223-228.
- [104] S. Krishnan, R. M. Rangayyan, G. D. Bell, and C. B. Frank, "Adaptive time-frequency analysis of knee joint vibroarthrographic signals for noninvasive screening of articular cartilage pathology," *IEEE Transactions on Biomedical Engineering*, vol. 47, no. 6, pp. 773-783, 2000.

- [105] J. M. Binkley, P. W. Stratford, S. A. Lott, and D. L. Riddle, "The Lower Extremity Functional Scale (LEFS): scale development, measurement properties, and clinical application," *Physical therapy*, vol. 79, no. 4, pp. 371-383, 1999.
- [106] T. Giannakopoulos, and A. Pikrakis, *Introduction to Audio Analysis: A MATLAB® Approach*, pp. 70-96: Academic Press, 2014.
- [107] L. Muda, M. Begam, and I. Elamvazuthi, "Voice recognition algorithms using mel frequency cepstral coefficient (MFCC) and dynamic time warping (DTW) techniques," *arXiv preprint arXiv:1003.4083*, 2010.
- [108] L. A. Adamic, and E. Adar, "Friends and neighbors on the web," *Social networks*, vol. 25, no. 3, pp. 211-230, 2003.
- [109] M. Rosvall, and C. T. Bergstrom, "Maps of random walks on complex networks reveal community structure," *Proceedings of the National Academy of Sciences*, vol. 105, no. 4, pp. 1118-1123, 2008.
- [110] M. Pouyan, and M. Nourani, "Clustering Single-Cell Expression Data Using Random Forest Graphs," *IEEE Journal of Biomedical and Health Informatics*, 2016.
- [111] C. M. Bishop, "Pattern recognition," *Machine Learning*, vol. 128, 2006.
- [112] M. Verleysen, and D. François, "The curse of dimensionality in data mining and time series prediction." pp. 758-770.
- [113] P. Indyk, and R. Motwani, "Approximate nearest neighbors: towards removing the curse of dimensionality." pp. 604-613.
- [114] J. H. Levine, E. F. Simonds, S. C. Bendall, K. L. Davis, D. A. El-ad, M. D. Tadmor, O. Litvin, H. G. Fienberg, A. Jager, and E. R. Zunder, "Data-driven phenotypic dissection of AML reveals progenitor-like cells that correlate with prognosis," *Cell*, vol. 162, no. 1, pp. 184-197, 2015.
- [115] C. Xu, and Z. Su, "Identification of cell types from single-cell transcriptomes using a novel clustering method," *Bioinformatics*, pp. btv088, 2015.
- [116] C. Fraley, and A. E. Raftery, "Model-based clustering, discriminant analysis, and density estimation," *Journal of the American statistical Association*, vol. 97, no. 458, pp. 611-631, 2002.
- [117] J. M. Joyce, "Kullback-leibler divergence," *International Encyclopedia of Statistical Science*, pp. 720-722: Springer, 2011.
- [118] L. v. d. Maaten, and G. Hinton, "Visualizing data using t-SNE," *Journal of Machine Learning Research*, vol. 9, no. Nov, pp. 2579-2605, 2008.

- [119] M. E. Houle, H.-P. Kriegel, P. Kröger, E. Schubert, and A. Zimek, "Can shared-neighbor distances defeat the curse of dimensionality?." pp. 482-500.